ARTURO ORTIZ-ARROYO

CONTRIBUTION TO THE MODELING OF PACKED BED REACTORS UNDER PLUGGING CONDITIONS IN SINGLE AND TWO PHASE TRICKLE FLOW

Thèse présentée
à la Faculté des études supérieures de l'Université Laval
dans le cadre du programme de doctorat en Génie Chimique
pour l’obtention du grade de Philosophiae Doctor (Ph.D)

FACULTÉ DES SCIENCES ET DE GÉNIE
UNIVERSITÉ LAVAL
QUÉBEC

MAI, 2004

Résumé Long

Les réacteurs à lit fixe arrosé vers le bas en régime ruisselant se comportent comme des filtres en profondeur quand des liquides contaminés entrent en contact avec le lit. La rétention des solides de petite taille occasionne une augmentation progressive de la perte de charge. Éventuellement, l'opération du réacteur doit être interrompue et le lit colmaté est écarté, même si le matériel catalytique qui le constitue demeure encore actif occasionnant de la sorte des pertes économiques importantes. Cet ouvrage propose des méthodes et des modèles pour la simulation du colmatage du lit fixe avec des écoulements mono et biphasiques.

Deux niveaux d'analyse sont présentés. Au niveau du lit complet, le modèle Eulérien-Eulérien, qui est une procédure de la mécanique des fluides numérique (CFD), permet l'inclusion des équations de fermeture pour le transfert de masse et de quantité de mouvement dans le contexte de la filtration en profondeur (*deep bed filtration*, DBF)..

A l'échelle d'un seul élément de garnissage, l'analyse de trajectoire est couramment acceptée pour l'étude du taux de capture de particules dans le cadre de la filtration en profondeur dans le lit fixe. Dans le cas de l'écoulement monophasique, la capture de particules est calculée par l'expression de Rajagolapan & Tien (1976). L'insertion de cette expression dans le code CFD fourni des informations utiles à propos du comportement de la colonne en état transitoire.

Dans le cas de l'écoulement biphasique en régime ruisselant, aucune procédure d'analyse de trajectoire n'est connue. En conséquence, une toute nouvelle adaptation de cette méthodologie est proposée. En utilisant un modèle de film pour représenter le réacteur à lit arrosé, l'analyse de TA est accomplie dans les cas suivants; monophasique et biphasique avec déposition monocouche et multicouche. Les tendances de TA concordent avec l'analyse de Rajagopalan et Tien (1976) démontrant que les mécanismes de capture sont du même type que ceux qui se présentent dans l'écoulement monophasique et qu'ils sont modifiés uniquement par la présence de la phase gazeuse. Les résultats ont été comparés aux données expérimentales de Gray et al. (2002).

La rétention liquide statique (SLH) est un paramètre qui, selon des observations expérimentales, affecte sensiblement la capture en conditions multiphasiques. Une collection presque exhaustive des données de la SLH a été construite à partir de la littérature expérimentale disponible. Avec ces données de SLH et avec l'utilisation d'un algorithme considérant un minimum d'énergie de ménisque, des angles de

contact moyennés pour une gamme de liquides et de garnissages ont été obtenus. En réinsérant les angles de contact calculés dans un logiciel de réseaux neuronaux, une corrélation qui surpasse toutes les corrélations disponibles a été obtenue.

À l'avenir, il serait souhaitable que la rétention liquide statique soit incluse dans le modèle de colmatage, ou à tout le moins dans l'analyse des trajectoires.

Long summary

Trickle bed reactors (TBR) behave as deep bed filtration (DBF) units when the liquid feedstock is contaminated with fine particles. Solid retention causes an ever increasing pressure drop in the bed that leads to eventual halting of the installation. Industry response has been so far to change the plugged, but still active, catalytic bed with a fresh catalyst packing causing important profit losses of the process.

In this work two levels of analysis are proposed for the DBF in single and two phase trickle flow conditions. At bed scale, an Eulerian-Eulerian CFD approach is used that provides the framework for the insertion of closure equations for the mass transfer in DBF.

At pore scale, Trajectory Analysis (TA) is used as is an accepted procedure for the analysis of Deep Bed Filtration (DBF) in single-phase aqueous systems. In single phase flow through packed beds, the known TA based expression of Rajagolapan and Tien (1976) is used. By inserting this expression in the CFD approach it becomes possible to obtain valuable information about the transient structure and development of plugging. Benchmarking was obtained with the work of Narayan et al. (1997).

In two phase trickle flow, no TA approach is known so far and an all new extension of this methodology is proposed in this work. Using a film model to represent the trickle bed reactor, TA analysis is performed in single phase, one-layer and multilayer deposition in TBR conditions. TA tendencies were akin to the analysis of Rajagopalan and Tien (1976) demonstrating that deposition mechanisms are of the same kind as in the single phase flow only modified by the presence of the gas phase. Results were compared with the data of Gray et al. (2002).

Static liquid hold-up (SLH) is a parameter that, according to experimental observations, affects significantly solid deposition in multiphase conditions. An almost exhaustive collection of SLH values was constructed from the available experimental literature. With the SLH data and with the use of a minimum energy algorithm, average contact angles for a wide range of liquids and packing were obtained. Reinserting the calculated contact angles in neural network software, a correlation was obtained which outperforms all the available correlations. It is hoped that in future work, this last parameter, the SLH, will be included in the plugging model or at least in the trajectory analysis at the collector scale.

Avant-Propos

I would like to bring the following paragraphs to the attention of the readers:

- Prof. Faiçal Larachi provided technical guidance, proposed ideas and discussed all the aspects of the written articles. A very important part of his contribution was the correction and writing of all the produced manuscripts.

- Prof. Bernard Grandjean proposed ideas and valuable discussions on the second and fourth chapter.

- Dr. Ion Iliuta revised the manuscript of chapter 4.

- Dr. Shantanu Roy provided considerable help on the implementation of the simulations and helpful discussions on the subjects treated in chapter 2.

The author of the thesis structured the project, conceived the new models and proposed the application of existing ones, conducted and programmed all the simulations, analysed the obtained results and wrote all the draft manuscripts with the contributions mentioned above.

Consequently the following papers were produced;

CFD modeling and simulation of clogging in packed beds with non aqueous media. Arturo Ortiz-Arroyo, Bernard Grandjean, Shantanu Roy, Faical Larachi. Paper published in *AIChE J* (2002) v48, n8, 1596-1609.

Lagrange-Euler-Euler CFD approach for modelling deep bed filtration in trickle flow reactors. Arturo Ortiz-Arroyo, Faical Larachi. Paper accepted in *Separation and Purification Technology*, May 2004.

Method for inferring contact angle and for correlating static liquid hold-up in packed beds.
Arturo Ortiz-Arroyo, Faical Larachi. Paper published in *Chem. Eng. Sci.* (2003) v58, n13, 2835-2855.

Additionally some findings in chapter 2 and 3 were presented in the following conferences;

A. Ortiz-Arroyo, F. Larachi, B.P.A. Grandjean, S. Roy "Understanding plugging with fines in 2-D trickle beds using CFD simulations" 50th CChE Conf., Montréal, Québec, October 15-18 (2000).

A. Ortiz-Arroyo, F. Larachi, B.P.A. Grandjean, S. Roy "Modeling and simulation of clogging in packed-bed reactors with non-aqueous media using CFD" 2001 CREL annual meeting, St.-Louis, Missouri, USA, November 15 (2001).

A. Ortiz-Arroyo, F. Larachi, B.P.A. Grandjean, S. Roy "Étude par mécanique des fluides numérique du colmatage par lit fixe" 70th ACFAS Conference, Québec, May 13-17 (2002).

A. Ortiz-Arroyo, F. Larachi "A proposed methodology for the clogging of trickle beds; a VOF-PTM approach" VIème Journée d'activités CERPIC, Université Laval, Québec, March 5 (2002).

A. Ortiz-Arroyo, F. Larachi "Study of the deposition of fines by trajectory analysis on packed beds operating in gas-liquid trickle flow. CFD and slit models" VIIème Journée d'activités CERPIC, Université Laval, Québec, March 4 (2003).

A. Ortiz-Arroyo, F. Larachi "Modeling deep bed filtration in trickle bed reactors through computational fluid dynamics" Chemical Reaction Engineering IX, Meeting the challenges for new technology, June 29- July 4, Québec, Canada (2003)

Acknowledgements

I would like to express my sincere gratitude to Prof. Faiçal Larachi for his constant support, advice and mainly for his patience along all the stages of this work. Without his aid, this work could not be accomplished.

Prof. Bernard Grandjean is also acknowledged for his suggestions and support.

I would like to express my appreciation to the Département de génie chimique de l'Université Laval for the kind help provided.

I thank my friends and colleagues in the Département de génie chimique de l'Université Laval for their continuous support and to all those who contributed to this work.

CONACyT, México, Universidad Autónoma de Tlaxcala, México and CERPIC, Quebec, are greatly acknowledged as they were important financial supporters of this work.

The Los Alamos National Laboratory is acknowledged for their permission to use their CFDLib codes. Contributions of the CFDLib's user community are recognized as invaluable help for the implementation and conduction of the CFD simulations.

I am especially grateful to my friends Adrian Villegas-Jimenez, Manuel Garcia-Perez, Alejandro Larroca, Salomon Gonzalez and Aurelio Dominguez for their moral support for this work.

Dedicado principalmente a Aura y Angel
por el tiempo que debio ser suyo…

A mis padres Blanca y Daniel
con muchisimo cariño.

A mis hermanos Columba, Blanca, Daniel y Alfonso

A Mayeli gracias.

A mis sobrinos
... porque hay luces en camino.

A Rafael Ortega, Ignacio Leal, Gustavo Garza, Mateo Gomez y Gustavo Piñero,

por su amistad, epd.

A Rajae

Contents

List of figures

List of tables

CHAPTER 1

General introduction

1.1 Problem statement: Plugging of packed bed reactors

Deep Bed Filtration has been used for centuries in the treatment and purification of contaminated water. An effluent of water polluted with small suspended solids at low concentrations is circulated through a porous media. Inside the packed bed, some of the contaminating solids impact the surface of the packing and are retained by surface forces. Once the polluting particles eliminated, the fluid leaves the filter as a purified stream of liquid.

When the capture of small solid particles by the bed appears in processing units such as hydrotreaters in the refinery and petroleum industries, it turns into a serious problem that degrades the process and has considerable effect on its economics and technical performance. Turning into a real filter, the packed-bed reactor hydrodynamics is altered dramatically by early increasing of the pressure drop and reducing bed permeability. While permeability is affected by the restriction in the porous space available to the flowing phases, pressure drop is increased by a two-fold effect: the reduction of porosity and the increase of the area for momentum transfer. This augmentation of the surface of the collectors is caused by the area of the captured fines that is added to the clean collector's area (O'Melia and Ali, 1978).

If the pressure drop builds up beyond the allowed limits of pumps and compressors feeding the packed bed, then the column must be stopped and the catalytic charge dumped and exchanged with a fresh packing unit. In many cases the plugged bed still has catalytic activity so the process economics suffers by the cost of the expensive exhausted bed.

It is easy to forecast that the problem of plugging of packed beds will be encountered more often and will be accentuated in the future. Two main reasons can be given;

- Petroleum cuts of high boiling point usually were disposed or used in road carpeting. Actually, with the monotonic decrease of oils reserves there is a necessity to enhance the usability of these cuts into products of higher added value. Then, it can be expected that higher contents of sulphur, metals and coke will put additional pressure on the operation of hydrotreaters in refineries.

- High quality (shorter chain) hydrocarbons are the most likely reserves to be soon depleted so lower quality reserves are expected to be exploited in a near future (Trambouze, 1993; Meyers, 1996). These oils will be of diverse origins and some will have a considerable content of small solids. Athabasca bituminous sands of Alberta can be recognized as a clear example of this situation.

This introduction is planned as follows. First, the deep bed filtration theory is presented along with methods for the calculation of the rate of collection. Among these methods, the trajectory analysis is presented in a more detailed manner because of its importance for this work.

Next, single phase and hydrodynamics of trickle bed reactors is presented stressing on what it is considered an important parameter for the collection of fines: the static liquid hold-up.

Finally, a historical perspective on the modeling of packed beds in single and trickle flow is reported.

1.2 Deep Bed Filtration (DBF) modeling

Deep bed filters have been used to remove polluting particles from drinking waters since the early 1800's. Although DBF is such an old technology, the mechanisms responsible for particle removal are not well understood and are still subject of intense research.

Particle trapping by a granular filter includes the following mechanisms: interception, straining, diffusion and impaction (Fig. 1-1). In liquid deep bed filtration, inertial forces are not important (Tien, 1989) and this mechanism is not found while in air filtration, impaction is an important mechanism.

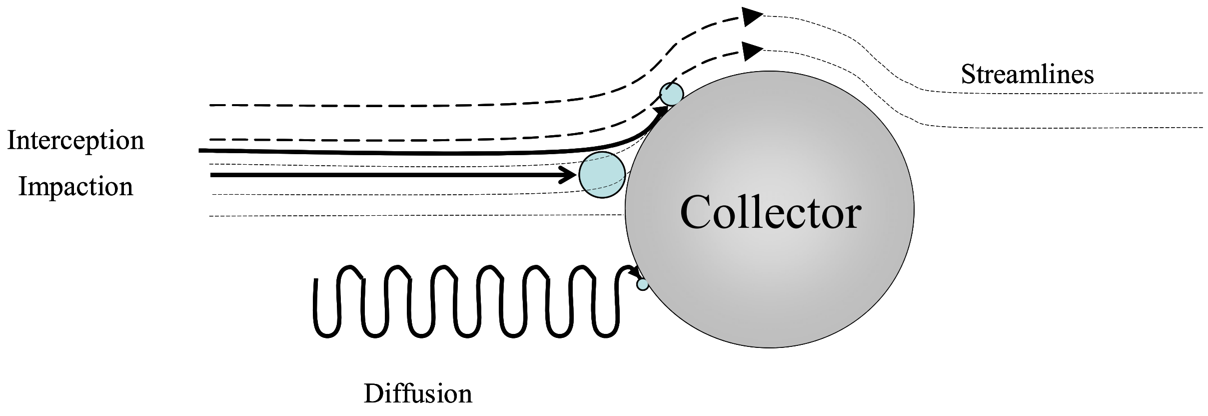

Figure 1.1 Deposition mechanisms in Deep Bed Filtration (DBF).

Elimelech and O'Melia (1990) divided the process of fine's deposition in two sequential steps: transport and attachment. In the first step, particles are transported from the bulk of the fluid to the vicinity of the collector. In the second step, attachment of particles is dominated by physicochemical-colloidal interaction actuated between the incoming particles and the surface of the collector. Interactions include electrical double-layer and Van der Waals forces depending on the physicochemical characteristics of the collector-liquid-particle system.

Brownian size particles (<1 μm) transport is dominated by convection and diffusion (Elimelech and O'Melia, 1990; Tien, 1989). In the case of medium size particles (1 μm $<d_p<$10 μm), the transport process is dominated by physical forces (gravity and fluid drag) and by interception due to the finite size of the particles (Yao et al. (1971); Tien (1989)).

DBF analysis and modeling was mainly empirical until Herzig et al. (1970) developed the conservation equations that govern the process. A key parameter used in the DBF equation is the efficiency of deposition of fines that must be acquired or estimated by a particle capture model.

A wealth of theoretical models to estimate deposition efficiencies has been proposed so far in the literature. Models can be divided according to the following classification (Rege and Fogler, 1988):

- Empirical models
- Stochastic models
- Network models
- Trajectory Analysis

Excellent reviews on the subject can be found describing each model and pointing on their capabilities and limitations; e.g., Tien and Payatakes (1979), Herzig et al. (1970), Rege and Fogler (1988) and Burganos et al. (2001). In the following paragraphs only a brief summary is offered except for the Trajectory Analysis Model that is the most pertinent for this work, which is presented in a more extended way.

1.2.1 Empirical models

Empirical models solve a simplified filtration equation that includes simple laws involving empirical parameters developed from observational facts for the rate of deposition. Depending on the events observed during the filtration process, the rate of deposition is related to the initial or clean filter coefficient, a function of the velocity and concentration of fines and an eventual function for the detaching rate of particles. In the case of the filter coefficient and the rate of detachment, usually a vector of parameters is included. Most of these parameters must be obtained by retrofitting experimental data. Examples of empirical models can be found elsewhere (Tien, 1989; Herzig et al. 1970; Tien and Payatakes, 1979); while simple in nature, these models do not provide insights into the mechanisms and are naturally restricted to the cases for which they were developed.

1.2.2 Stochastic models

In this approach, probabilistic laws are applied to determine the extent of the blocked pores. The state of a pore (open or blocked) is considered an event whose probability is determined by solving a certain probability law related to the velocity of the fluid and the local permeability (Hsu and Fan, 1984). This model has parameters that must be obtained by retrofitting experimental data. By using this method it is not possible to predict effluent concentration histories thus its usefulness is rather limited.

1.2.3 Network models

In these models, the porous media structure is conceptualized as a random network, which is generated according to a certain geometry. Then, a random set of particles is generated at the entrance of the network and the fluid flow is calculated in every pore by solving the mass balance for every node. The particles are then transported through the nodes and their fate (capture or not) is determined according to a probabilistic law. This method tries to predict the effluent concentration profiles, the permeability changes and the filter coefficient. Though promising, the model does not use the velocity fields to calculate the filtration parameters and is somewhat limited in use; also many parameters (as many as six) are frequently needed (Gruesbeck and Collins, 1990).

1.2.4 The particle trajectory analysis (TA)

Based on ideas of Yao et al. (1971), Payatakes (1973) developed a methodology to estimate the rate of particle deposition using Lagrangian trajectory calculations. When a liquid contaminated with small particles flows through a granular bed, these particles (here after, the fines) can meet a bed element (collector) and, following the fluid streamlines generated in the fluid, impact on the collector. Knowledge of the forces acting on the incoming fines, their magnitude and the behaviour of the fines when they impact the collector enables, in principle, to estimate the rate of deposited fines.

In the TA approach, fines trajectories are calculated by constructing appropriate equations of motion that include the short and long range forces acting on a spherical fine. Depending on the distance separating the fine and the surface of the collector, long and short range forces are developed and are considered on the force balance affecting the fine. If the particle is far from the surface of the collector, the force balance will include gravity and the drag forces exerted by the liquid. When the particle is close to the collector (several fine diameters) short range forces such as the surface forces (London, Double Layer if present) will be included along with the gravity and liquid drag force. At the vicinity of the collector, the fine will rotate and therefore the torque given by the presence of the collector's surface need to be accounted for. Inertial forces are considered negligible in liquid deep bed filtration, so impaction is considered as a non existent collection mechanism (Figure 1-2.)

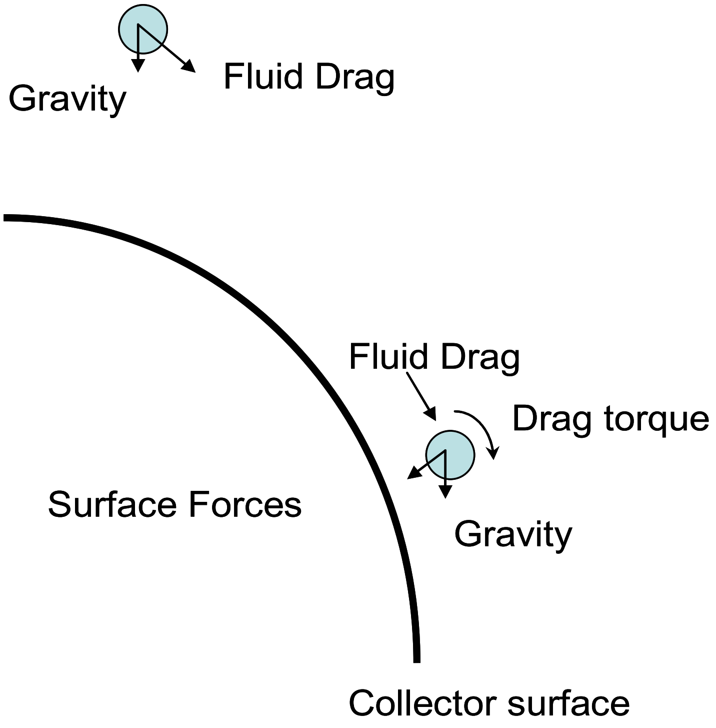

Figure 1.2 Forces acting far and close to the collector surface when a fine travels towards a collector.

To generalize the approach, Payatakes (1973), Payatakes et al. (1974), Rajagolapan and Tien (1976) and Tien and Payatakes (1979) have proposed several representations of the porous media. Different collector geometries (Figure 1.3) were used in which the flow field, affected by a periodically geometric packing of collectors in the neighborhood is known from theoretical fluid dynamics (isolated sphere, Happel sphere-in-a-cell model, capillary and constricted tube). Then, the collector geometry is included in the whole bed, considered as formed of unit bed elements (UBE) which, regularly repeated along the bed, represent the granular filter. In the sphere-in-cell model, the streamline function is then used to calculate the trajectory of all the particles in the unit bed collector. Forces acting on the fine such as gravitational, inertial, hydrodynamic, electric double layer and London-van der Waals are added to the streamline function.

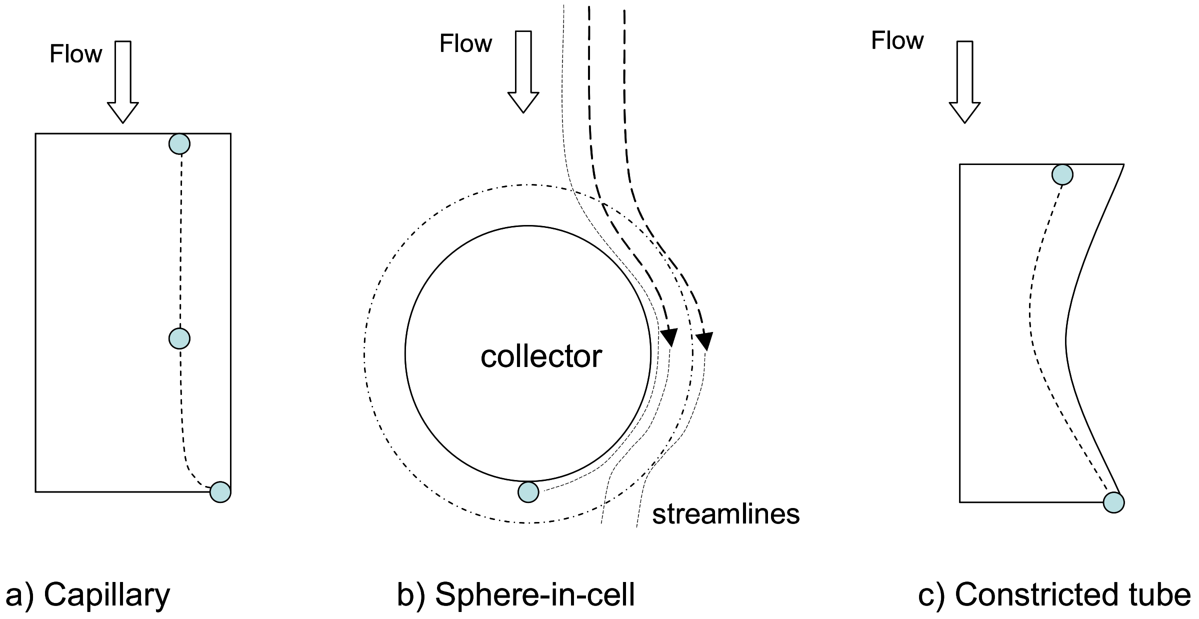

Figure 1.3 Proposed collector geometries and limiting trajectories for the calculation of collection efficiencies in single phase deep bed filtration.

Finally, to calculate the deposition efficiencies, another concept, the limiting trajectory, is employed to determine if a particle will make contact with the collector; if so, the touching particle and all those below its trajectory are considered to be captured. Depending on the geometrical model used in TA, the limiting trajectory is the trajectory of the fine that makes contact at the end of the representation of the collector (capillary model and constricted tube models) or the streamline that barely touches the collector at its farthest point (sphere-in-cell).

Numerical simulations are then performed and a correlation is determined for the range of variables of interest. The obtained expression is a function of dimensionless numbers accounting for the most pertinent variables such as gravity, relation between the size of particle and collector (interception) and London forces.

This analysis has made significant advances in the understanding of the underlying phenomena of the deep bed filtration process at the pore level and it is selected for the analysis of this work.

The force balance in the TA assumes that the fine-surface interaction does not change nor does the geometrical representation of the collector; this feature confines the originally presented method to represent clean packed beds only (Tien, 1989) however several other approaches have been proposed to improve the prediction capabilities of the method.

1.3 Modern extensions to the modeling of plugging of packed beds using TA

To overcome the disadvantages of the original method, Mackie et al. (1987) proposed a simplified TA based method in which the fines trajectories are found in a reduced dendritic modeling combined with a smooth coating mode geometry. Good qualitative and quantitative agreement with their experimental values was found. The model poorly behaves in advanced stages of plugging due to the fact that the Happel's sphere-in-cell model used for the unit filter is not adequate for severely clogged beds.

In 1995, Choo and Tien (Choo and Tien, 1995a, 1995b) published a fully predictive model for the whole operating cycle of the filter in non-Brownian conditions. The model extends Happel's concept to several sphere-in-cell models for various stages of filtration. In the first stage, the spherical collector is covered by a single layer of captured particles governed by classical TA. As deposition progresses, a second stage of collection is included by modifying the original collector shape. Then a sphere of larger diameter is superimposed but is displaced by a distance which is a function of the specific deposit, σ. Also, a porous layer of non-uniform thickness advances and covers the surface of the collector while preserving the spherical shape (See Figure1.4). Happel's model as well as the TA methodology are still valid and consequently applied. Collection efficiencies for the second stage are calculated considering that the controlling collection mechanism is by interception, as described in several experimental works (Ushiki and Tien, 1984; Yoshida and Tien, 1985).

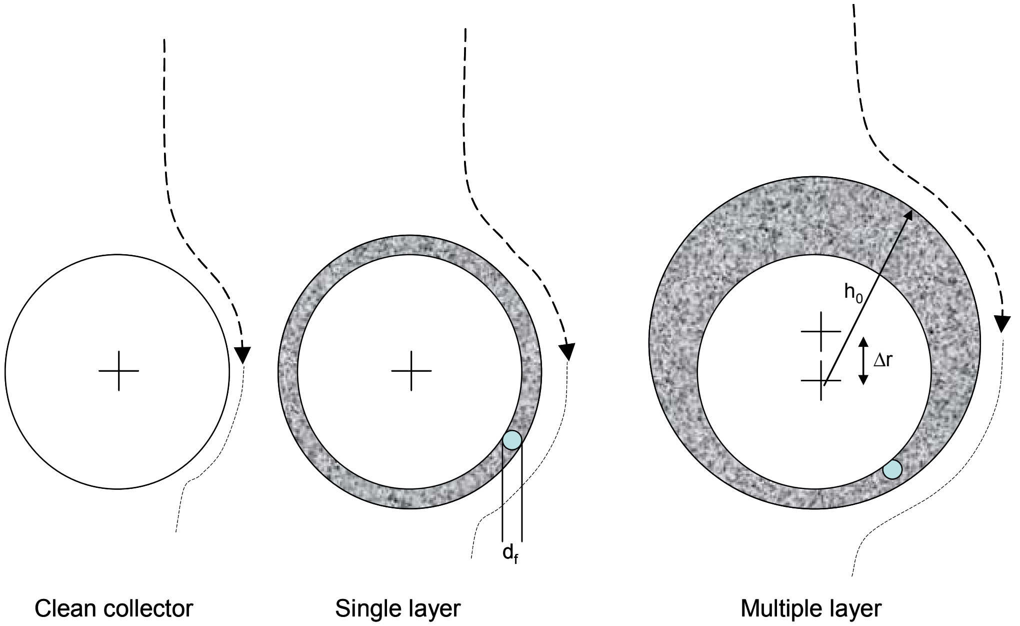

Figure 1.4 Geometrical representation of a spherical collector in the different filtering stages. Adapted from Choo and Tien (1995a, b).

Burganos et al. (2001) proposed a three dimensional hybrid simulation procedure which combines a network representation of the bed, as connected constricted tubes, with a 3-D trajectory analysis to calculate the transport and local rates of deposition of non-Brownian particles. Other concepts such as morphology, pore distribution, plugging, and detachment/redeposition mechanisms are also included in the simulator. Overall behaviour of filter parameters such as filter efficiency, loss of permeability and effluent concentration were found to follow characteristic filter tendencies and benchmarking included filtration trends in diverse nature systems.

The inclusion of the bed three dimensionality and accounting for the phenomenological characteristics of filtration resulted in a rather complex simulator. However the quality of the reported results makes evident that such an intricate procedure is indeed required for a better representation of deep bed filtration.

1.4 Other extensions

Applying the fundamental theorem of calculus and the mean-value theorem, Stephan and Chase (2000) re-obtained the volume averaged equations for the deep bed filtration process. In their development, a model for the specific area of the collector was proposed which accounts for the ‘shadow effect’ resulting from the deposited particles. This shadow effect makes unavailable for deposition a neighbouring area to the deposited fine due to the alteration of the incoming flow pattern streamlines (Stephan and Chase, 2000). Experiments were performed to validate the method obtaining good agreement with a model that included a term for a deposition/detachment case of the fines. This contribution reinforces the theoretical framework on which the DBF modeling is based. However, the fact that the averaged equations were developed for unsteady state in the fines transport equation but considering steady state in the momentum equation reduces its applicability (without modification), since DBF is an implicitly transient phenomenon. Then, the procedure allows following the fines concentration history but not the pressure drop.

1.5 Plugging in packed bed reactors in petroleum-like conditions

Led by M.R. Gray, the group of the University of Alberta has experimentally studied the plugging of packed beds in single and multiphase flows in refinery like conditions. In their first work, Narayan et al. (1997) studied the plugging of a packed column in single-phase conditions finding that the deposition mechanisms were akin to deep bed filtration. This finding allows application of knowledge available for DBF to the modeling in packed bed plugging. Carbon black and kerosene were used in the model to represent a refinery-like system.

Gray et al. (2002) experimentally studied the phenomena of fines deposition in packed beds operating in trickle, transitional and pulse two phase flow regimes using kerosene and kaolinite as system models. In both studies pressure drops changed as far as 800% as plugging developed in time. The authors held the porosity reduction as responsible of this variation.

Fang et al. (1998) presented an experimental study of the plugging of packed beds in trickle, transition and bubble flow conditions. Detailed descriptions of the morphology of deposits in single and two phase flows were presented and compared. The comparison of trickle two-phase flow experiments with deposition in single-phase flow indicated that the collection efficiency was one to two orders of magnitude less for the gas-liquid flow than in single-phase flow.

Fines deposition was highly dependent on the flow regime that determined the morphology of the deposits. It was well established that the gas flow rate had an effect on the filtration efficiency, which decreased when the gas flow rate was increased at constant liquid flow rate.

In single-phase flow, deposition of fines was highly dependent on the fine-fine interaction, giving rise to loose flock-like deposits localized in the points of contact of packing. In trickle flow the fine-fine interaction was not observed and the deposits were more dense and consolidated but as in the single phase case, a considerable deposition of fines was localized in the points of contact of the spheres of the bed where very low liquid renewal rates exist, i.e., where the static liquid holdup resides. (See Figure 1.5).

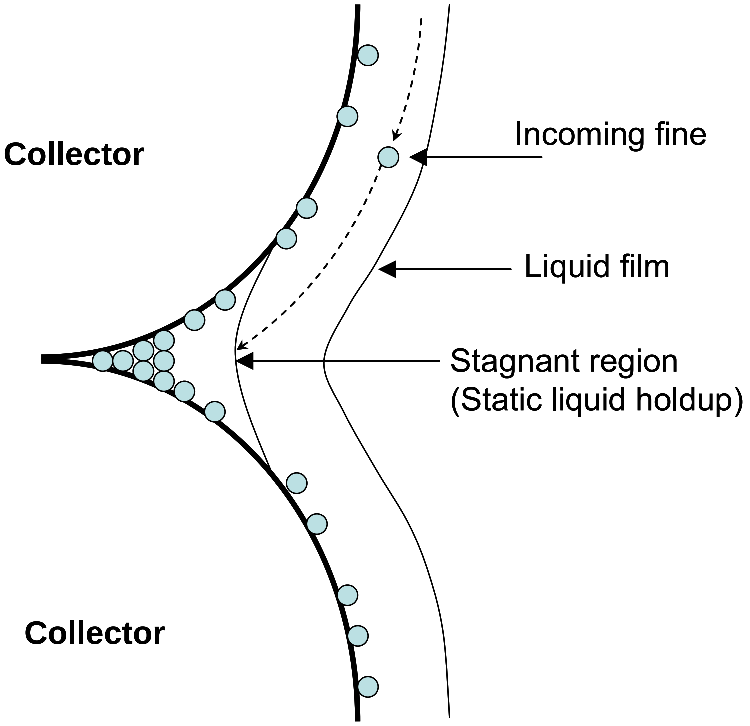

Figure 1.5 Schematics of the experimental observations of Fang et al. (1998) on the capture of fines in trickle flow in two phase refinery like conditions.

1.6 Modeling of plugging of packed beds operating in trickle flow.

A modeling effort for the plugging of packed beds in multiphase conditions was made by Iliuta et al. (2003). The authors proposed a model for the plugging of packed beds in which new expressions for the gas-liquid and liquid-solid hydrodynamic interactions were used. The model included an expression for the increase of the specific area and the reduction of the porous space by the collected fines to explain the increase of the pressure drop. Collection efficiency was estimated by the expression given by Rajagopalan and Tien (1976) for single-phase flow collection. A good match was found with the experimental data from Gray et al. (2002).

Classical DBF in granular filters and trickle bed reactors have differences that deserve to be noted: collector size ranges from 1 to 3 mm in typical TBR while in granular beds collectors can vary from 0.5 to 2 mm (Tien, 1989). DBF filters are usually 1 m in height while TBR of up to 10 m and 2 m of diameter are common. Larger space hourly velocities are observed in TBR's (Iliuta et al., 2003) influenced by packing and vessel size. Flow liquid velocities in TBR's are typically between 0.001 and 0.05 m/s while in granular beds they are less than 0.001 m/s. Liquid (and gas) velocities are such that in granular beds the law of Darcy applies (Iliuta et al., 2003) while in TBR the inertial effects cannot be ignored (Saez and Carbonell, 1985).

To our knowledge, so far no expressions or models for the particle collection of packed beds in gas-liquid trickle flow conditions have been yet reported in the literature. As result of the presence of a gas-liquid interface, the description of the phenomenon is more complicated but the same collection mechanisms are expected to exist.

1.7 Packed bed reactors

Cylindrical columns in which small solid pieces are placed in random or structured fashion are commonly called packed bed reactors. These reactors are extensively used in many industries, including chemical, petrochemical, petroleum refineries, wastewater treatment, fine chemicals manufacture, etc.

Packed beds operating in single or multiple phase conditions are commonly used in separation, reaction and purification processes resulting of their great versatility (Froment and Bishop, 1990; Dudukovic et al. 1999, 2002; Boelhouwer, 2001). Due to their importance, fixed bed reactors with catalytic active packing, in which heterogeneous reactions take place, deserve special attention. It is this feature which allows the production of many chemicals of interest that otherwise would be difficult or impossible to produce.

1.7.1 Single phase packed bed reactors.

Fixed bed catalytic reactors operating with gas or liquid are one of the most widely used industrial reactors for heat and mass transfer, with or without chemical reaction. Froment and Bishop (1990) present a large list of refining and petrochemical processes hosted by fixed bed reactors and list the key improvements that have led to the success in their application. Spheres, Raschig rings, Berl saddles, trilobe or extruded catalysts are commonly used as packing elements for the fixed bed.

One of the first questions to be addressed in designing a packed bed reactor, is the heat transfer mode prevailing in the reactor. This choice is crucial as the operation of the reactor can be complicated by the presence of hotspots and eventually, by the probability of runaways when the catalytic reaction is highly exothermic. Adiabatic, isothermal, non adiabatic-non isothermal modes can be considered as operation modes, but selection will be ruled by the thermal nature of the reaction.

If the adiabatic mode is selected, then a column of considerable diameter can be used but concerns on the maldistribution of the phases may arise. If a highly endothermic reaction develops in the reactor, the temperature will drop as reaction proceeds and the reaction can become unacceptably slow. For an exothermic reaction, the adiabatic reaction temperature may cause a shift on the rate equilibrium and therefore, the production of parasitic unwanted reactions.

If heat is continuously added or removed through the wall of the packed bed, then the diameter of the column must be small enough to avoid unacceptable radial temperature gradients. Once the basic disposition of the fixed bed reactor has been decided (adiabatic, multiple adiabatic reactors with interstage cooling, multitube continuously cooled, or some combination) then the reactor must be modeled to obtain a quantitative design.

1.7.2 Trickle Bed Reactors (TBR)

In a trickle bed reactor (Figure 1.6) gas and liquid streams flow concurrently downward a random or ordered packed bed at such velocities that the gas-liquid interactions vanish and the liquid trickles down the wall of the solid matrix while the gas fills the available porous space.

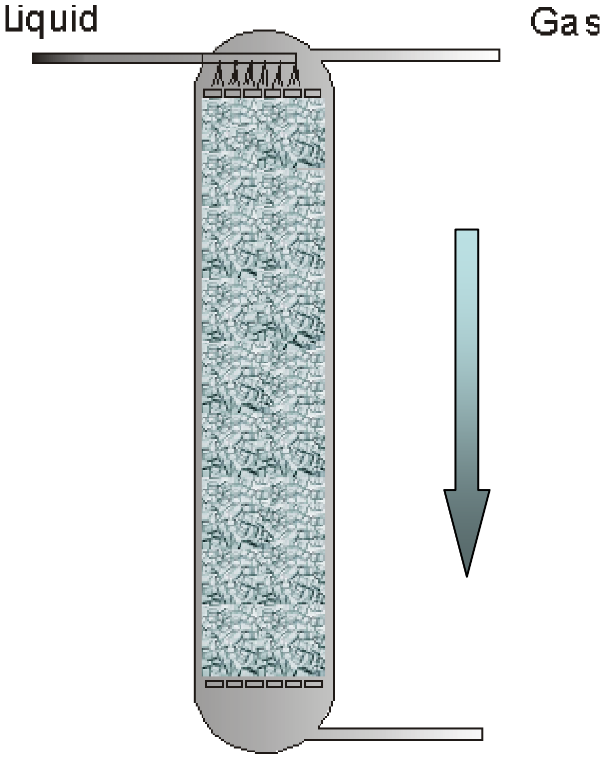

Figure 1.6 Schematics of a Trickle Bed Reactor.

An ample diversity of processes for producing or separating chemical species have been developed using trickle packed bed reactors and many examples can be found in many industries (Dudukovic et al. 1999; Dudukovic et al. 2002). The importance of multiphase reactors is such that it is widely considered that the efficiency of the reactor operation often dictates the economy and feasibility of the process in which the reactor is involved (Dudukovic et al. 2002). Literature devoted to the description of the hydrodynamic and many other aspects of trickle bed reactors is vast, and several excellent reviews are available (Ramachandran and Chaudhari 1983; Saroha and Nigam 1996; Dudukovic et al. 1999; Dudukovic et al. 2002).

Besides the difficulties resulting from the intricacy of the inner geometry of the porous bed, other complex issues must be resolved when trying to understand and model multiphase packed bed reactors. Suffice to mention for example, the fluid-fluid and fluid-solid (gas-liquid-solid) interactions (flow regimes) and the presence of complex fluid-particle contacting phenomena (partial wetting and static liquid holdup).

1.7.2.1 Flow regimes.

When gas and liquid phases are present in the void space of the porous packed bed, several flow regimes may develop depending on the velocities and transport properties of the gas and liquid as well as on the characteristics of the packing material. Broadly, flow regimes are classified in high and low interaction regimes. The low interaction regime is also called trickle flow regime and has been already defined. The high interaction regimes include many different flow patterns: pulsing, wavy, dispersed bubbly, spray, etc. Charpentier and Favier (1975) presented diagrams for foaming and non-foaming liquids in which the transition from one flow pattern to another were shown as a function of gas and liquid flow rates. Lines bounding the flow patterns were considered as transition regimes rather than points of abrupt change.

1.7.2.2 Wetting efficiency.

Wetting efficiency can be defined as the fraction of external catalyst area covered by the flowing liquid film (Al-Dahhan et al. 1997). Two scales are distinguished to analyze partial wetting: bed and packing scale. At bed scale, deficiencies in the liquid distributor design are mainly the cause. At particle scale it is the result of insufficient liquid mass velocity to cover catalyst particles with a continuous liquid film (Dudukovic et al. 2002) (Figure 1.7).

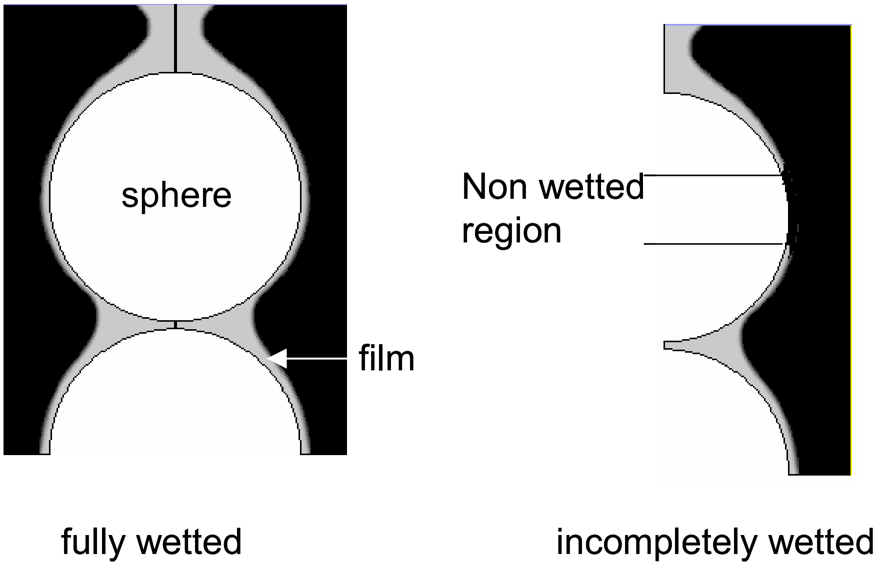

fully wetted incompletely wetted

Figure 1.7 CFD-VOF (Volume-Of-Fluid) axysymmetrical simulations of gas-liquid trickle flow over spheres showing complete and incompletely wetted regions. A liquid-solid contact angle of 25 degrees was used.

Reaction rate over incompletely covered catalytic particles can be smaller or greater than the rate observed on completely wetted packing. This depends on whether the limiting reactant is present only in the liquid phase or in both, gas and liquid phases. If the reaction is liquid limited and the liquid reactant is non-volatile, then a decrease in the catalyst-liquid contacting reduces the surface for mass transfer between the liquid and the catalyst causing a decrease in the reaction rate. But, if reactants are volatile and significant heat effects exist, then a gas phase reaction can occur on the dry solid area and consequently a higher reaction rate is observed. Such higher rate is also achieved in case of gas-limited reactions where gas reactant can access the catalyst pores from the externally dry area (Saroha and Nigam, 1996).

1.8 Static Liquid Holdup (SLH)

The amount of liquid in a given time plays an important role in the hydrodynamics as well as in the heat and mass transfer of the multiphase reactors.

Total liquid hold-up is usually divided in two categories: dynamic and static (Shulman et al. 1955; Goto and Smith, 1975). Two types of static external liquid holdup are currently mentioned in the literature, depending on the measuring approach used and are defined accordingly. The static liquid holdup can be measured by bed drainage or by a tracer method. The basic difference between both methods is that in the latter, the column hydrodynamics is not disturbed which is not the case for the draining method. Then, the liquid in the static holdup can be considered either being totally stagnant (draining method) or flowing at a much lower velocity than the dynamic liquid holdup (tracer method).

A controversial issue that arises is whether the static liquid holdup measured by draining the bed agrees with values obtained by the tracer method. Some authors have concluded that static holdup measured by either method is equivalent (Engel et al. 1997), while others have found fundamental differences (Kushalkar and Pangarkar, 1990; Schubert et al. 1986; Stanek and Kolar, 1973). Static liquid holdup in the draining method is the result of a balance of gravitational and capillary forces while the tracer method static liquid holdup is a function of the gas and liquid flow rates.

Draining is the most frequently used experimental technique. In this method the packing particles are assured to be well wetted by allowing the liquid to flow (or stay) in the bed for several hours. Once the wetting has been assured, the liquid (and gas) flow to the bed is suddenly stopped. The column is then weighed; the valve at the bottom of the column is then open and the liquid is allowed to flow until a fairly constant weight is reached. Finally, the static liquid holdup is calculated as the difference between these two weights (Figure 1.8). In some works, the liquid holdup is defined as the amount of liquid that stays in the bed after a 10, 15 or 50 minutes drainage, because after a few hours, small quantities of liquid might continue to drain (Shulman et al. 1955). This feature as well as the exactness of the weighing devices can be mentioned as potencial sources of experimental error. If a porous catalyst or packing is used, the porous volume must be subtracted.

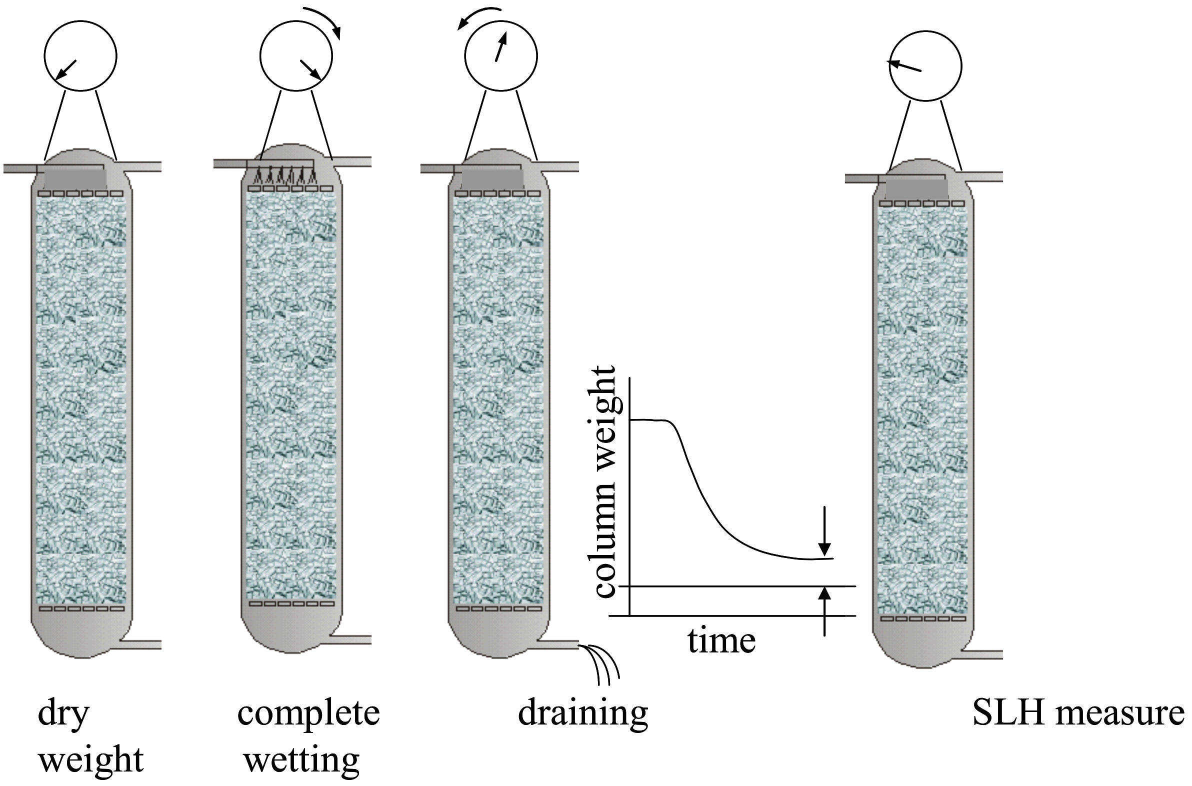

Figure1.8 Schematics of the experimental set-up for the measurement of the static liquid hold-up by the weighting method.

The static liquid holdup depends on several variables: geometry and size of the particles, method of packing of the column, physical properties of the liquid and the surface of the solid, capillary and gravitational forces, and physical and thermodynamic properties of the solid-liquid-gas system (Mao et al. 1993). Viscosity has been mentioned by several authors as a factor that can have a direct impact on the static liquid holdup. Shulman et al. (1955), correlated their experimental data with an expression that included the viscosity. Standish in 1968 found his data on liquid metals and aqueous solutions to be a function of viscosity. Goto and Gaspillo (1992) found that their data were ‘strongly dependent on the liquid viscosity'. This result can be explained by the work of Zisman (1964), which showed that liquid viscosity affects the adhesion of the liquid to the solid. In an opposite sense, some authors have stated the independence of static liquid holdup on the viscosity (Venkata-Ratnam and Varma 1992), or have obtained a weak effect (Shulman et al. 1955).

To date and despite its importance and applicability, not much effort has been directed to obtain a good predictive tool for static liquid holdup. As an example, it can be mentioned that some correlations for the external total liquid holdup (Kohler and Richarz, 1985; Stiegel and Shah, 1977) use static liquid holdup as a parameter. Saez and Carbonell (1985) used static liquid holdup to estimate the interfacial drag forces exerted on one phase by the others across the interfaces. Grosser et al. (1988) and Dankworth et al. (1990) used such expressions to build their models to estimate the hydrodynamic regime state of a trickle bed reactor. The work on theoretical models is scarce (Mao et al. 1993; Saez et al. 1991; Kramer, 1998) and results are still far from adequate. Contradictory values can be found and are difficult to predict, in part because of the complexity of the phenomena as well as to the difficulties encountered in the experimental work.

1.9 Modeling of single and trickle flow bed reactors

1.9.1 Single phase packed bed reactors

Modeling of these reactors has evolved naturally in time. In the earliest models, the bed was considered as an axial, one-dimensional flowing continuum. In some cases, the radial flow effects were disregarded (pseudo-homogeneous model) and the main gradients of concentration and temperature were considered to occur only in the axial direction. Then, the continuity, heat and momentum transfer equations are written, giving a set of ordinary differential equations. When ad-hoc closure terms were added, the set of equations were solved by suitable numerical methods.

When neglecting the radial effects of all the transport mechanisms, the one-dimensional models predict constant temperature and conversions in the cross section. This is an oversimplification for highly temperature-dependent reactions. In the two-dimensional pseudo-homogeneous models, the radial and axial processes are lumped in a single entity: the effective transport parameters for mass and heat transfer. This conceptualization of the packed bed reactor led to a great amount of efforts on the understanding, prediction and interpretation of such effective parameters. Results of this effort are many correlations that have limited success with data other than those from the publishing author and have led to many discussions on the pertinence of the use of such parameters (Dixon & Nijemeisland, 2001). Since most of the mentioned models rely on assumed ideal flow patterns and are one dimensional in nature, the accurate prediction of the operation and design of the packed bed reactors cannot be resolved with these approaches.

1.9.2 Modeling of trickle bed reactors

Crine et al. (1979), Melli and Scriven (1991) and Melli et al. (1990) studied the hydrodynamics of two phase flows at the pore scale using a simple flow visualization device in which the bed was represented by an ordered array of discs trapped between two transparent walls. Some rules were formulated and a complete bed scale model was obtained and solved. The two-dimensional model provided evidence on the relationship between the global hydrodynamics and the local (or pore) level states. Model results were found to be comparable with some experimental data but did not provide insights into the flow distributions in the bed (Jiang et al. 2002a).

In 1990, Holub presented the discrete cell model (DCM), which conceptualized the flow distribution in the bed as governed by the minimum total energy dissipation rate. Recently (Jiang et al. 2000a) the method was revisited and expanded by statistically assigning cell porosity values and by incorporating the interfacial tension force that relates to the particle wetting for two-phase flow in trickle beds. In the same study, the authors compared DCM and computational fluid dynamics (CFD) k-fluid models with experimental data obtaining a good agreement. In terms of computational efficiency, CFD approaches appeared to be superior since the optimization algorithms used in DCM have difficulties when dealing with large packed beds.

Holub in 1990, proposed a simplified phenomenological hydrodynamic model for the steady state, uniform two-phase gas-liquid co-current flow in the low interaction regime in trickle bed reactors. A single slit with an inclination angle, which is related to the bed tortuosity, models the complex actual porous space in a packed bed. The liquid flow completely wets the slit surface, forming a film whose thickness is proportional to the liquid holdup. This model has been successfully used to predict the pressure drop, the liquid holdup and the flow regime transition in gas-liquid trickle flow with acceptable accuracy (Holub et al. 1992, 1993). Several modifications have been proposed to increase the accuracy of the model (Iliuta et al. 1998, 2002) as well as to extend its prediction capabilities (Al-Dahhan et al. 1998; Iliuta et al. 2000).

A model somehow related to the CFD approach, is the two fluid model obtained by Attou et al. (1999). Using one-dimensional k-fluid averaged balance equations of continuity and momentum, the model accounts for the solid-liquid and liquid-gas interactions. In isothermal conditions and considering fully wetted particles, the authors obtained an Ergun-like model for single and two phase flows that gave good results when compared with experimental data.

Deficiencies in the reaction kinetics, overlooking of the spatial and temporal nature of the transport parameters and its dependency on the flow patterns developed in the porous structure of the packed bed can be cited as limitations for the success of these methods. Use of Computational Fluid Dynamics (CFD) for the modeling of packed beds is a promising methodology to overcome the mentioned limitations.

1.9.1.1 Computational Fluid Dynamics (CFD) modeling of packed beds

Packed beds modeling in CFD has been accomplished by means of several methodologies. Depending on the scale of the flow pattern to be modeled (local or global), mainly two approaches have been used so far.

1.9.1.2 Direct Numerical Simulation (DNS)

Logtenberg and Dixon (1998), Nijemeisland et al. (1998), Dixon and Nijemeisland (2001) developed 3D simulations using spheres of 2-5 cm of diameter in tubes of small column/particle diameter ratio (2 to 3 approx.) to model the heat transfer in packed beds. Though the porous space is well represented and local valuable information can be obtained, the transition to a whole bed scale is still out of reach.

Other works using similar approaches have been used to study the flow field and pressure drop in structured beds (Calis et al. 2001) and radial dispersion (Schnitzlein, 2001).

This approach can be considered more universal, but present computers and models make impossible to model a full scale packed bed having a small particle/column diameter ratio and where several thousands or millions of packing particles must be accounted for. Another problem is the inclusion of more than one phase that could require additional modeling of the interface and a far more intense use of the computer. Therefore, another strategy must be applied to include the bed structure into the model to be solved.

1.9.2.3 Euler-Euler k-fluid modeling of packed beds

To represent multiphase flows, Anderson and Jackson (1967) and Ishii (1975), derived conservation equations for mass, momentum and energy transfer by ensemble averaging the local instantaneous conservation expressions for each phase. This formulation derived for Euler-Euler models has the following assumptions and characteristics:

- Phases are considered as interpenetrating continua.
- Existence of a phase at certain point is determined by its volume fraction.
- In every point, the sum of all volume fractions is unity.
- All phases are considered non-compressible.
- A single pressure field is generated for all phases.
- Continuity and momentum transfer equations are solved for each phase.
- Momentum transfer between phases is included in a drag term determined by the local slip velocity between phases.
- Other flow characteristics are modeled separately (turbulence, mass transfer, etc.)

Initially developed to model fluidized beds, this approach has been used to model other multiphase systems. In approaching packed bed reactors, the porous matrix is included in the model by imposing a constant volume fraction for the solids and the momentum transfer between fluid and solid is included using an Ergun-like expression. Due to the averaging of the flow variables over a certain volume, we expect to obtain only large-scale (averaging volume) flow structure using this approach.

An Eulerian k-fluid model has been used in a number of works with considerable success to study packed bed columns: multiphase flow textures in trickle beds (Jiang et al. 2001), mass transfer in random packed distillation columns (Yin et al. 2000), hydrodynamics in distillation tray columns (Van Baten et al. 2001), maldistribution of flows in packed bed columns (Sun et al. 2000; Jiang et al. 1999) and single phase and multiphase flow in random packed beds (Jiang et al. 2000, 2002a, 2002b),

It is well known that the successful application of such simulations to multiphase flow is mainly dependent on the appropriate closure laws for the inter-phase transport of mass, momentum and energy (Kuipers and van Swaaij, 1998). For modeling multiphase flow in packed beds, additional efforts are needed as discussed above, to better approximate and implement the porosity structure of packed beds into the model equations.

1.9.2.4 Insertion of the random bed structure in an Eulerian-Eulerian CFD code

The implementation of the porosity distribution in flow simulation increases the level of difficulty in packed beds as compared with other multiphase reactors. So far, this issue has been mainly tackled in a deterministic and simplified manner. For example, either uniform porosity or radial porosity variations are considered in the bed model (Bey and Eigenberger, 1997; Yin et al. 2000). In some cases, a multi-zone porosity assignment was used (Stanek, 1994). Since the 3-D interstitial pore space varies with repacking the bed, the porosity distribution possesses a statistical nature (Wijngaarden and Westerterp, 1992) and the use of a statistical description of the porosity structure in the flow model has considerable potential for success (Crine et al. 1992; Jiang et al. 1999).

Jiang et al. (1999) used a porosity model partitioning the 3-D pore space into sections and assigning to each section a porosity distribution. An initial solid phase volume fraction is assigned to every section and then the flow distribution is simulated with a CFD methodology. Depending on the section size chosen for the partition, the section porosity values follow a certain probability density function. That means that the probability function is assumed section-size dependent. The authors used the results from Chen et al. (2001) and from Sederman and Gladden (2001), in which a Gaussian distribution or a nearly binomial type of section porosity distribution was used. With these results, the porosity distribution was assigned.

1.10 Objectives of this work

Plugging of multiphase packed beds when processing with fluids polluted with small particles in petroleum-like conditions demands for new models and approaches to this phenomenon.

The intent of this work is to develop new modeling approaches and to explore simulation tools such as CFD, for the study of the plugging of packed bed reactors in single and two phase trickle flow conditions. CFD is proposed as a tool of choice for the solution of a naturally multidimensional and transient process such as plugging of packed beds.

There is also a necessity to fill the gap within the fine deposition in single phase and gas-liquid trickle flow. So, one of the main objectives of this work is to expand the single phase capture models to the multiphase case.

Multiphase flows in packed bed presents unique hydrodynamic characteristics that must be accounted for in a comprehensive plugging model, such as static liquid holdup and partial wetting. This work was originally designed to include the static liquid holdup into the fines capture equation but due to time restrictions on the research, only a modeling effort for the static liquid was possible. So, this work must be considered as a first attempt on this direction and is expected to serve as inspiration for its continuation by an interested reader.

This thesis is divided in four chapters. The first chapter is devoted to present a general introduction on the deep bed filtration problem and a synopsis on the modeling of plugging. Also modeling and hydrodynamics of packed bed reactors are reviewed.

Chapter two deals with the exploration of an Eulerian-Eulerian CFD code as a tool of choice for the description of the transient behaviour and multidimensionality of the DBF phenomena in single phase packed beds operating with non-aqueous liquids. Also a modified collector area and porosity reduction models are proposed to explain the pressure drop and loss of permeability in the operation of the bed.

Chapter three presents a new model formulation for the calculation of deposition efficiencies in trickle flow using the model of Holub (1990) to represent the porous media and an implementation of the Trajectory Analysis algorithm as given in Payatakes et al. (1974). The efficiencies obtained are imbedded in a Eulerian-Eulerian CFD code to complete the full-scale description of the deposition on trickle bed reactors.

Chapter four is focused on the presentation of an algorithm to describe and calculate the Static Liquid Holdup using a Neural Networks correlation allowing using the contact angle as input parameter.

Chapter five presents the conclusions and general recommendations for the continuation of this work.

References

Al-Dahhan M.H., Larachi F., Dudukovic M.P. and Laurent A. (1997) High pressure trickle bed reactors; A review. *Ind. Eng. Chem. Res.* **36**, 3292.

Al-Dahhan M.H., Khadilkar M.R., Wu Y. and Dudukovic M.P. (1998) Prediction of pressure drop and liquid holdup in high pressure trickle bed reactors. *Ind. Eng. Chem. Res.* **37**, 793.

Anderson T. B. and Jackson R. (1967) A fluid dynamical description of fluidized beds. *Ind. Eng. & Chem. Fund.* **6**, 527.

Attou A., Boyer C. and Ferschneider G. (1999) Modeling of the hydrodynamics of the cocurrent gas-liquid trickle flow through a trickle-bed reactor. *Chem. Eng. Sci.* **54**, 785.

Bey O. and Eigenberger G. (1997) Fluid flow through catalyst filled tubes, *Chem. Eng. Sci.* **52,** 1365.

Boelhouwer J.G. (2001) Non-steady operation of trickle bed reactors. Doctoral Thesis. Technische Universiteit Eindhoven.

Burganos V.N., Skouras E.D., Paraskeva C.A. and Payatakes A.C. (2001) Simulation of the dynamics of depth filtration of non-Brownian particles. *AIChE J.* **47**, 4. 880.

Calis H.P.A., Nijenhuis J., Paikert B.C. Dautzenberg F.M. and van den Bleek C. M. (2001) CFD modelling and experimental validation of pressure drop and flow profile in a novel structured catalytic reactor packing. *Chem. Eng. Sci*. **56**, 1713.

Charpentier J.C. and Favier M. (1975) Some liquid holdup experimental data in trickle-bed reactors for foaming and nonfoaming hydrocarbons. *AIChE J.* **21**, 1213.

Chen J., Rados N., Al-Dahhan M. H., Dudukovic M. P., Nguyen D. and Parimi K. (2001) Particle motion in packed/ebullated beds by Ct and CARPT. *AIChE J.* **47**, 994.

Choo C.U. and Tien C. (1995a) Simulation of hydrosol deposition in granular media. *AIChE J.* **41**, 1426.

Choo C.U. and Tien C. (1995b). Analysis of the transient behavior of deep-bed filtration. *J. Colloid Interface Sci.* **169**, 13.

Crine M, Marchot P. and L'Homme G. A. (1979) Mathematical modeling of the liquid trickling flow through a packed bed using the percolation theory. C*omp. Chem. Eng.* **3**, 515.

Crine M., Marchot P. and L′Homme G. (1992) Statistical hydrodynamics in trickle flow columns. *AIChE J.* **38**, 136.

Dankworth D. C., Kvrekidis I. G. and Sundaresan S. (1990) Dynamics of pulsing flow in trickle beds. *AIChE J*. **36**, 605.

Daszkowski T. and Eigenberger G. (1992) A revaluation of fluid flow, heat transfer and chemical reaction in catalyst filled tubes. *Chem. Eng. Sci*. **47**, 2245.

Dixon A. G. and Nijemeisland M. (2001) CFD as a design tool for fixed bed reactors. *Ind. Eng. Chem. Res.* **40**, 5246.

Dudukovic M. P., Larachi F. and Mills P. L. (1999) Multiphase reactors: revisited. *Chem. Eng Sci*. **54**, 1975.

Dudukovic M.P., Larachi F. and Mills P.L. (2002) Multiphase catalytic reactors. A perspective on current knowledge and future trends. *Cat. Rev. Sci. Eng*. **44**, 1, 123.

Elimelech M. and O'Melia C.R. (1990) Kinetics of deposition of colloidal particles in porous media. *Env. Sci. Tech.* **24**, 1528.

Engel V., Stichlmair J. and Geipel W. (1997) A new model to predict liquid holdup in packed columns, using data based on capacitance measurements techniques. *Eng. Inst. Chem*. **N142**, 939-947. Simposium Series.

Fang J., Chung K, Masliyah J. and Gray M.R. (1998) Characteristics of particle filtration from gas-liquid flow by packed beds. Personal Comunication.

Froment G.F. and Bishop K.B. (1990) Chemical reactor analysis and design. 2nd Edition. John Wiley & Sons.

Goto S. and Gaspillo P. D. (1992) Multiple hydrodynamic states in gas-liquid upflow and downflow through beds of small packings. *Ind. Eng. Chem. Res.* **31***,* 629.

Goto S. and Smith J. M. (1975) Trickle Bed Reactor Performance. Part I. Holdup and Mass Transfer Effects. *AIChE J.* **21***,* 706.

Gray M.R., Srinivasan N. and Masliyah J.H. (2002) Pressure buildup in gas-liquid flow through packed beds due to deposition of fine particles. *Can. J. Chem. Eng.* **80**, 346.

Grosser K. A., Carbonell R. G. and Sundaresan S. (1988) Onset of pulsing in two-phase cocurrent downflow through a packed bed. *AIChE J.* **34**, 1850.

Gruesbeck C. and Collins R.E. (1990) Entrainment and deposition of fine particles in porous media. *SPE Reprint Series –Formation Damage*. 103.

Herzig J.P., Leclerc, D.M. and LeGoff P. (1970) Flow of suspensions through porous media. Application to deep bed filtration. *Ind. Eng. Chem.* **62**, 8-35.

Holub R. A. (1990) Hydrodynamics of trickle bed reactors. *Doctoral Thesis*, Washington University in St. Louis, MO, USA.

Holub R.A., Dudukovic M.P. and Ramachandran P.A. (1992) A phenomenological model for pressure drop, liquid holdup and flow regime transition in gas-liquid trickle flow. *Chem. Eng. Sci.* **47**, 2343.

Holub R.A., Dudukovic M.P., and Ramachandran P.A. (1993) Pressure drop, liquid holdup, and flow regime transition in trickle flow. *AIChE J.* **39**, 2, 302.

Iliuta I., Larachi F. and Grandjean B.P.A (1998) Pressure drop and liquid holdup in trickle flow reactors: Improved Ergun constants and slip correlations for the slit model. *Ind. Eng. Chem. Res.* **37**, 4542.

Iliuta I., Larachi F. and Al-Dahhan M.H. (2000) Double slit model for partially wetted trickle flow hydrodynamics. *AIChE J.* **46**, 597.

Iliuta I., Grandjean B.P.A. and Larachi F. (2002) New mechanistic film model for pressure drop and liquid holdup in trickle flow reactors. *Chem. Eng. Sci.* **57**, 3359.

Iliuta I., Larachi F. and Grandjean B.P.A. (2003) Fines deposition dynamics in gas-liquid trickle flow reactors. *AIChE J.* **49**, 485.

Ishii M. (1975) Thermo-fluid dynamic theory of two-phase flow. Eyrolles, Paris.

Jiang Y., Khadilkar M.R., Al-Dahhan M. H. and Dudukovic M. P. (1999) Two-phase flow distribution in 2D trickle-bed reactors. *Chem. Eng Sci*. **54**, 2409.

Jiang Y., Khadilkar M.R., Al-Dahhan M. H. and Dudukovic M. P. (2000) Single phase flow modeling in packed beds: discrete cell approach revisited. *Chem. Eng Sci*. **55**, 1829.

Jiang Y., Al-Dahhan M.H. and Dudukovic M. P. (2001) Statistical characterisation of multiphase flow textures in trickle beds. *Chem. Eng. Sci.* **56**, 1647.

Jiang Y., Khadilkar M.R., Al-Dahhan M.H. and Duddukovic M.P. (2002a) CFD of multiphase flow in packed bed reactors: I. k-fluid modeling issues. *AIChE J.* **4**, 701.

Jiang Y., Khadilkar M.R., Al-Dahhan M.H. and Duddukovic M.P. (2002b) CFD of multiphase flow in packed bed reactors: II. Results and applications. *AIChE J.* **4**, 716.

Kohler M. and Richarz W. (1985) Investigation of Liquid Holdup in Trickle Bed Reactors. *Germ. Chem. Eng.* **8***,* 295.

Kramer G.J. (1998) Static liquid hold-up and capillary rise in packed beds. *Chem. Eng. Sci.* **53,** 2985.

Kuipers J. A. M. and van Swaaij W. P. M. (1998) Computational fluid dynamics applied to chemical reaction engineering. *Advances in Chemical Engineering*, Vol 24, edited by Wei J. et al. Academic press, 227.

Kushalkar K. B. and Pangarkar V. G. (1990) Liquid Holdup and Dispersion in Packed Columns. *Chem. Eng. Sci.* **45***,* 759.

Logtenberg S. A. and Dixon A. G. (1998) Computational fluid dynamics studies of Fixed-bed heat transfer. *Chem. Eng Proc*. **37**, 7.

Mackie R.I., Horner R.M.W. and Jarvis R.J. (1987) Dynamic modeling of deep-bed filtration. *AIChE J.* **33**, 1761.

Mao Z. S., Xiong T.Y. and Chen J. Y. (1993) Theoretical prediction of static liquid holdup in trickle bed reactors and comparison with experimental results. *Chem. Eng. Sci.* **48***,* 2697.

Melli T. R., Santos J. M., Kolb W. B. and Scriven L. E. (1990) Cocurrent downflow in networks of passages: Microscale roots of macroscale flow regimes. *Ind. Eng. Chem. Res.* **29**, 2367.

Melli T. R. and Scriven L. E. (1991) Theory of two-phase cocurrent downflow in networks of passages. *Ind. Eng. Chem. Res.* **30**, 951.

Meyers R.A. (1996) *Handbook of petroleum refining processes*. 2nd edition, McGraw-Hill, New York.

Narayan R, Coury J.R., Masliyah J.H. and Gray M.R. (1997) Particle capture and plugging in packed-bed reactors. *Ind. Eng. Chem. Res.* **36**, 4620.

Nijemeisland M., Logtenberg A. and Dixon A. G. (1998) CFD studies of wall-region fluid flow and heat transfer in a fixed bed reactor. *AIChE Annual Meeting*, Paper 311f, Miami, FL.

O'Melia C.R. and Ali W. (1978) The role of retained particles in deep bed filtration. *Prog. Wat. Tech.* **10**, 167.

Payatakes A.C. (1973) A new model for granular porous media –application to filtration through packed beds. *Doctoral Thesis*, Syracuse University, NY.

Payatakes A.C., Rajagopalan R. and Tien C. (1974) Application of porous media models to the study of deep filtration. *Can. J. Chem. Eng.* **52**, 722.

Rajagopalan R. and Tien C. (1976) Trajectory analysis of deep bed filtration with the sphere-in-cell porous media model. *AIChE J.* 22. **3**, 523.

Ramachandran P.A. and Chaudhari, R.V. (1983) Three phase catalytic reactors. Gordon and Breach Science Publishers. Philadelphia.

Ranade V.V. (2002) Computational flow modeling for chemical reactor engineering. Process system engineering series, vol. 5. Academic Press, San Diego, CA.

Rege S.D. and Fogler H.S. (1988) A network model for deep bed filtration of solid particles and emulsion drops. *AIChE J.* 11, **34**, 1761.

Saez A. E. and Carbonell R. G. (1985) Hydrodynamic parameters for gas-liquid cocurrent flow in packed beds. *AIChE J.* **31**, 52.

Saez A. E., Yepes M., Cabrera C. and Soria E. M. (1991) Static liquid holdup in packed beds of spherical particles. *AIChE J.* **37***,* 1733.

Saroha A.K. and Nigam K.D.P. (1996) Trickle bed reactors. *Rev. Chem. Eng.* **3-4**, 207.

Schnitzlein K. (2001) Modelling radial dispersion in terms of the local structure of packed beds. *Chem. Eng. Sci.* **56**, 579.

Schubert C.N., Lindner J.R. and Kelly R.M. (1986) Experimental methods for measuring static liquid holdup in packed beds. *AIChE J.* **32**, 1920.

Sederman A. J. and Gladden L. F. (2001) Magnetic Resonance Imaging as a quantitative probe of gas-liquid distribution and wetting efficiency in trickle bed reactors. *Chem. Eng. Sci.* **56,** 2615.

Shulman H. L., Ullrich C. F. and Wells N. (1955) Performance of Packed Columns I. Total, Static and Operational Holdups. *AIChE J.* **1***,* 247.

Standish N. (1968) Some Observations on the Static Holdup of Aqueous Solutions and Liquid Metals in Packed Beds. *Chem. Eng. Sci.* **23***,* 945.

Stanek V. (1994) *Fixed Bed Operations: flow distribution and efficiency*. Ellis Horwood Series in Chemical Engineering.

Stanek V. and Kolar V. (1973) A model of the effect of the distribution on liquid holdup in a packed bed and a new concept of static hold-up. *Chem. Eng. J.* **5,** 51-60.

Stephan E. and Chase G. (2000) Development of volume-average theory for deep-bed filtration. *AIChE J.* **46**, 1918.

Stiegel G. J. and ShahY. T. (1977) Backmixing and liquid holdup in a gas-liquid co-current upflow packed column. *Eng. Chem. Proc. Des. Dev.* **16***,* 37.

Sun C.G., Yin F.H., Afacan A., Nandakumar K. and Chuang K.T. (2000) Modelling and simulation of flow maldistribution in random packed columns with gas-liquid countercurrent flow. *Chem. Eng. Res. Des. Trans. Ch. E. Part A.* **78**, 378.

Tien C. (1989) *Granular filtration of aerosols and hydrosols.* Butterworths series in Chemical Engineering. Boston MA.

Tien C. and Payatakes A. C. (1979) Advances in deep bed filtration*. AIChE J.* **25**, 9, 737.

Trambouze P. (1993) Engineering of hydrotreating processes. In *Chemical reactor technology for environmentally safe reactors and products*. (pp. 425-442). NATO Ser. E, Applied Sciences, Eds. H.I. De Lasa, G. Dogu, A. Ravella.

Ushiki K. and Tien C. (1984) In situ observation of aerosol filtration in a two dimensional model filter. *Am. Inst. Chem. Eng. Symp. Ser*. **80**, 137.

Van Baten J.M., Ellenberg J. and Krishna R. (2001) Hydrodynamics of reactive distillation tray column with catalyst containing envelopes vs. CFD simulations. *Catalysis Today.* **66**, 233.

Venkata-Ratnam G. and Varma Y. (1992) Liquid holdup in gas liquid co-current downflow through packed beds. *Can. J. Chem. Eng.* **70***,* 580.

Wijngaarden R. J. and Westerterp K. (1992) The statistical character of packed-bed heat transport problems. *Chem. Eng Sci.* **47**, 3125.

Yao K.M., Habibian M.T. and O'Melia C.R. (1971) Water and waste water filtration: Concepts and applications. *Env. Sci. Tech*. **5**, 1105.

Yin F.H., Sun C., Afacan A., Nandakumar K. and Chuang K.T. (2000) CFD modeling of mass-transfer processes in randomly packed distillation columns. *Ind. Eng. Chem. Res.* **39**, 1369.

Yoshida H. and Tien C. (1985) Dynamic behavior of aerosol filtration in a two dimensional filter. *Aerosol Sci. Technol.* **4**, 365.

Zisman W. A. (1964) Relation of equilibrium contact angle to liquid and solid constitution. *Adv. Chem. Ser*. **43**, 1.

CHAPTER 2

Modeling of Clogging of single phase packed bed reactors

Résumé

Quand des liquides pollués par des solides de petite taille à concentration faible sont traités dans des réacteurs à lit fixe, le colmatage se développe et commence à restreindre l'écoulement de manière sévère. Ce phénomène s’appelle filtration en profondeur (en anglais *deep bed filtration*, DBF), et on peut le rencontrer dans des procedés incluant l'hydrotraitement et l’hydrocraquage des sables bitumeux dans des réacteurs à lit fixe. Dans ces réacteurs, les particules non filtrables, sont la cause du disfonctionnement par colmatage. Les solides peuvent être d’origines diverses, par exemple, l’argile trouvée sur le lieu d’extraction ou le coke produit pendant l’opération. Un modèle transitoire détaillé et prédictif type mécanique des fluides numérique (en anglais *computational fluid dynamics*, CFD) est proposé pour décrire la filtration en profondeur. Plus spécifiquement, une approche Euler-Euler est donc formulée pour la description de l'évolution dans l’espace et le temps du colmatage se développant en filtration en profondeur de liquides non-aqueux contenants des particules. Une formulation est proposée pour la variation locale de la loi logarithmique macroscopique de filtration, ainsi qu'un modèle géométrique pour la surface spécifique efficace pour l'échange de quantité de mouvement. Des mécanismes de capture types monocouche et multicouche pendant les étapes de filtration ont été expliqués par l’inclusion de formulations appropriées pour le coefficient de filtration. Des simulations bidimensionnelles axisymétriques en régime transitoire ont été réalisées. L'approche CFD-DBF a été comparée aux résultats et observations expérimentales de Narayan et al. 1997 (Ind Eng. Chem. Res., 36, 4620) dans leur étude du kérosène pollué avec du noir de carbone traversant le lit fixe. La confrontation des simulations et les résultats expérimentaux permet de déclarer que l’approche CFD est un outil prédictif utile pour la description quantitative des lits fixes quand ils subissent un processus de colmatage. Des recommandations sont proposées afin d’améliorer la modélisation de la capture de particules particulièrement à de basses valeurs de nombres de Reynolds.

CFD Modeling and Simulation of Clogging in Packed Beds with non-Aqueous Media

(by Arturo Ortiz-Arroyo, Faïçal Larachi, Bernard P.A. Grandjean and Shantanu Roy)

[A paper published in ***AIChE J***. (2002). Vol 48, No. **8**, 1596-1609]

Abstract

When liquids containing low concentrations of *fine* solid impurities are treated in packed-bed reactors, clogging develops and starts hampering the flow severely. Instances where this phenomenon, called *deep-bed filtration*, constitutes serious concerns include hydrotreating or hydrocracking of bituminous sands in packed bed reactors, in which *non-filterable* fines, e.g., native clay or incipient coke, are the cause of reactor dysfunction by clogging. In this work, a detailed *k*-fluid Eulerian two-dimensional transient computational fluid dynamic (CFD) model has been formulated for the description of the space-time evolution of the clogging patterns developing in deep bed filtration (DBF) of fines'-containing non-aqueous liquids. A local formulation of the macroscopic logarithmic filtration law has been proposed, as well as a geometrical model for the effective specific surface area for momentum exchange. Both mono-layer and multiple-layer deposition mechanisms were accounted for by including the appropriate filter coefficient formulations.

Transient, 2-D axisymmetrical simulations were performed and the approach was benchmarked using the experimental results and observations of Narayan et al. 1997 (Ind. Eng. Chem. Res., 36, 4620) in their study of the carbon-black contaminated kerosene flow through packed beds. Comparing the simulations and experimental results allowed to state that CFD is a useful tool for the quantitative description of packed beds' clogging. Recommendations were put forth for improvements in modeling the fines deposition needed especially at low Re numbers.

Keywords packed bed, clogging, single-phase flow, fines, specific deposit, hydrodynamics, pressure drop, computational fluid dynamics

2.1 Introduction

Trickle bed reactors (TBR), which are catalytic fixed beds contacted by cocurrent downward gas-liquid flows, host a variety of gas-liquid-solid catalytic reactions especially in the petroleum and petrochemical industries. The economic impact of how well these reactors operate is considerable, since in the petroleum sector alone the annual processing capacity for various hydrotreatments (e.g., desulfurization, hydrocracking, metals removal, denitrification, etc.) exceeds billions of metric tons (Trambouze, 1991; Al-Dahhan et al. 1997; Duduković et al. 1999). With the permanent market shift towards increasing demand for light oil products (naphtha, middle distillates, gas oil), and the decreasing needs for heavy cuts, it is forecast that the refiners will keep improving their "bottom-of-the-barrel" processing units for upgrading heavy oil and residual feedstocks (Trambouze, 1993; Meyers, 1996). In addition, to comply with the EPA/EU low sulfur emission policy by the 2005 deadline, considerable pressure is put on the oil refining industries to produce diesel with low sulfur content (Marcandelli et al. 2000).

When liquids containing low concentrations of *fine* solid impurities are treated in packed beds, clogging develops so that ultimately the flow becomes severely hampered. A classical practical example arises in the area of deep bed filtration (DBF) of hydrosols where wastewater is treated by trapping solid biological materials to yield purified water. A less common area where this phenomenon represents a serious concern is in hydro-treating and hydro-cracking of resids where oil-borne *non-filterable* fines, such as native clay or incipient coke, are incriminated in the drop of catalytic reaction performances, and in the triggering of reactor hydrodynamic instabilities. The fines in such *non-aqueous* media can be of different origins. They may naturally occur in the liquid feed; a good example is the clay-containing Athabasca oil sands bitumen (Chan et al. 1994; Narayan et al. 1997). They may also be produced *in situ* in the form of coke (Wang et al. 1999; 2001) such as in the reduced-crude hydrodesulfurization process (Meyers, 1996) as a result of the decomposition and condensation of heavy asphaltic compounds. Other possibilities include the presence of iron sulfides produced by corrosion reactions in upstream equipment (Koyama et al. 1995). In the case of bitumen, the particles are usually small (< 20 μm) and cannot be retained in the upstream filtration trains. They subsequently enter the catalytic reactor and get progressively deposited upon the packing that makes up the reactor bed. Current industry response is to leave the bed collecting fines until the pressure drop climbs to a critical value forcing reactor shutdown (Gray, 2001). Thence, the reactor is emptied and reloaded afresh with pristine catalyst. Since in chemical terms, the catalyst is still highly active, such a drastic remedy causes considerable profit loss of the process. An alternative riposte consists in using catalyst pellets having special surface design for providing the necessary catalytic activity along with the suitable geometry to cope with the adhesion of unfilterable fines. For the time being, such geometry profiling is more an art science. The CDS-NP macaroni catalyst series of UOP RCD Unionfining process is a good example of that art (Meyers, 1996). Unfortunately, such solutions remain palliative in nature in the sense that they cannot get rid completely of bed clogging.

New fundamental knowledge is required to tackle the complex hydrodynamics and surface phenomena involved in the clogging with fines of packed-bed reactors typical of the oil industry. Indeed, there is a lack of descriptive and quantitative models which can be used for planning strategies for minimizing the problem of clogging in these reactors. This contribution is offered as a step in that direction.

In this work, a Computational Fluid Dynamics (CFD) based approach is developed for describing the deposition of fines in packed beds. Our endeavor at calculating two-dimensional axisymmetrical unsteady-state filtration concentrates in formulating the appropriate drag closures and the effective specific surface area model. For the time being, the proposed CFD framework is intended to provide a qualitative/quantitative assessment of the impact of fines build up during *single-phase* flow hydrodynamics. Such impact is measured in terms of pressure drop as a function of specific deposit relationships, as well as in terms of the clogging patterns developing throughout the porous medium. The approach is benchmarked using the experiments and observations of Narayan et al. (1997), who studied the macroscopic dynamics of kerosene/carbon black fine/glass bead bed flows. The set of mass and momentum conservation PDE equations is solved using the CFDLIB code (Kashiwa et al. 1994).

Our approach rests on formulating the problem in the following manner:

- ensemble-averaged continuity equations (mass conservation) for both fluid and packed bed;
- ensemble-averaged momentum conservation equations for the fluid phase;
- ensemble-averaged species balance equation for the fines;
- closure equations needed for the filtration rate and the momentum exchange term,
- a phenomenological description of fines capture,
- a model for the effective specific surface area,
- a bed voidage distribution model.

2.2 Experimental data used to validate the bed clogging CFD approach.

Validation of the model for the fines capture, the clogging of bed, and the build-up in pressure gradient is based on the experimental work of Narayan et al. (1997). Ambient clogging tests (room temperature and atmospheric pressure) were run in a one inch-I.D. one foot-high packed tube. A non-aqueous liquid, i.e., kerosene, seeded with various concentrations of 8-μm carbon black mimicking-fines flows upwards across a porous layer of randomly dumped one-mm glass beads (henceforth referred to as the collectors), see Table 2.1 for the other experimental conditions.

It was found in the experiments that the liquid superficial velocity was a key factor in controlling the amount of deposition as well as the morphology of the deposits of fines. The lower the liquid throughputs, the higher the collection rates of fines, and correspondingly, the larger the rise in pressure drops.

Visual inspection of the evolving morphology of the aggregates anchored to the collectors is indicative of complex capture mechanisms. Mainly driven by fine-fine interceptions, scattered and loose flocks (or cotton-like clusters) form at low liquid velocities. Especially at lower liquid feed rates, the fines preferentially deposit adjacent to the contact points between collectors, presumably because these are sites of static hold-up of liquid with lower rates of fluid renewal. At high liquid feed rates, collector-fine (and very likely non-Brownian) interactions occur, presumably through fluid drag, gravity-buoyancy and London-van der Waals forces, to yield disparate scattered thin patches of fine deposits over the collector outer surface.

The objective of this work is to present a flow simulation of the liquid/fines/porous medium system in the laboratory conditions of Narayan et al. (1997) and to compare the computational results with experimental observations presented in terms of pressure drop rise as a function of volume-averaged bed specific deposit relationships. This effort highlights the possibilities as well as the limitations of the multiphase flow simulations using CFD of the flows relevant to the petroleum refining area involving filtration mechanisms. It is hoped that this will arouse interest and new ideas for future improvements to the theory and the computational approach of DBF.

2.3 Governing Equations for the Fluid Transport in Porous Medium

An Euler-Euler two-fluid, two-dimensional, unsteady-state CFD model is formulated to describe the space-time evolution of clogging by fines and the resulting build-up of pressure drop in deep bed filtration as a function of the average specific deposit. The application problems targeted are typical of the petroleum refining catalytic processes. Specifically, the packing material and the fines dealt with here fall within the mm and the 10 μm ranges, respectively, with fines' loadings well below 0.2 ‰ v/v.

To conduct the multiphase flow simulations in DBF, use is made of the Los Alamos CFDLIB multiphase flow simulation library (Padial et al. 2000; Kashiwa and Rauenzahn, 1994). The ensemble-averaged Euler *k*-fluid multi-material formalism is used to integrate over finite control volumes (or grid cells) representing the computational grid, the time-dependent *phasic* conservation equations. For details about the CFDLIB numerical schemes, several references from the Los Alamos group can be consulted (Padial et al. 2000; Brackbill et al. 1997; Kashiwa and Rauenzahn, 1994; Kashiwa et al. 1994).

Here, the non-aqueous liquid/fine/porous medium multiphase system representing the DBF problem is treated as a system of two interpenetrating continuum phases: i) a *dilute* fluid phase consisting of the liquid embracing fines present at yet tiny volume fractions in the incoming stream, ii) and a pseudo-continuous solid phase made up of the packing particles (called "collectors", for the purposes of this work) of the porous bed along with the fines being attached to their surface due to capture. Both phases within each finite control volume of the computational domain are assumed to be having complementary ensemble-averaged volume fractions which, due to clogging by fines, evolve in time. To ensure resolution and convergence the grid cells should be specified of such a size to be sufficiently small in comparison of the dimensions of the DBF-containing vessel in order to assume constancy at the cell level of volume fractions, velocity, pressure, or any advected scalar or vector (Kashiwa et al. 1994; Sokolichin and Eigenberger, 1994).

To perform the flow field simulations using CFD, the packed bed was discretized in a r-z framework into cells by assigning at every grid point $\underline{\mathbf{a}}$ in the computational domain, a cell volume $v(\underline{\mathbf{a}})$ and an initial local porosity $\varepsilon_0(\underline{\mathbf{a}})$.

The following assumptions are inherent in the formulation presented in this paper:

- the properties of the pseudo-homogeneous fluid, i.e., liquid+fines, in short henceforth referred to as *fluid*, are equal to those of the embracing liquid (inlet fines volume fraction ≤ 0.1 ‰),

- the density of the packing is not affected by the collected mass of fines, i.e. dilute solid phase,
- the single homogeneous fluid is assumed to be isothermal and incompressible;
- turbulent transport neglected, i.e., Reynolds stress negligible;
- net sink for fluid momentum due to fines capture on the collector neglected;
- no re-entrainment of deposited fines occur;
- bed clogging by *sieving effect* (Tien and Payatakes, 1979) and *blocking mode* (Choo and Tien, 1995a) does not occur;
- the local fluid velocity in every grid cell is below the critical velocity that impedes deposition due to a large drag force acting on the impinging fines. For hydrosols, this critical velocity lies within the 1 – 20 mm/s range (Rege and Fogler, 1988; Mackie et al. 1987); (this assumption is checked *post facto*);
- the coupling between the fluid and solid phases is monitored via the *fines* filter equation (Eq. 2.8) and the interaction drag or momentum exchange force term (Eq. 2.20).

The conservation equations of mass, momentum and species (i.e., the fines) are provided in the form of the Euler-Euler formulation. These equations consist of the continuity and the Navier-Stokes equations for the fluid phase, a continuity equation for the solid *stationary* phase and a species balance equation for the fines being displaced from the fluid phase to the solid phase.

Continuity equation for the fluid phase

$$\frac{\partial}{\partial t}\varepsilon\rho_\ell + \nabla \bullet \varepsilon\rho_\ell \underline{\mathbf{u}}_\ell + \rho_f N = 0 \qquad (2.1)$$

Continuity equation for the solid phase

$$\frac{\partial}{\partial t}(1-\varepsilon)\rho_s = \rho_f N \qquad (2.2)$$

Species balance equation for the fines

$$\frac{\partial}{\partial t}\varepsilon c + \nabla \bullet \varepsilon c \underline{\mathbf{u}}_{\ell} + N = 0 \tag{2.3}$$

Momentum balance equation for the fluid phase

$$\frac{\partial}{\partial t}\varepsilon \rho_{\ell} \underline{\mathbf{u}}_{\ell} + \nabla \bullet \varepsilon \rho_{\ell} \underline{\mathbf{u}}_{\ell} \otimes \underline{\mathbf{u}}_{\ell} = -\varepsilon \underline{\nabla} P + \varepsilon \rho_{\ell} \underline{\mathbf{g}} + \nabla \bullet \mu_{\ell} \varepsilon \left(\nabla \underline{\mathbf{u}}_{\ell} + \left[\nabla \underline{\mathbf{u}}_{\ell} \right]^{T} \right) + \underline{\mathbf{F}}_{\ell s} \tag{2.4}$$

The solid (packing) phase transfers momentum with the fluid phase through the effective drag term. While in the fluid phase this results in modifying the velocity field, in the packing phase it results in shear stress and inter-particle compressive stress. The solids stress balance is not explicitly solved here, since the scope of our work focuses on the fluid phase and the way fines get deposited *on* the packing.

The fines are imposed in the influent stream as a fluid step-increase function after *suddenly* switching from the *steady-state* flow of clean or “fines-free” liquid flow through the immaculate porous medium. Solution of this initial state is obtained by solving the continuity and the momentum balance equations for the pure liquid case.

Continuity equation for the liquid phase

$$\nabla \bullet \varepsilon_{o} \rho_{\ell} \underline{\mathbf{u}}_{\ell}^{o} = 0 \tag{2.5}$$

Momentum balance equation for the liquid phase

$$\frac{\partial}{\partial t}\varepsilon_{o} \rho_{\ell} \underline{\mathbf{u}}_{\ell}^{o} + \nabla \bullet \varepsilon_{o} \rho_{\ell} \underline{\mathbf{u}}_{\ell}^{o} \otimes \underline{\mathbf{u}}_{\ell}^{o} = -\varepsilon_{o} \underline{\nabla} P + \varepsilon_{o} \rho_{\ell} \underline{\mathbf{g}} + \nabla \bullet \mu_{\ell} \varepsilon \left(\nabla \underline{\mathbf{u}}_{\ell}^{o} + \left[\nabla \underline{\mathbf{u}}_{\ell}^{o} \right]^{T} \right) + \underline{\mathbf{F}}_{\ell s}^{o} \tag{2.6}$$

The problem depicted by the above five *scalar* conservation equations (Eqs. 2.1-2.4) is 2-D + t. It contains five natural unknowns, i.e., ε, c, P, and the $\underline{\mathbf{u}}_{\ell}$ axial and radial scalar projections. It further contains two dependent unknowns, the filtration rate and the momentum exchange term, which require additional closure formulations. Procurement of expressions of the dependent unknowns as a function of some of the five natural unknowns permits to have a closed form of the CFD model yielding a solution specific to the present hydrodynamic flow problem.

2.4 Closure Models

Ad hoc closure models are required for the filtration rate, N, and the momentum exchange term in the conservation equations Eqs.2.1-2.6.

2.4.1 Filtration rate

The filtration (or deposition) rate determines the degree of collection of fines. On a volume basis, it measures the volume of fines collected per unit grid cell volume and unit time. The filtration rate is related to the specific deposit, σ, which represents the volume of fines deposited per unit grid cell volume. Both N and σ are *local* and time-dependent. Hence, N is assumed to depend on the local number of fines present in the fluid, i.e., the fines concentration c, and the local state of the porous medium that is characterized by the specific deposit (Tien, 1989):

$$\mathrm{N}(\sigma, \mathrm{c}, \mathrm{t}, \underline{\mathbf{a}}) = \frac{\partial \sigma}{\partial \mathrm{t}} \tag{2.7}$$

For a microscopic description required in the CFD approach, it is useful to recast the *unidirectional* macroscopic phenomenological formalism that ties the fines concentration and the fluid velocity to the filtration rate. This is achieved by assuming that at the grid cell level, the relationship is symbolically preserved so that the filtration rate is proportional to the local concentration and interstitial fluid velocity. In the absence of more sophisticated "local" models, we tailor the well-trodden and popular logarithmic law of Iwasaki (1937) to express such a dependence of the deposition rate:

$$\mathrm{N} = \lambda \mathrm{c} \left\| \underline{\mathbf{u}}_{\ell} \right\| \tag{2.8}$$

where λ is the filter coefficient which can be thought of as the probability for a fine to be captured as it travels a unit distance through the bed (Tien, 1989). The form of the filter coefficient is dictated by the nature of the capture phenomena in play, and by the amount of capture as bed clogging proceeds.

The fines deposition hence evolves through two stages (Choo and Tien, 1995a):

- The first stage describes the initial, almost clean filter bed, having an initial filter coefficient, λ_o, and a specific deposit $\sigma \approx 0$ (Fig. 2.1a). During this stage, the fines adhere individually as a *mono-layer* on the collector surface through fine-collector interactions. In the vicinity of the collector, their capture is an outcome of a force balance which determines their motion. In the present analysis, Brownian diffusion ($d_f > 1$ μm), electrostatic and double-layer forces are neglected. Furthermore, as is typical in hydrosols filtration at tiny feed rates, the inertial forces of the fines are marginal. Hence, the forces likely in play are the fluid drag and the London van der Waals surface-interactive force. As long as the mono-layer keeps developing, the specific deposit obeys the condition:

$$\sigma \leq \sigma_{crit.} \tag{2.9}$$

which is derived assuming a layer thickness equal to that of one fine diameter. The critical specific deposit, $\sigma_{crit.}$, corresponds to the amount of fines required for completing a mono-layer having a coating porosity ε_d. Its full expression will be given later in Eq. 2.37.

Under these circumstances, the trajectory simulations of Rajagopalan and Tien (1976) yield the following numerical correlation for the initial filter coefficient:

$$\lambda(\underline{\mathbf{a}}) = \lambda_o(\underline{\mathbf{a}}) = \frac{9}{4d_c} A_s \left(1 - \varepsilon_o(\underline{\mathbf{a}})\right) N_R^2 \left[\frac{2}{3} N_L^{1/8} N_R^{-1/8} + \frac{9}{4000} N_G^{6/5} N_R^{-12/5}\right] \tag{2.10}$$

where A_s is the Happel parameter defined as:

$$A_s = \frac{2\left(1 - p^5\right)}{w} \tag{2.11}$$

$$p = \sqrt[3]{1 - \varepsilon_o(\underline{\mathbf{a}})} \tag{2.12}$$

$$w = 2 - 3p + 3p^5 - 2p^6 \tag{2.13}$$

The dimensionless groups representing the relative importance of gravitational and viscous forces, N_G, the relative importance of the London – van der Waals forces and the viscous forces, N_L, and the interception parameter, N_R, are defined respectively, as:

$$N_G(t, \underline{\mathbf{a}}) = \frac{(\rho_f - \rho) d_f^2 g}{18 \pi \mu \left\| \underline{\mathbf{u}}_\ell \right\|} \tag{2.14}$$

$$N_L(t, \underline{\mathbf{a}}) = \frac{4H}{9 \pi \mu d_f^2 \left\| \underline{\mathbf{u}}_\ell \right\|} \tag{2.15}$$

$$N_R = \frac{d_f}{d_{co}} \tag{2.16}$$

- During the second stage, no room is left for adhesion of fines through the fine-collector interactions and the condition given by Eq.2.9 no longer holds. Driven now by fine-fine interactions, an interception mechanism establishes, and fines start piling up as a multi-layer deposit (Fig. 2.1b). The fines already deposited on the collectors themselves become secondary collectors: the capture can be viewed as an auto-catalytic process in which the filtration rate gets accelerated as more and more fines are trapped. The filter coefficient no longer remains constant with time and an expression representing its time-evolution during the second stage is necessary. Several empirical correlations are available in literature, wherein the filter coefficients during ripening have to be fitted to the experimental filtration rate data (O'Melia and Ali, 1978; Chiang and Tien, 1985; Vigneswaran and Tien, 1987; Mackie et al. 1987). For the sake of preserving to the present approach a predictive capability, we rather preferred to use the numerical correlation derived from trajectory analyses by Choo and Tien (1995a) as a function of the interception number, the specific deposit, and the initial filter coefficient:

$$\begin{aligned}\frac{\lambda(t,\underline{a})}{\lambda_o(\underline{a})} &= (1-Y)\left[1+\frac{0.6794}{1-\varepsilon_o(\underline{a})}\left(\frac{1}{N_R}-0.921\right)\left(\frac{\sigma(t,\underline{a})}{1-\varepsilon_d}\right)+\frac{0.1731}{(1-\varepsilon_o(\underline{a}))^2}\left(\frac{1}{N_R^2}+\frac{3}{N_R}-117.1\right)\left(\frac{\sigma(t,\underline{a})}{1-\varepsilon_d}\right)^2\right] \\ &\quad + Y\left[1+9.61(1-\varepsilon_o(\underline{a}))^{2/3}\left(\frac{\sigma(t,\underline{a})}{1-\varepsilon_d}\right)\right]\end{aligned} \qquad (2.17)$$

$$\text{where } Y = \frac{0.598 k_d^{-0.8}\left(1-\varepsilon_o(\underline{\mathbf{a}})\right)^{-2}\left(1+\frac{0.0128}{N_R}\right)\left(\frac{\sigma(t,\underline{\mathbf{a}})}{5(1-\varepsilon_d)}\right)^{1.63+\frac{5.5\times10^{-4}}{N_R}}}{1+0.598 k_d^{-0.8}\left(1-\varepsilon_o(\underline{\mathbf{a}})\right)^{-2}\left(1+\frac{0.0128}{N_R}\right)\left(\frac{\sigma(t,\underline{\mathbf{a}})}{5(1-\varepsilon_d)}\right)^{1.63+\frac{5.5\times10^{-4}}{N_R}}} \qquad (2.18)$$

In Eqs.2.17, 2.18, the deposit permeability, k_d, was estimated using a Kozeny-Carman like expression (Dullien, 1992) and the porosity of the deposit, ε_d, was assigned a value of ca. 0.8 (Tien, 1989).

2.4.2 Momentum exchange

In any given point $\underline{\mathbf{a}}$ of the computational domain, the momentum exchange vector can be formulated as the product of the volume fractions of the two k phases, the momentum exchange rate coefficient, $X_{\ell s}$, and the local relative velocity between the k phases (Kashiwa et al. 1994):

$$\underline{\mathbf{F}}_{\ell s} = -\varepsilon(1-\varepsilon)X_{\ell s}\underline{\mathbf{u}}_{\ell} \qquad (2.19)$$

in which $X_{\ell s}$ takes the general *creeping flow* form as a function of the local instantaneous values of the porosity and of the effective specific surface area, $\bar{a}_{\beta\gamma}$ (to be discussed later in § 2.4.3.):

$$X_{\ell s}(t,\underline{\mathbf{a}}) = h_K \, \bar{a}_{\beta\gamma}^{2}(t,\underline{\mathbf{a}}) \frac{(1-\varepsilon(t,\underline{\mathbf{a}}))}{\varepsilon^3(t,\underline{\mathbf{a}})} \mu_\ell \tag{2.20}$$

In clean bed simulations, $X_{\ell s}$ takes the following simplified form:

$$X_{\ell s}(\underline{\mathbf{a}}) = \frac{36 h_K}{d_{co}^2} \frac{(1-\varepsilon_o(\underline{\mathbf{a}}))}{\varepsilon_o^3(\underline{\mathbf{a}})} \mu_\ell \tag{2.21}$$

In combination with Darcy's law, $X_{\ell s}$ can easily be interpreted using the permeability concept:

$$X_{\ell s}(t,\underline{\mathbf{a}}) = \frac{\mu_\ell}{B(t,\underline{\mathbf{a}})(1-\varepsilon(t,\underline{\mathbf{a}}))} \tag{2.22}$$

with the local permeability being defined as:

$$B = \frac{\varepsilon^3(t,\underline{\mathbf{a}})}{h_K \, \bar{a}_{\beta\gamma}^{2}(t,\underline{\mathbf{a}})(1-\varepsilon(t,\underline{\mathbf{a}}))^2} \tag{2.23}$$

Note that the Blake-Kozeny-Carman constant, h_K, in Eqs. 2.20, 2.21 and 2.23 is assigned a mean value equal 5 as a consensus value in DBF (O'Melia and Ali, 1978; Stephen and Chase, 2000).

As suggested from Eq. 2.23, the drop in local permeability with time is caused by two factors: a drop in local porosity as the specific deposit increases, and at the same time, an increase in local effective specific surface area as a result of the increasing number of fines being attached to the collectors (Herzig et al. 1970). A trade-off between the "bulk" effect due to porosity deflation, and the "areal" effect due to the enhancement of the liquid-solid interface for drag by the fines will be assessed later.

Neglect of the previous areal effect would yield the following simplified form of the momentum exchange coefficient:

$$X_{\ell s}(t,\underline{\mathbf{a}}) = \frac{36 h_K}{d_c^2(t,\underline{\mathbf{a}})} \frac{(1-\varepsilon(t,\underline{\mathbf{a}}))}{\varepsilon^3(t,\underline{\mathbf{a}})} \mu_\ell \tag{2.24}$$

As will be seen, such formulation fails to forecast the rise of pressure drop in clogged beds because the impact of the specific surface area is essentially overlooked. As drag models based on porosity changes are expected not to produce satisfactory predictions of the pressure drop build-up (O'Melia and Ali, 1978), the impact of the rise in effective specific surface area is included. For that purpose, an accurate model of the effective specific surface area must be developed and included in the momentum exchange coefficient given by Eq. 2.20.

2.4.3 Effective specific surface area model for momentum transfer

With the progress of bed clogging, the solid-fluid surface area of the *filter bed* is altered by two opposing phenomena (Stephan and Chase, 2000). The capture of fines by the collector causes an increase in surface area by an amount equivalent to the cross-section fraction, γ, being actually exposed by the *anchored* fines to the streamline flow (Fig. 2.2a). *Ipso facto*, a fraction of the *collector* area located immediately beneath the anchored fine no longer contributes to the subsequent collection events. This last phenomenon, known as the "shadow effect" (Tien and Payatakes, 1979), results from the spontaneous hindrance occasioned by the tethered fines, and also from the alteration by the fine of the local flow field; both impeding the access to the collector area, A_Δ, behind the fine for further interceptions (Fig. 2.2a).

Similarly, the ability the collector has to capture the incoming fines largely depends on the location of impact on the collector periphery. While frontal locations, especially on the upstream collector pole, are likely to be active in the capture process, points such as those located on the collector downstream pole are more or less passive. To handle this angular feature, it can be stated that the collector offers a cross-section fraction, β, for fines capture (Fig. 2.2a).

The cross-section fractions β and γ are thus measures of the peripheral areas effectively involved in interception. They account for the surface of the target reachable by the incoming fines and fluid for momentum and mass transfers. For instance a cross-section fraction of 0.5 means that interception fully exploits the frontal hemispheric area of the target (Stephen and Chase, 2000).

Consequently, in terms of solid-fluid drag activity, not all the total solid-fluid *geometrical* surface area participates in the momentum transfer during the subsequent collisional interceptions occurring at the periphery of the collecting assemblage, i.e., collector-deposited fines. Due to peculiarities in the geometrical configuration of the collector-deposited fines porous medium, e.g., throats, cul-de-sacs, rough relief, creeks, etc., only a fraction of the total surface area, henceforth referred to as the *effective specific surface area*, $\bar{a}_{\beta\gamma}$, is involved in the interception and also in the momentum exchange coefficient of the drag term appearing in the momentum balance equation (Eqs.2.4, 2.20).

At every point $\underline{\mathbf{a}}$ of the computational domain, the *instantaneous* effective specific surface area, expressed per unit *total solid volume in grid cell*, can be summarized in the following compact relationship:

$$\bar{a}_{\beta\gamma}(t,\underline{\mathbf{a}}) = \frac{\overbrace{\tilde{N}_c(\underline{\mathbf{a}})\beta(t,\underline{\mathbf{a}})\pi d_c^2(t,\underline{\mathbf{a}})}^{\text{Useful area of collectors}} + \overbrace{\tilde{N}_c(\underline{\mathbf{a}})\partial\tilde{N}_f(t,\underline{\mathbf{a}})\left(\gamma\pi d_f^2 - A_\Delta(t,\underline{\mathbf{a}})\right)}^{\text{Peripheral area due to captured fines}}}{\tilde{N}_c(\underline{\mathbf{a}})\frac{\pi}{6}d_{co}^3 + \tilde{N}_f(t,\underline{\mathbf{a}})\frac{\pi}{6(1-\varepsilon_d)}d_f^3} \tag{2.25}$$

in which $\tilde{N}_c(\underline{\mathbf{a}})$ and $\tilde{N}_f(t,\underline{\mathbf{a}})$ are, respectively, the number of collectors and the number of captured fines in cell volume $v(\underline{\mathbf{a}})$; $\partial\tilde{N}_f(t,\underline{\mathbf{a}})$ represents how many fines, per collector, culminate at the periphery of the collecting assemblage at time t; d_{co} and d_c are the diameters of, respectively, the initial *clean* collector and the *dirty* collector in duty at time t; and ε_d is the porosity of the fines deposit usually assigned a value of *ca.* 0.8 (Tien, 1989).

The number of collectors in any given cell located at $\underline{\mathbf{a}}$ can be obtained straightforwardly as:

$$\tilde{N}_c(\underline{\mathbf{a}}) = \frac{6v(\underline{\mathbf{a}})}{\pi d_{co}^3}\left(1-\varepsilon_o(\underline{\mathbf{a}})\right) \tag{2.26}$$

Analogously, the number of fines deposited within the time period [0 – t] in cell volume $v(\underline{\mathbf{a}})$ is computed from the variation of the solid volume fraction caused by deposition:

$$\tilde{N}_f(t,\underline{\mathbf{a}}) = \frac{6v(\underline{\mathbf{a}})}{\pi d_f^3}\left(\varepsilon_o(\underline{\mathbf{a}})-\varepsilon(t,\underline{\mathbf{a}})\right)\left(1-\varepsilon_d\right) \tag{2.27}$$

Or equivalently, in terms of the local value of the specific deposit:

$$\sigma(t,\underline{\mathbf{a}}) = \left(\varepsilon_o(\underline{\mathbf{a}})-\varepsilon(t,\underline{\mathbf{a}})\right)\left(1-\varepsilon_d\right) \tag{2.28}$$

As time evolves, a deposit layer develops on top of the collector. Accordingly, the collector diameter swells and the collector center drifts upwards from O to O' (Fig. 2.2b). Usually, the *crescent-like* deposited layer is at its thickest at the front stagnant point of the collector (Choo and Tien, 1995b). To account for the non-uniform circumferential growth of the deposit, the increase in the collector diameter in every cell of the flow field is calculated as a function of the specific deposit assuming sphere-in-cell model configurations such as that of Choo and Tien (1995b) illustrated in Fig. 2.2b:

$$d_c(t,\underline{\mathbf{a}}) = d_{co}\sqrt[3]{1+\frac{\sigma(t,\underline{\mathbf{a}})}{(1-\varepsilon_d)(1-\varepsilon_o(\underline{\mathbf{a}}))}} \tag{2.29}$$

The collector area loss, A_Δ, occasioned by the shadow effect per attached fine is estimated from the shadow left by an equilateral triangle in which the fine is inscribed as shown in Fig. 2.3:

$$A_\Delta(t,\underline{\mathbf{a}}) = \frac{\pi d_c^2(t,\underline{\mathbf{a}})}{2}\left[-1+\sqrt{1+\frac{3d_f^2}{d_c^2(t,\underline{\mathbf{a}})}}\right]\cos\frac{\sqrt{3}d_f}{d_c(t,\underline{\mathbf{a}})} \tag{2.30}$$

As argued earlier, the peripheral fines culminating over the collecting assemblage populate the area corresponding to the cross-section fraction β. The number of peripheral fines becomes thus (Vigneswaran and Tulachan, 1988):

$$\partial\tilde{N}_f(t,\underline{\mathbf{a}}) = 4\beta(t,\underline{\mathbf{a}})(1-\varepsilon_d)\left(\frac{d_c(t,\underline{\mathbf{a}})}{d_f}\right)^2 \tag{2.31}$$

For the effective specific surface area given by Eq.2.25 to be fully computable, it is necessary now to estimate the cross-section parameters β and γ.

When $\sigma \approx \sigma_{crit.}$, (Eq.2.9, Fig. 2.1a), it is safe to assume that an upper bound of the cross-section fraction corresponds to the hemispheric frontal area of the anchored fine. This situation holds during the first stage on the initial almost clean filter bed. Thus, we have approximately

$$\gamma \approx 0.5 \tag{2.32}$$

During the subsequent stage when multiple layers of fines form on top of the collector, the impinging fines encounter a roughened relief. Hence, interception, rather than being on a one-to-one basis, most likely involves boundaries of several fines at a time (Fig. 2.4). It appears at this stage that a rigorous geometrical model for fines capture through fine-fine interactions is an overkill, given the other uncertainties in the formulation that may mask any improved geometric model. As also pointed out by Stephen and Chase (2000), a γ value as given by Eq. 2.32 proves inadequate. As suggested by Fig. 2.4, the cross-section parameter γ is expected to change with the evolution of the specific deposit. Instead and for simplification purposes, the model is allowed to search for a single *overall* γ value within the range [0.5 – 1] until an acceptable match between measured and predicted pressure drops across the bed versus the current value of specific deposit is achieved for every Reynolds number value. As the CFD simulations are time consuming, we did not attempt to locate precisely the optimum value of γ. Hence, when the specific deposit exceeds the critical specific deposit $\sigma_{crit.}$, that is Eq. 2.9 is not satisfied, the recommended value for the conditions of this work fall within the range:

$$\gamma \approx 0.6 \quad \text{to} \quad 0.75 \tag{2.33}$$

On the other hand, the cross-section parameter for the collector, β, is evaluated assuming that the growth of the fines layer around the collector can be described by the aforementioned sphere-in-cell model sketched in Fig. 2.2b. Taken at a snapshot for a given azimuthal coordinate θ, the distance between the center O of the clean collector and a peripheral point A on the fines mantle is approximated by (Choo and Tien, 1995b):

$$\delta \approx \frac{d_{co}}{2}\sqrt{1+2h_o}\left[1+\frac{h_o\cos\theta}{\sqrt{1+2h_o}}+\frac{h_o^2\cos\theta}{2(1+2h_o)}\right] \tag{2.34}$$

where $h_o = \dfrac{d_c(t)}{d_{co}} - 1$

Physically, the *downstream* edge of the deposit layer is delineated by a ring accommodating a string of fines of diameter d_f girdling the collector (two filled black circles, Fig. 2.2b). In a 2-D view (Fig. 2.2b), the critical point of deposition ($\delta_{crit.}$,$\theta_{crit.}$) is restricted by the sphere of lowest volume in which a fine can fit, i.e., $\delta_{crit.} = d_{co}/2 + d_f$. Hence, it is postulated that the collector area beneath the *latitude* of this critical point is hidden and unavailable for interception, whereas the area upstream allows for capture and growth of the fines layer. As time evolves, the latitude of the ring slides downwards due to the thickening of the deposit. Consequently, the cross-section fraction is expected to increase accordingly.

Knowing the value of σ at $\underline{\mathbf{a}}$ and instant t yields from Eq. 2.29 the diameter $d_c(t)$. By equating δ with $\delta_{crit.}$ in Eq.2.34 one obtains through an iterative procedure the angle $\theta_{crit.}$ of the critical point of deposition. Geometrical arguments yield the area of the hidden pole of the collector:

$$A_H \approx \frac{\pi}{2} d_{co}^2 \left(1 + \cos\theta_{crit.}\right) \tag{2.35}$$

Finally, the cross-section fraction β is obtained from the ratio of the hidden pole area to that of the collector area with the diameter d_c calculated by means of Eq. 2.29:

$$\beta = 1 - \frac{A_H}{\pi d_c^2(t)} \tag{2.36}$$

Owing to the angular dependence of the fines coating thickness illustrated above, the critical specific deposit must be evaluated after resting the passive area of the downstream collector's pole. Hence instead of using the smooth-layer coating relationship of Tien and Payatakes (1979), the following relationship, derived from simple geometrical arguments, must be used for ensuring the switch from the filter coefficient λ_o Eq. 2.10 to the filter coefficient λ Eq. 2.17:

$$\sigma_{crit.} \approx \frac{3}{2}\frac{d_f}{d_{co}}\left(1 - \varepsilon_o(\underline{a})\right)\left(1 - \varepsilon_d\right)\left(1 - \cos\theta_{crit.}\right)^2\left(2 + \cos\theta_{crit.}\right) \tag{2.37}$$

2.5 Numerical simulation of Narayan et al. (1997) filtration experiments

2.5.1 Voidage model of the clean packed bed

The high aspect ratios $d_R/d_c \approx 25$ and $H/d_R \approx 12$ yielding in our case *ca.* 175,000 particles in bed make computerization of the porous medium geometry impossible. The k-fluid Euler approaches are suitable to lift such a limitation by viewing voxels in the computational domain as made up of *probabilistic volume fraction* contributions arising from each phase occupying the voxel but without requiring detailed knowledge of local geometry. Note that in this description (see for e.g. Drew, 1983; Drew and Passman, 1998), the identity of an individual particle is lost and each phase is treated as a pseudo-continuum in each cell and in the whole domain. The forces arising from the interactions between the phases (both "skin" and "form" drag) are modeled with appropriate closures, as discussed above, with the understanding that the conservation equations themselves (of the k-fluid model) are exact. The validity of the closures and their exactness is justified with arguments as those made above, and anyway have to satisfy the *post-facto* test in being able to explain the macroscopic experimental data.

A voidage field, or equivalently its complementary solid-filled counterpart, is thus generated in a 2-D axisymmetrical computational domain of communicating grid cells to represent the initial porosity of the clean packed bed state. The dimensions of the bed are summarized in Table 2.1.

Once the mesh size is decided, the local voidage per cell is obtained by means of a simple simulation program that assigns randomly porosity values by using a normal Gaussian probability density function (Jiang et al. 2001; Chen et al. 2001). A mean bed porosity of 0.37 is used, which is the value measured by Narayan et al. (1997) for their bed. Also, the allowed disparities in porosity varied within the range 0.346 – 0.395. The thus obtained voidage field is shown in Fig. 2.5 as a contour plot of solid volume fraction for a discretization using 2,768 cells.

2.5.2 Mesh, boundary and initial conditions

Due to the simple cylindrical bed geometry, a single-block computational mesh of a structured type is used in the CFDLIB finite volume solver with explicit temporal differencing (Brackbill et al. 1997). The Eulerian boundary conditions for the fluid (or liquid) are of four types: specified inflow, conserving outflow, centerline symmetry, and reflective-wall (or free-slip wall) condition.

The fluid (or liquid, clean bed simulation) is fed upwards through an already *imbibed* bed. At the inlet boundary, CFDLIB requires that the fluid velocity and the fines concentration be specified. To prevent slow convergence, the inflow *liquid* velocity profile is ramped from zero to its final value which is reached within ca. 10 *real-time* seconds. At the bed top, the outflow boundary condition is computed to ensure mass conservation of the fluid (or liquid). At the vessel vertical boundaries, a free-slip wall condition is imposed. This means that the velocity component or the flux of an advected scalar (fines concentration) normal to the wall is zero. Also, the wall tangential velocity component is approximated by that of the adjacent cell-centered cell.

Transient simulations of *clean* bed liquid flow are run until the flow field (pressure and velocity) reaches steady state. Under these circumstances, the conservation equations (Eqs.2.5, 2.6) are solved in the absence of fines in the liquid along with the momentum exchange coefficient calculated using the Blake-Kozeny-Carman drag equation Eq.2.21. Transient simulations with fines-containing liquid are then resumed by solving Eqs. 2.1-2.4. The clogging simulations correspond to sets of experiments reported by Narayan et al. (1997) for three kerosene Reynolds numbers: Re = 0.1, 0.5, and 1.

To ensure grid convergence, numerical simulations are performed on computational grids of up to 3000 cells. The finer grid was chosen to allow i) representative collectors-per-cell statistics, ii) realistic execution cpu time, and iii) converging results. The coarser grid was set once the mismatch between results from fine and coarse grids becomes significant. When the pressure drop versus specific deposit profiles at different grid resolutions yield mean absolute relative errors < 0.5% (and residuals' standard deviation < 0.3%), grid independence was assumed to be attained. Because the simulations are computationally intensive, the grid size is held to a minimum, and the smaller the Reynolds number the finer the grid. The dense character of the thus selected computational grids and the smallness of the time steps preclude the occurrence of problems associated with numerical diffusion. Simulations are carried out on a dual-processor Pentium III running at 1000 MHz each. Typical simulation time is about 3 CPU days for simulating clogging flows lasting up to 20 real-time hours at Re = 0.1 and 2768 grid cells.

2.5.3 Model simulation flow chart

With the above CFD model of DBF, the evolution of clogging in the packed bed can be simulated. Hence, detailed numerical output results can be obtained including the time-evolving fields of porosity, specific deposit, velocity, permeability, and pressure. Also, the instantaneous bed-scale or bulk pressure drop, defined as the difference between the inlet and outlet pressures divided by the bed height, can be calculated and plotted against the mean global specific deposit. Note that the mean global specific deposit is the volume averaged specific deposit over all the computational grid cells which is calculated as:

$$\langle \sigma(t) \rangle = \frac{\sum_{i}\sum_{j} \sigma_{ij}(t, \underline{\mathbf{a}}) v_{ij}(\underline{\mathbf{a}})}{\sum_{i}\sum_{j} v_{ij}(\underline{\mathbf{a}})} \tag{2.38}$$

2.6 Discussion & Concluding Remarks

To illustrate the qualitative and quantitative filtration features, the simulated results are presented in terms of contour plot snapshots of specific deposit, local permeability and local porosity for the kerosene Reynolds numbers of 0.1, 0.5 and 1. Likelihood of the simulated patterns is supported from comparing bulk simulated solutions with bulk experimental measurements of the pressure drop build up versus global specific deposit.

Filtration phenomena in porous media being a complex problem, non-invasive field probing of the transient phenomena accompanying fluid flow and fines deposition in bed is not trivial even by performing the most sophisticated laboratory sensing or imaging techniques. One of the advantages CFD simulations permit is the possibility to mimic these phenomena by solving the rigorous transport equations.

The axisymmetrical contour plot of the local specific deposit (Eq. 2.28) is illustrated in Figs. 2.6a-c for, respectively, Re = 0.1, 0.5, and 1.0. Three snapshots (I)–(III) are shown for each Re number value. The snapshot triplets (I), or (II) or (III) correspond to approximately constant mean global specific deposit in the bed (Eq.2.38), *ca.* 1.3, 2.7, and 4.6 mg fines/mL bed, respectively.

Coherent with the photographs of Narayan et al. (1997), the bed increasingly captures fines the lower the Reynolds number (or the liquid throughput). The peak specific deposits of 30 mg/mL occur at Re = 0.1 (Fig. 2.6a), which are up to a factor six larger than the peak specific deposits at Re = 0.5 or 1.0 (Fig. 2.6b,c). As time evolves, the *clogging front* progressively fills up the column. However, clogging is more confined in the entrance region at low Re numbers. Hence, the bed undergoes more inhomogeneous clogging the lower the Reynolds number yielding sharper contrasts in the specific deposits between the entrance and the exit regions. Moreover, longer clogging duration is required, as expected, to attain the same global specific deposit with increasing Re number.

The drop in local bed permeability for the same simulation conditions is illustrated in Figs. 2.7a-c. The contour plot snapshots are depicted using as a measure of divergence from the clean bed state the error function $100\times(B_o - B(t))/B(t)$. This function measures how much the instantaneous local permeability B (Eq.2.23) departs, during the course of clogging, from the permeability B_o of the immaculate bed. It is important to note that the lower scale value at 60% in Fig. 2.7 has been set for commodity to better illustrate the color contrast so that permeability changes between 0 and 60% are embedded in this lower limit.

The simulated permeability patterns are in qualitative agreement with those corresponding to specific deposit. At the lowest Reynolds value, the bed entrance portion, i.e., area of the highest collection *activity*, undergoes permeability drop off by almost one order of magnitude (red spot in Fig. 2.7a). There the permeability falls by 882% with respect to the clean bed local permeability, B_o. In the upper bed portions, deposition has less a hold and the clean bed permeability is preserved as bed outlet is approached, i.e., $B \rightarrow B_o$. However with the increase in DBF time or global specific deposit, the *contaminated* bed fraction swells up. As Re number is increased and for constant global specific deposit values, the reduction in permeability is distributed in a more homogeneous manner throughout the bed (Fig. 2.7b,c). This result is in agreement with Narayan et al. (1997) experimental observations who found that deposition was distributed more evenly throughout the bed. For the highest Re and the highest global specific deposit, bed local permeabilities decrease by a factor three or less.

It is very instructive to parallel the behavior in permeability with that exhibited in the porosity field for the same conditions. Hence, Figures. 2.8a-c depict snapshot contour plots of the local void volume fraction taken at the conditions of Figs 2.6 and 2.7. The plots are constructed using as a measure of departure from the initial local porosity, the error function $100\times(\varepsilon_o - \varepsilon(t))/\varepsilon_o$. This function was also evaluated at global scale, using the global specific deposit and the average bed porosity, see Table 2.2.

While local bed permeability may decline by up to an order of magnitude, the corresponding local porosity does not change by more than 6% (red spots in Fig. 2.8a). Reduction in local porosity is less pronounced at higher Re numbers. On a bed averaged scale, the decrease in the average bed porosity never exceeds 3.7% (Table 2.2) for the highest global specific deposits.

The maximum change in local permeability due to the bulk effect in Eq.2.23, i.e., via $\varepsilon^3/(1-\varepsilon)^2$, does not exceed 35% for the maximum increase by 6% in the local porosity (Figs. 2.8a-c). Consequently, the bulk effect alone is not able to explain why the permeability diminishes by up to 880% (Figs. 2.7a-c). It is therefore the areal effect contributed in Eq.2.23 by the effective specific surface area, i.e., via $\bar{a}_{\beta\gamma}$, that contributes for the majority of the changes undergone by permeability. This result is not surprising, in view of the experimental results from researchers like Herzig et al. (1970), O'Melia and Ali (1978), and Vigneswaran and Tulachan (1988) to propose macroscopic empirical drag models accounting for the fines build up. The present work corroborates such findings and stresses out their importance at a more local scale. The variable bringing about the most important changes in permeability is the effective specific surface area which required an accurate model such as the one proposed earlier (Eq.2.25).

The agreement with the bulk experimental measurements is in general very conclusive for the global pressure drop versus the global specific deposit (Figs. 2.9a-c). The measured pressure drops at $Re = 1.0$ are predicted very well by the CFD-DBF approach. At lower Re number of 0.5, the model slightly under-predicts the pressure drop for higher global specific deposits. One likely interpretation could be the increasing manifestation of liquid dead zones forming around the collectors' contact points. Such regions, acting as collection systems, narrow the useful area for flow and favor the accumulation of fines (see Narayan et al. 1997 photographs) which yield an increase in pressure drop which is not handled in the present model formulation. At the smallest Re value, the predictions are close to the measured pressure drops in the early and late DBF instances. Though the simulated profile exhibits a sigmoid shape in the intermediate $\langle \sigma(t) \rangle$ range which is not evidenced experimentally. Such peculiar numerical behavior can be ascribed to the effective specific surface area model which under-predicts the impact of the collecting assemblages, i.e., fines + collector, on the drag force when the specific deposits become large. There the cross-section fractions γ and β (Eqs.2.32, 2.33, 2.36) intervening in Eq.2.25 would require more sophisticated model formulations. It can also be due to the simplifications in the model regarding the dead zone collecting regions.

Acknowledgements

The authors thank the following institutions for their financial contributions: The Natural Sciences and Engineering Research Council of Canada, the Fonds pour la formation de chercheurs et d'aide à la recherche (Québec). The Los Alamos National Laboratory is also acknowledged for giving us access to the CFDLIB library of codes. A. O. would like to thank the financial support from CONACyT, Mexico and the Universidad Autonoma de Tlaxcala, Mexico.

Nomenclature

A_H	hidden area in downstream collector pole, m^2
A_s	Happel constant, –
A_Δ	shadow area, m^2
$\underline{\mathbf{a}}$	grid point representing a cell center in computational grid
$\bar{a}_{\beta\gamma}$	effective specific surface area, m^{-1}
B	local bed permeability, m^2
c	fine volumetric concentration (liquid volume basis), –
d	particulate diameter (collector or fine), m
$\underline{\mathbf{F}}_{\ell s}$	momentum exchange force, Pa/m
$\underline{\mathbf{g}}$	gravitational acceleration, m/s^2
H	Hamaker constant, J
h_K	Blake-Kozeny-Carman constant, –
k_d	deposit permeability, m^2
N	filtration rate (reactor volume basis), s^{-1}
$\tilde{N}_c$	number of collector in grid cell volume v, –
$\tilde{N}_f$	number of trapped fines in grid cell volume v, –
$\partial\tilde{N}_f$	number of peripheral fines per collector, –
N_G	gravitational dimensionless group, –
N_L	London – van der Waals dimensionless group, –
N_R	interception dimensionless group, –
P	pressure, Pa

p	Happel cell parameter
Re	Reynolds group, $\rho U d_c/\mu$
r	radial coordinate, m
t	time, s
U	fluid superficial velocity, m/s
$\underline{\mathbf{u}}_{\ell}$	velocity, m/s
v	grid cell volume, m^3
w	Happel cell parameter
X	momentum exchange rate coefficient, $kg/m^3/s$
Y	parameter in Eq. 2.17, –
z	longitudinal coordinate, m

Greek

β	collector cross-section fraction, –
δ	distance from clean collector center to coating border, m
ε	grid cell porosity, –
γ	fine cross-section fraction, –
λ	filter coefficient, m^{-1}
μ	viscosity, Pa·s
ρ	density, kg/m^3
σ	specific deposit (reactor volume basis), –
$\langle\sigma\rangle$	bed volume-averaged specific deposit, –

Sub/superscripts

c	collector
crit.	critical

d	deposit
f	fine
ℓ	liquid
o	clean bed state
s	solid

Acronyms

CFD	computational fluid dynamics
DBF	deep bed filtration
PDE	partial differential equation
TBR	trickle bed reactor

References

Al-Dahhan M.H., Larachi F., Duduković M.P. and Laurent A. (1997) High-pressure trickle bed reactors – A review. *Ind. Eng. Chem. Res.* **36**, 3292.

Brackbill J.U., Johnson N.L., Kashiwa B.A. and VanderHeyden W.B. (1997) *Multiphase flows and particle methods*. CFD'97, 5th Annual Conference of the Computational Fluid Dynamics Society of Canada, University of Victoria, Victoria, British Columbia, May 28, 29.

Chan E.W., Chung K.H., Veljković M. and Liu J.K, (1994) Hydrodynamics and fines capture in packed bed hydrotreaters. Canadian Conf. Chem. Eng., Ottawa, October 1994.

Chen J.W., Radoš N., Al-Dahhan M.H., Duduković M.P., Nguyen D. and Parimi C. (2001) Particle motion in packed/ebullated beds by CT and CARPT. *AIChE J.* **47**, 994.

Chiang H. and Tien C. (1985) Dynamics of deep bed filtration. Part I: Analysis of two limiting situations. *AIChE J.* **31**, 1349.

Choo C-u. and Tien C. (1995a) Simulation of hydrosol deposition in granular media. *AIChE J.* **41**, 1426.

Choo C-u. and Tien C. (1995b) Analysis of the transient behavior of deep-bed filtration. *J. Colloid Interface Sci.* **169**, 13.

Drew D.A. (1983) Mathematical Modeling of Two-Phase Flow. *Ann. Rev. Fluid Mech.* **15**, 261.

Drew D.A. and Passman S.L. (1998) *Theory of multicomponent fluids (Applied Mathematical Sciences (Springer-Verlag).* **Vol. 135**, Springer, New York.

Duduković M.P., Larachi F. and Mills P.L. (1999) Multiphase reactors – Revisited. *Chem. Eng. Sci.* **54**, 1975.

Dullien F.A.L. (1992) *Porous media fluid transport and pore structure*. 2nd edition, Academic Press Inc., San Diego.

Gray M.R. (2001). Private communication.

Herzig J.P., Leclerc D.M. and Le Goff P. (1970) Flow of suspensions through porous media, Application to deep bed filtration. *Ind. Eng. Chem.* **62**, 8.

Iwasaki T. (1937) Some notes on sand filtration. *J. Amer. Water Works Assoc.* **29**, 1591.

Jiang Y. Al-Dahhan M.H. and Duduković M.P. (2001) Statistical characterization of macroscale multiphase flow structures in trickle beds. *Chem. Eng. Sci.* **56**, 1647.

Kashiwa B.A., Padial N.T., Rauenzahn R.M. and VanderHeyden W.B. (1994) A cell-centered ICE method for multiphase flow simulations. ASME Symposium on *Numerical Methods in Multiphase Flows*. FED-vol. 185 .

Kashiwa B.A., and Rauenzahn R.M. (1994) A multimaterial formalism. ASME Symposium on *Numerical Methods in Multiphase Flows*. FED-vol. 185.

Koyama H., Nagai E., Torri H. and Kumagai H. (1995) Japanese refiner solver problems in resid desulfurization unit. *Oil & Gas J.* **93**, 8290.

Mackie R.I. Horner R.M.W. and Jarvis R.J. (1987) Dynamic modeling of deep-bed filtration. *AIChE J.* **33**, 1761.

Marcandelli C., Lamine A.S., Bernard J.R. and Wild G. (2000) Liquid distribution in trickle-bed reactors. *Oil & Gas Sci. & Technol.* **55**, 407.

Meyers R.A. (1996) *Handbook of petroleum refining processes*. 2nd edition, McGraw-Hill, New York.

Narayan R., Coury J.R., Masliyah J.H. and Gray M.R. (1997) Particle capture and plugging in packed-bed reactors. *Ind. Eng. Chem. Res.* **36**, 4620.

O'Melia C.R. and Ali W. (1978) The role of retained particles in deep bed filtration. *Prog. Wat. Tech.* **10**, 167.

Padial N.T., VanderHeyden W.B., Rauenzahn R.M. and Yarbro S.L. (2000) Three-dimensional simulation of a three-phase draft-tube bubble column. *Chem. Eng. Sci.* **55**, 3261.

Rajagopalan R. and Tien C. (1976) Trajectory analysis of deep bed filtration with the sphere-in-cell porous media model. *AIChE J.* **22**, 523.

Rege S.D. and Fogler H.S. (1988) A network model for deep bed filtration of solid particles and emulsion drops. *AIChE J.* **34**, 1761.

Sokolichin A. and Eigenberger G. (1994) Gas-liquid flow in bubble columns and loop reactors: Part I: Detailed modeling and numerical simulation. *Chem. Eng. Sci.* **49**, 5735.

Stephan E.A. and Chase G.G. (2000) Development of volume-average theory for deep-bed filtration. *AIChE J.* **46**, 1918.

Tien C. and Payatakes A.C. (1979) Advances in deep bed filtration. *AIChE J.* **25**, 737.

Tien C. (1989) *Granular filtration of aerosols and hydrosols*. Butterworths-Heinemann series in Chemical Engineering, Boston, MA.

Tien C. (2000) Hydrosol deposition in porous media: The effect of surface interactions. *Adv. Pow. Technol.* **11**, 9.

Trambouze P. (1991) Multiphase catalytic reactors in the oil industry, an introduction. *Rev. Inst. Franç. Pétr.* **46**, 433.

Trambouze P. (1993) Engineering of hydrotreating processes. In *Chemical reactor technology for environmentally safe reactors and products*. (pp. 425-442). NATO Ser. E, Applied Sciences, Eds. H.I. De Lasa, G. Dogu, A. Ravella .

Vigneswaran S. and Tulachan, R.V. (1988) Mathematical modeling of transient behaviour of deep bed filtration. *Wat. Res.* **22**, 1093.

Vigneswaran S. and Tien C. (1987) Transient behavior of deep-bed filtration of Brownian particles. *Chem. Eng. Sci.* **42**, 2729.

Wang S., Chung K.H., Masliyah J.H. and Gray M.R. (1999) Deposition of fine particles in packed beds at hydrotreating conditions: Role of surface chemistry. *Ind. Eng. Chem. Res.* **38**, 4878.

Wang S., Chung K.H. and Gray M.R. (2001) Role of hydrotreating products in deposition of fine particles in reactors. *Fuel.* **80**, 1079.

Table 2.1 Experimental DBF conditions simulated in CFD (Narayan et al. 1997)

Properties of materials

Liquid

Kerosene:

Viscosity; 2.14 mPa·s

Density; 784.3 kg/m^3

Re = 0.1; 0.5; 1

Fines

Carbon black

Diameter; 5-10 μm, 8 μm average

Density; 1768 kg/m^3

Influent concentration; 100-200 mg/L

Packing material

Glass spheres

Density; 2487 kg/m^3

Diameter; 1.0×10^{-3} m

Porosity; 0.37

Hamaker constant for glass-carbon-kerosene; 3.04×10^{-20} J

Geometry of the packed bed reactor

Diameter; 2.54 cm

Height; 30 cm

Table 2.2 Evolution of the global porosity change as a function of the global specific deposit

Re	0.1			0.5			1.0		
$\langle \sigma(t) \rangle$ [&]	1.7	3.2	4.9	1.2	2.7	4.6	1.0	2.2	4.2
D (%)[$]	1.4	2.4	3.7	0.9	2.0	3.6	0.9	1.7	3.2

[&] mg fines / mL bed [$] $D(\%) = 100 \times \frac{\langle \sigma(t) \rangle}{\rho_f \langle \varepsilon_o \rangle (1 - \varepsilon_d)}$

Figure captions

Figure 2.1 (a) Initial stage of deposition, mono-layer of fines on collectors (fine-collector interaction); (b) second stage of deposition, multiple-layer of fines on collectors (fine-fine interaction).

Figure 2.2 (a) Illustration of the shadow effect, the cross-section fractions of fine and collector; (b) sphere-in-cell representation of the fines' layer building up on top of collector for estimating the cross-section fraction, β, of collector.

Figure 2.3 Geometrical representation of the shadow area hidden by the fine on top of the collector.

Figure 2.4 Representative capture of an impinging fine via multiple interactions with anchored fines.

Figure 2.5 Initial solid volume fraction r-z distribution of the clean packed bed.

Figure 2.6 Contours at various clogging times of the specific deposit contour plots at different liquid Reynolds numbers. Snapshots taken at the approximately constant mean global specific deposit in the bed. Influent concentration co = 142 mg/L.

Figure 2.7 Contours at various clogging times of local permeability drop off expressed as 100×(Bo - B(t))/B(t) with respect to the initial clean bed state permeability field. Snapshots correspond to the same conditions as in figure 2.6. Permeability deviation evaluated at every grid cell center in the computational grid.

Figure 2.8 Contour various clogging times of the local porosity drop off expressed as 100×(εo - ε(t))/ε(t) with respect to the initial clean bed state porosity field. The snapshots correspond to the same conditions as in Figures 2.6. The porosity deviation is evaluated at every grid cell center in the computational grid.

Figure 2.9 Increase in pressure drop with mean global specific deposit at Reynolds numbers of (a) 1.0, (b) 0.5, (c) 0.1. Experimental data of Narayan et al. (1997), CFDLIB simulation using the momentum exchange coefficient (Eq. 2.23) referred to as the Koseny drag model. Influent concentration c_0= 142 mg/L.

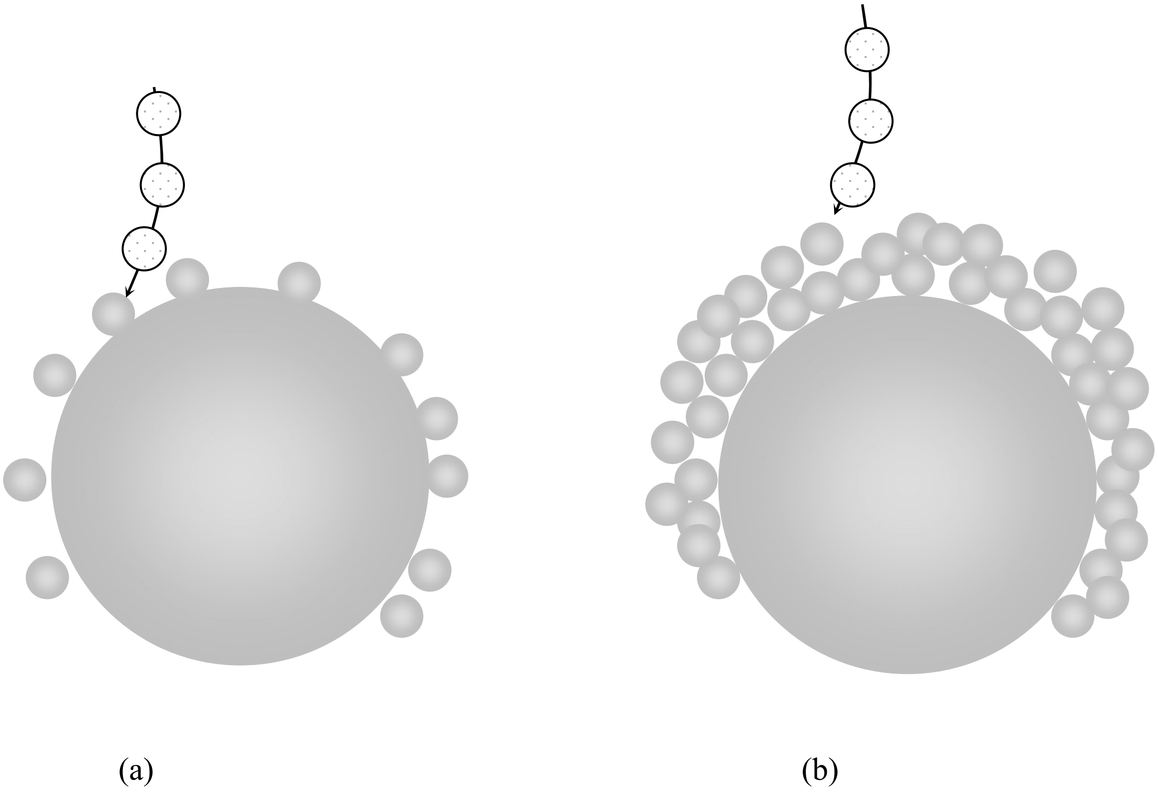

Figure 2.1 Deposition of fines on collectors (a) Initial stage, mono-layer (fine-collector interaction); (b) second stage, multiple-layer (fine-fine interaction).

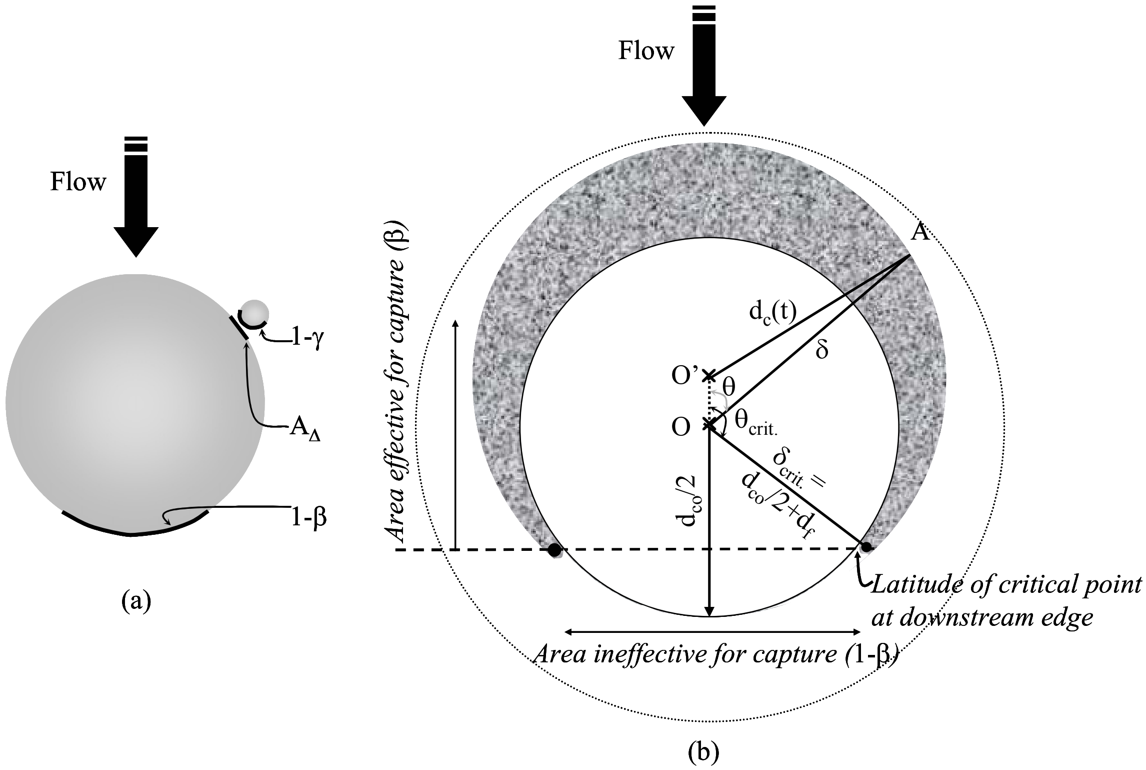

Figure 2.2 (a) Shadow effect, cross-sectional fractions of fine and collector; (b) sphere-in-cell fines' layer building up on top of collector for estimating the cross-section fraction β of collector.

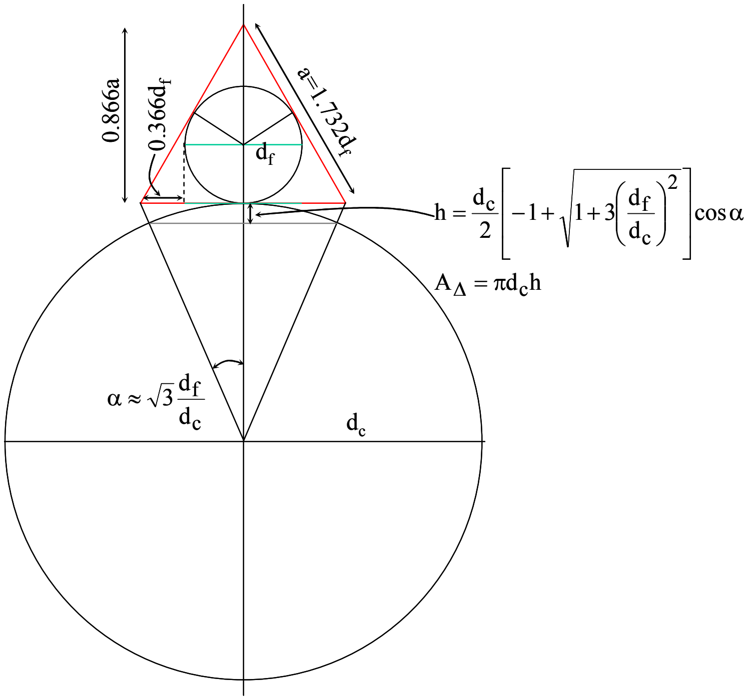

Figure 2.3 Geometry of the shadow area hidden by the fine on top of the collector.

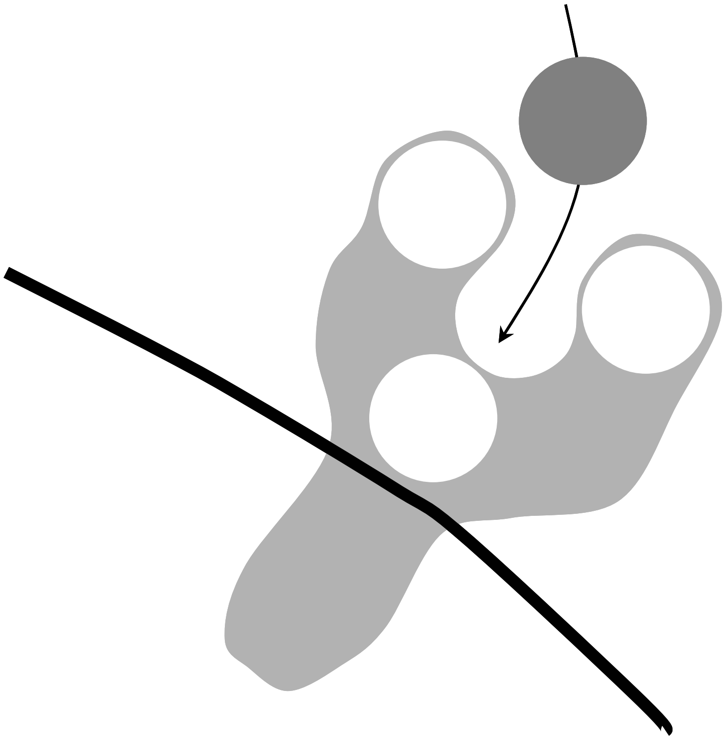

Figure 2.4 Representative capture of an impinging fine via multiple interactions with anchored fines.

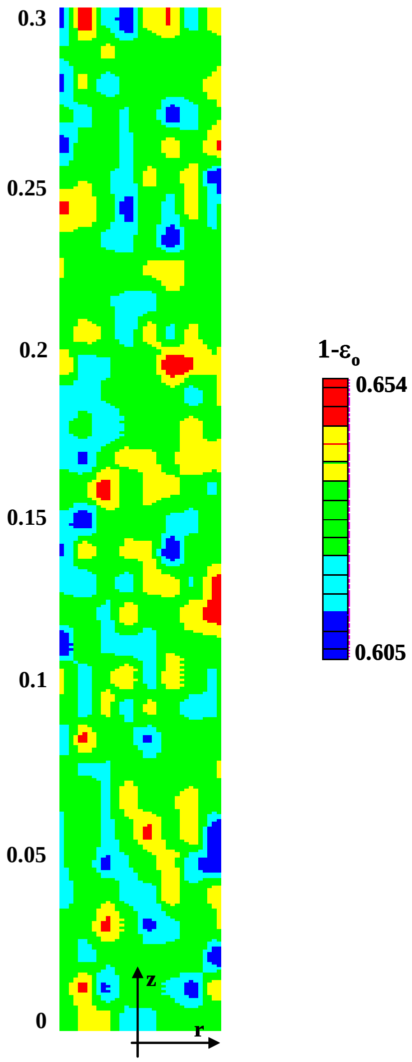

Figure 2.5 Initial solid volume fraction r-z distribution of the clean packed bed.

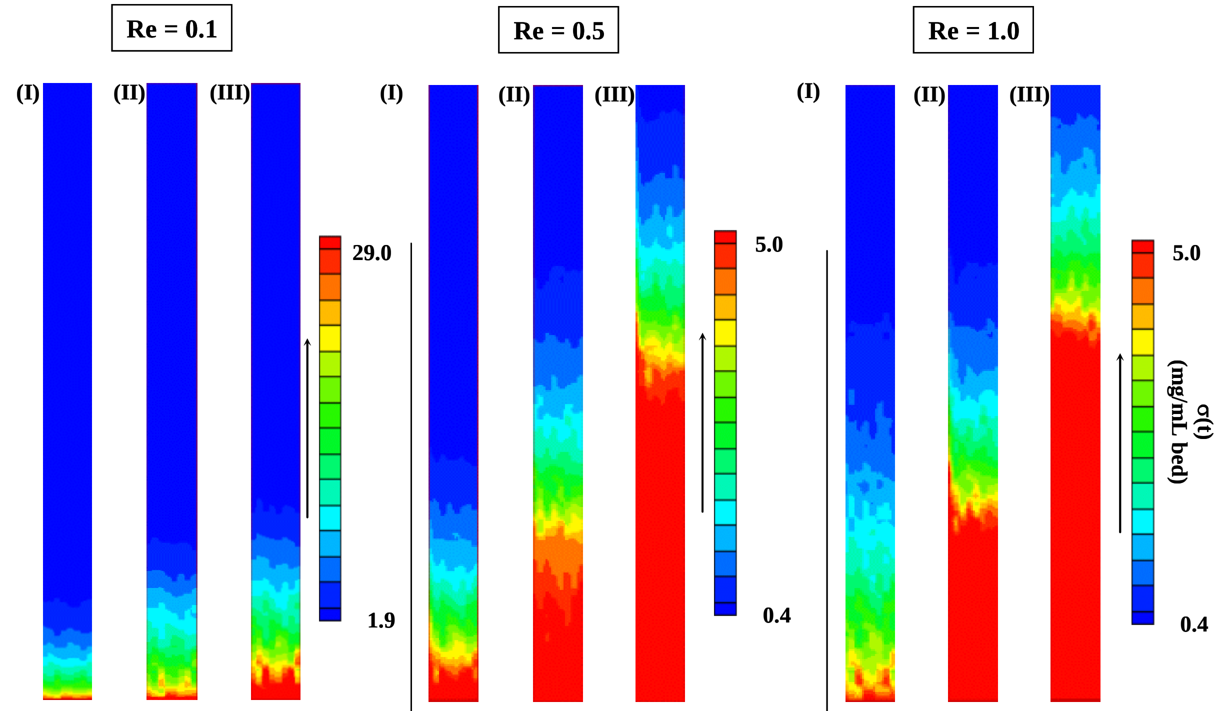

(a)

(I) $\langle\sigma(t)\rangle$=1.7 mg/mL bed; t = 2.0 h

(II) $\langle\sigma(t)\rangle$=3.2 mg/mL bed; t = 6.5 h

(III)$\langle\sigma(t)\rangle$=4.9 mg/mL bed; t = 10.25 h

(b)

$\langle\sigma(t)\rangle$=1.2 mg/mL bed; t = 3.3 h

$\langle\sigma(t)\rangle$=2.7 mg/mL bed; t = 8.0 h

$\langle\sigma(t)\rangle$=4.6 mg/mL bed; t = 16.0 h

(c)

$\langle\sigma(t)\rangle$=1.0 mg/mL bed; t = 4.0 h

$\langle\sigma(t)\rangle$=2.2 mg/mL bed; t = 11.5 h

$\langle\sigma(t)\rangle$=4.2 mg/mL bed; t = 20.0 h

Figure 2.6 Contours at various clogging times of specific deposit contour plots at different liquid Reynolds numbers. Snapshots taken at an approximately constant mean global specific deposit in the bed. Influent concentration c_o = 142 mg/L.

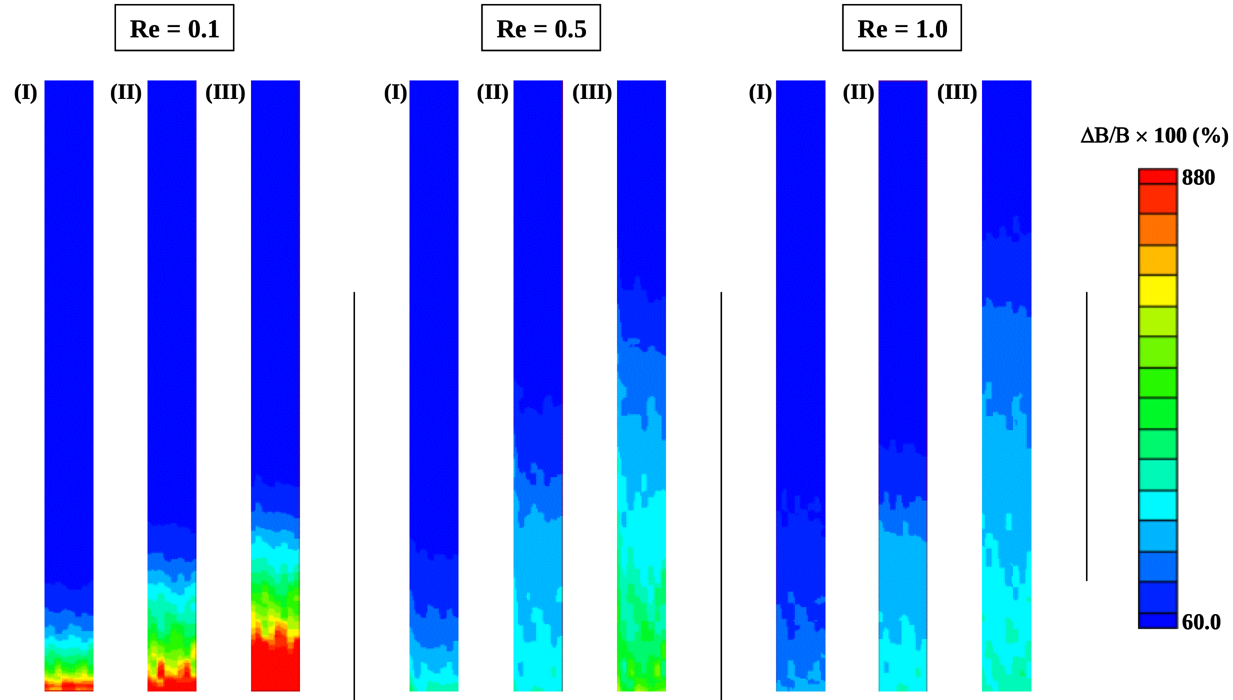

(a)

(I) $\langle\sigma(t)\rangle$=1.7 mg/mL bed; t = 2.0 h

(II) $\langle\sigma(t)\rangle$=3.2 mg/mL bed; t = 6.5 h

(III) $\langle\sigma(t)\rangle$=4.9 mg/mL bed; t = 10.25 h

(b)

$\langle\sigma(t)\rangle$=1.2 mg/mL bed; t = 3.3 h

$\langle\sigma(t)\rangle$=2.7 mg/mL bed; t = 8.0 h

$\langle\sigma(t)\rangle$=4.6 mg/mL bed; t = 16.0 h

(c)

$\langle\sigma(t)\rangle$=1.0 mg/mL bed; t = 4.0 h

$\langle\sigma(t)\rangle$=2.2 mg/mL bed; t = 11.5 h

$\langle\sigma(t)\rangle$=4.2 mg/mL bed; t = 20.0 h

Figure 2.7 Contours at various clogging times of local permeability drop off expressed as 100×[B_o - B(t)]/B(t) with respect to the initial clean bed state permeability field. Snapshots correspond to the same conditions as in figure 2.6. The permeability deviation is evaluated at every grid cell center in the computational grid.

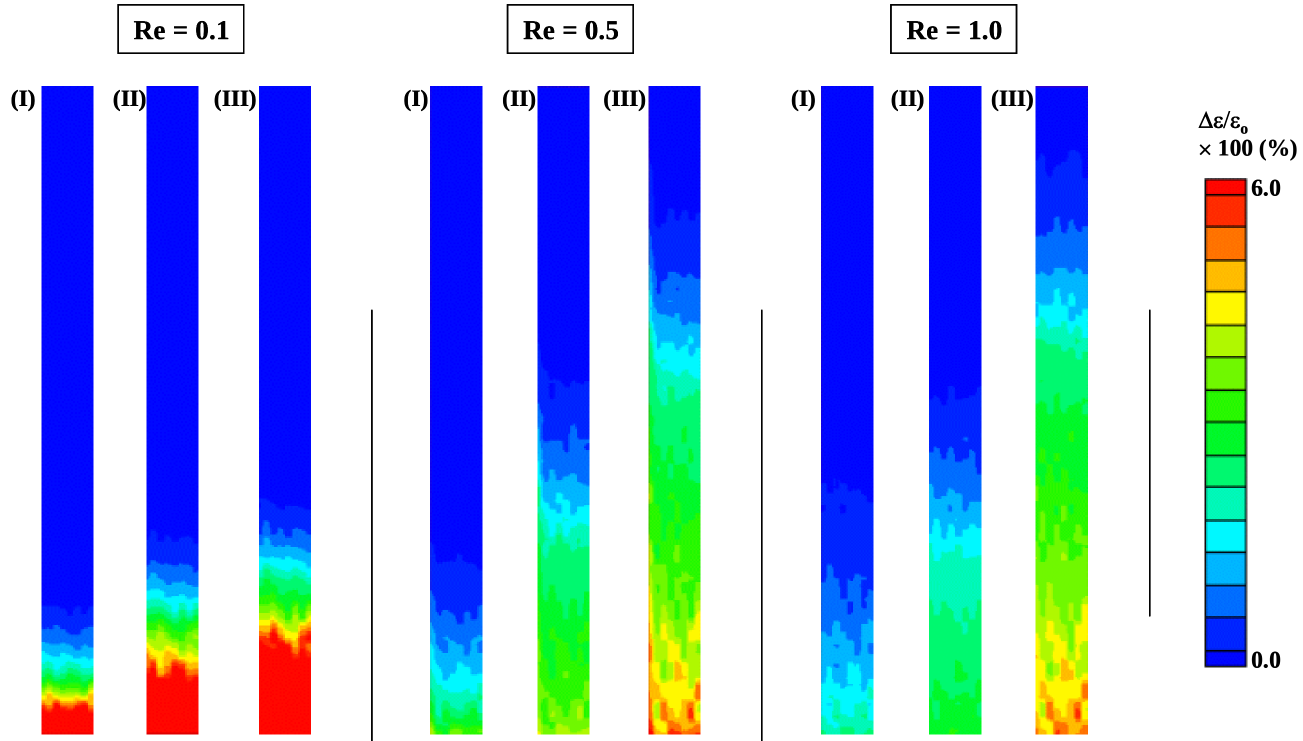

(a)

(I) $\langle\sigma(t)\rangle$=1.7 mg/mL bed; t = 2.0 h
(II) $\langle\sigma(t)\rangle$=3.2 mg/mL bed; t = 6.5 h
(III)$\langle\sigma(t)\rangle$=4.9 mg/mL bed; t = 10.25 h

(b)

$\langle\sigma(t)\rangle$=1.2 mg/mL bed; t = 3.3 h
$\langle\sigma(t)\rangle$=2.7 mg/mL bed; t = 8.0 h
$\langle\sigma(t)\rangle$=4.6 mg/mL bed; t = 16.0 h

(c)

$\langle\sigma(t)\rangle$=1.0 mg/mL bed; t = 4.0 h
$\langle\sigma(t)\rangle$=2.2 mg/mL bed; t = 11.5 h
$\langle\sigma(t)\rangle$=4.2 mg/mL bed; t = 20.0 h

Figure 2.8 Contours at various clogging times of the local porosity drop off expressed as $100\times(\varepsilon_o - \varepsilon(t))/\varepsilon(t)$ with respect to the initial clean bed state porosity field. The snapshots correspond to the same conditions as in Figures 2.6. The porosity deviation is evaluated at every grid cell center in the computational grid.

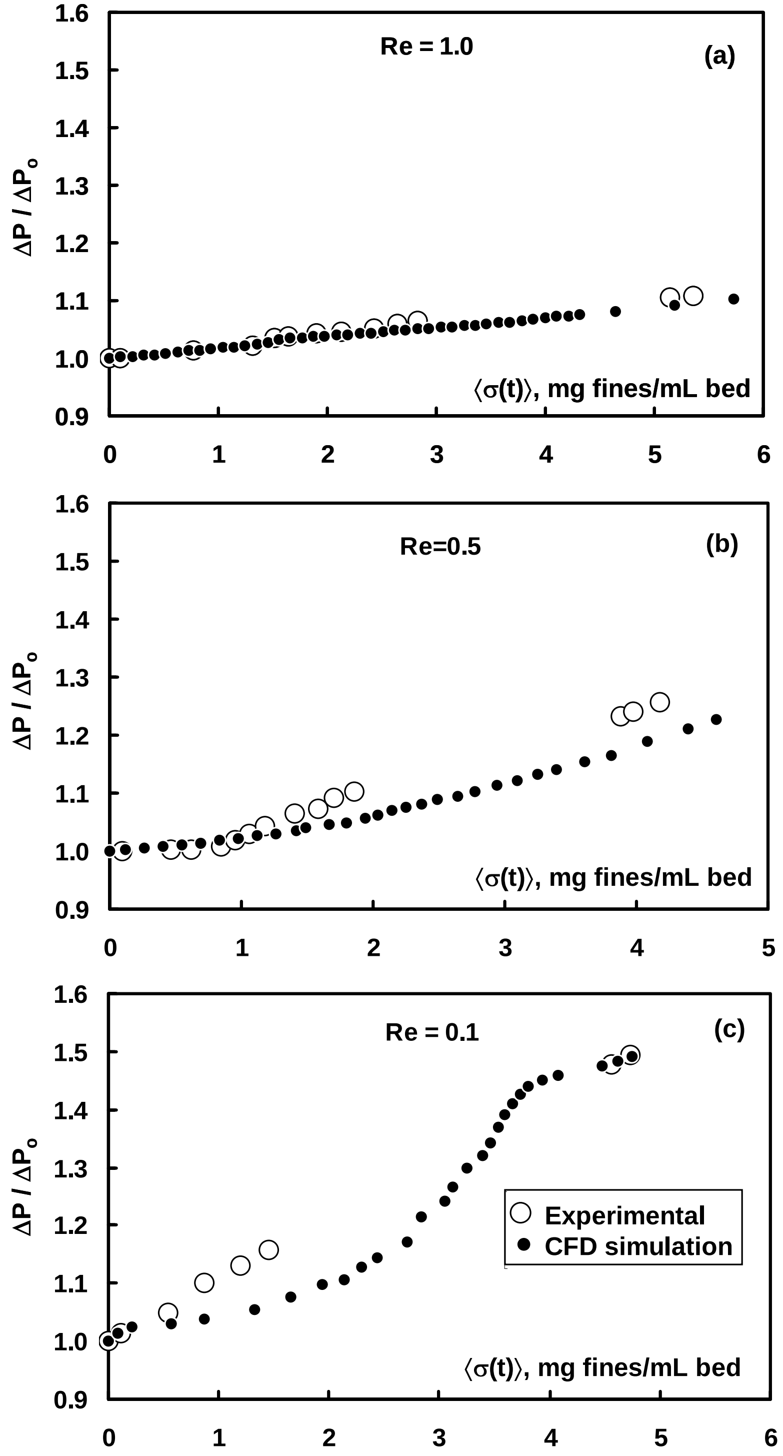

Figure 2.9 Increase in pressure drop with mean global specific deposit at Reynolds numbers (a) 1.0, (b) 0.5, (c) 0.1. Experimental data of Narayan et al. (1997), CFDLIB simulation using the momentum exchange coefficient (Eq.2.23) referred to as the Kozeny drag model. Influent concentration c_o = 142 mg/L.

CHAPTER 3

Modeling of clogging in two phase trickle flow packed bed reactors

Résumé

Une approche hybride utilisant un procédure extraite de la mécanique des fluides numérique de type Euler-Euler a été développée pour représenter l'évolution de la perte de pression dans des réacteurs à lit fixe arrosé subissant la capture de particules de grandeur colloïdale et non colloïdale dans des conditions de filtration en profondeur. L'équation balistique Lagrangienne de trajectoire pour analyser l'interception de particules a été adaptée aux écoulements biphasiques en utilisant une fente inclinée comme géométrie de base du collecteur. De nouvelles équations pour les efficacités de collection et les coefficients de filtration ont été établies pour les diverses étapes de filtration qui se produisent dans les écoulements monophasiques et à lit fixe arrosée pour les mécanismes de capture en monocouche et multicouche. Ces expressions basées sur le modèle de fente, ont été établies pour des liquides non-polaires et non-électrolytiques semblables au pétrole et à des liquides de l'industrie de raffinage où il existe un réel besoin pour modéliser la filtration en profondeur en écoulement multiphasique. En incluant les nouvelles expressions de coefficient d'efficacité et de filtration dans un code multidimensionnel de mécanique de fluides en état non stationnaire, le procédé de filtration en lit fixe arrosé a été simulé et l'augmentation de la perte de pression pendant le colmatage a été expliquée par l’accroissement de la surface spécifique locale des collecteurs et l’abaissement de la porosité locale due au dépôt de particules. Les simulations ont été comparées aux données de perte de pression de Gray et al. 2002 (Can. J. Chem. Eng., 80, 346) dans leur étude qui utilisait le système kaolinite-kérosène-air comme modèle de colmatage dans les réacteurs à lit fixe arrosé.

Lagrange-Euler-Euler CFD approach for modeling deep bed filtration in trickle flow reactors

(by A. Ortiz-Arroyo, F. Larachi)

[Paper accepted in: Separation & Purification Technology, May 2004]

Abstract

A Lagrange-Euler-Euler computational fluid dynamic approach was developed to represent the evolution of two-phase pressure gradients in trickle-bed reactors undergoing deposition of colloidal/non-colloidal fines under deep-bed filtration conditions. The ballistic trajectory equation to analyze fines interception was extended to two-phase flows using the inclined slit as the basic collector geometry. New equations for the collection efficiencies and filter coefficients were established for the various filtration stages encountered in single-phase flow and trickle flow regime both for monolayer and multilayer collection mechanisms. These slit-based expressions were established for non-polar and non-electrolytic petroleum-like liquids where there is a need for the refining industry to model deep-bed filtration in multiphase flow. By embedding the new collection efficiency and filter coefficient expressions in an unsteady-state multidimensional computational fluid dynamics code, the deep bed filtration process in trickle flow reactors was simulated and the increase of pressure drop during plugging was explained by increasing local specific surface area and decreasing local porosity due to fines deposition. The simulations were benchmarked using the experimental pressure drop data and observations of Gray et al. 2002 (Can. J. Chem. Eng., 80, 346) in their study of kaolinite-kerosene-air flows in trickle bed reactors.

Keywords trajectory analysis, filter coefficient, Brinkman flow, inclined slit model, pressure drop, filtration, plugging, hydrotreating, colloidal and non-colloidal fines

3.1 Introduction and Background

3.1.1 Plugging with fines in the petroleum refining industry

Regardless of the several energy scenarios advocated by industry analysts, a consensus emerges that the world primary energy demand will roughly double from current 9Gtoe to 18Gtoe at 2020 horizon. Projections forecast that both conventional and non-conventional oil reserves are to contribute for 40% of all energy consumed over the next two decades. On the other hand, progressive exhaustion of conventional oil and the increasing needs for petroleum light products are forcing the oil sector to exploit non-conventional hydrocarbon deposits such as heavy crude oils and bitumen (Wauquier, 1994, Speight, 1999, 2001, Bauquis, 2002). Heavy crude grades including oil sand bitumen are among the world's largest resources with estimated 1.7 trillion barrels ultimate reserves only for Canada Athabasca bitumen (Bauquis, 2002). Bitumen processing will thus increasingly become ubiquitous in the petroleum industry in this part of the hemisphere where the syncrude growth capacity from bitumen conversion is projected to reach 1,200mbblpsd by 2005 (Sanaie et al. 2001, Rahimi et al. 2001).

Primary upgrading of the oil sand bitumen vacuum bottoms yields a syncrude, almost half of which is contributed by heavy gas oil, a major FCC feedstock. The market niche for this hydrocarbon fraction is thwarted by the heavy gas oil high aromaticity and high heteroatom (especially sulfur) content, and most importantly by the carryover of fines in the downstream hydrotreating units. While secondary upgrading mitigates gas oil aromaticity through partial hydrogenation and cycloparaffinic ring opening; it also reduces the objectionable sulfur through hydrotreating. However, the fines carryover severely limits the heavy gas oil hydrotreating capacity due to bed plugging by putting out of business important quantities of costly catalyst after abnormally short time-on-stream periods. Being of various origins, such fines naturally occur as reservoir-mud mineral solids (Narayan et al., 1997), or represent recalcitrant clay intruders that worm into the mineral processing upstream units, or even originate in the cokers through thermally-triggered asphaltene/resin condensation/polymerization of aromatic rings (Wang et al., 1999, 2001, Tanabe and Gray, 1997), or ultimately may build up in the form of corrosion-induced iron sulfide scales in upstream units (Wang et al., 1999, Brossard, 1996).

The trickle bed hydrotreaters consist of fixed beds of randomly packed catalyst pellets operating under elevated pressure and temperature (Dudukovic et al., 1999, 2002) for hydroprocessing the heavy gas oil suspensions in a H_2-rich atmosphere co-currently downwards to reduce aromaticity and sulfur impurities. In the mid and long terms, the fines conveyed in the gas oil are increasingly intercepted by the catalyst bed and ultimately forbid access for above friendly reactions. As a matter of fact upstream filtration in guard filters effectively intercept >20μm particles but not all the <20μm fines, leaving the undesirable fines slowly plug the bed. Despite a low concentration of the incoming fines (~100ppm), the cumulative effect of tens of thousands of barrels of heavy gas oil feed each day diverts the hydrotreater to a giant filter collecting hundreds of kilograms of fines. Fines accumulation causes the pressure to rise by restricting the flow via porosity reduction and increased momentum transfer area of the collectors. Eventually, the pressure drop becomes so high that the hydrotreaters are shutdown and the *still-chemically-active* catalyst replaced. As a result, fines deposition prematurely shortens hydrotreater cycle life, increases operational problems and maintenance work leading to poor energy efficiency.

There is a remarkable paucity in technological remedies to combat fines plugging. Current response is to leave the bed collecting fines until the pressure drop climbs to a critical level forcing plant shutdown (Gray et al., 2002) or until the blinded catalyst no longer functions to meet refiner specifications. While changing the obstructed bed with a new clean packing unit alleviates the problem, loss in profitability may be dramatic as the precious metal impregnated catalytic bed is still active. For the time being, two strategies have been attempted to allay the curse of plugging.

One route is to mitigate propensity of fines to attach or to flocculate to reduce capture on the catalyst grain (collector) through cake- or deep-bed filtration mechanisms (Wang et al., 1999, 2001). This could be achieved by chemically altering fines surface by adsorbing solutes, *e.g.*, surfactants, or by adding asphaltene to gas oil. By forming layers with sterically repulsive forces, the suspension is stabilized, the deposition is inhibited and the plugging is retarded. However, the actual high temperatures along with H_2, and build-up of H_2S and H_2O during gas oil hydrotreating promote the asphaltene desorption from fines, and the asphaltene catalyzed decomposition over captured fines. The first event prompts cake filtration amidst the buoyant fines floating in the gas oil suspension, whereas the second weakens the fines steric resistance so that it attaches strongly to the collector.

Another route to prolong hydrotreater cycle life is through the top bed grading technology. It was patented by Chevron to cope with the high levels of insoluble iron in the vacuum residuum desulphurisation hydrotreating of some crudes (Brossard, 1996). The solution is designed to impede inception of localized *plugging spots* via physical grading of the catalyst by size and shape. Fines are filtered out over several layers of graded catalyst, thus reducing their tendency to capture at one point of the reactor. Similar grading is also used in the UOP reduced crude desulphurisation Unionfining hydrotreaters. These are loaded with the CDS-NP macaroni catalyst from larger to smaller size to maximize void space and catalyst surface area for interception (Thompson, 1996).

3.1.2 Filtration issues in trickle-bed reactors

Studies of fines deposition in packed beds experiencing non-ionic liquid flows tend to support the contention that plugging with petroleum-like suspensions occurs via deep bed filtration mechanisms (Narayan et al., 1997). Deep bed filtration has its roots in the vast area of water treatment and purification. A water effluent contaminated with small suspended solids circulates through a granular filter. Some of the contaminating solids impact the collectors' surface for retention by surface forces. Once the polluting particles are captured, the fluid leaves the filter as a purified liquid stream. It is generally accepted that deep bed filtration proceeds following three stages: initial, ripening and obstruction. In the initial stage, the incoming fines impinge on the immaculate collectors and are collected through clean collector-fine interactions until a monolayer has completed. During the ripening stage, the collectors being completely covered, the subsequent incoming fines contribute to multilayer deposition through fine-fine interactions. Ultimately, under severe deposition, the filter behaves as a cake filter and must be shutdown for cleaning.

Despite the important efforts invested over several decades to understand its underlying phenomena, deep bed filtration remains a vividly researched topic. Interminglement between the multiphase hydrodynamics, the fine-collector and fine-fine surface interactions, and the physicochemical mechanisms developing inside the porous bed makes the process fundamentals difficult to grasp. Among the various methods conceived to analyze and simulate deep bed filtration, *trajectory analysis* is recognized as the approach of choice to provide insights into the mechanisms in play (Tien, 1989, Rege and Fogler, 1988).

Extension of trajectory analysis outside the realm of water treatment, and particularly to gas-liquid flow systems involving petroleum organic liquids has not deserved appropriate attention. Recently, Larachi and coworkers (Ortiz-Arroyo et al., 2002, Iliuta et al., 2003a, 2003b, 2004) postulated that water-based single-phase flow trajectory analysis in granular filters, such as those proposed by Rajagopalan and Tien, 1976, were also applicable to trickle-bed filtration for the estimation of the collection efficiencies and the filter coefficients. While the same governing hydrodynamic equations describe plugging in trickle beds and in granular filters (Narayan et al., 1997), few key distinctions must however be emphasized. There is no obvious reason that the collection efficiency and filter coefficient equations in single-phase flow filtration are equivalent to those prevailing under gas-liquid flow conditions. The diameter of collectors and vessel in granular beds, and liquid hourly space velocity are much smaller than in trickle beds. A (flowing) gas phase in granular filters being absent, liquid holdup (i.e., bed porosity) decreases with the advancement of deposition. Conversely, in trickle beds the presence of a flowing gas phase may reduce liquid holdup, influence both the liquid velocity field and the extent of deposition as well as eventual accumulation of fines at the gas-liquid interface. The fluids throughputs differ substantially in both applications: in trickle beds, gas and liquid velocities range typically from 0.05 to 0.5 m/s and 0.001 to 0.025 m/s, respectively. In granular filters, liquid velocities are generally far less than 0.001 m/s and Darcy's law typically applies to model the pressure build up due to fine collection in deep bed filtration. In trickle beds, the inertial effects are non-negligible and Darcy's law is inadequate as a drag force model at higher gas and liquid velocities (Saez and Carbonell, 1985).

3.1.1 Computational fluid dynamics in trickle bed filtration

Steady- and unsteady-state hydraulics inside trickle-bed reactors have been modeled using numerous approaches, including the diffusion model (Stanek and Szekely, 1974), the 1-D slit model (Holub et al., 1992, Iliuta et al., 2002), the discrete cell model (Holub, 1990, Jiang et al., 2000), and multidimensional computational fluid dynamics modeling (Jiang et al., 1999, 2001), etc. At present, the representation of the complex random porous interstitial space of the bed is among the most challenging issues. However, despite direct numerical simulation of the porous space appears to give promising insights into the flow behavior (Dixon and Nijemeisland, 2001) the approach is still out of reach in terms of actual available computational power to deal with multiphase flows such as in trickle beds.

A convenient way to model multiphase flows through porous media using computational fluid dynamics is provided in the form of *k*-fluid Euler formulation. The advantage of this approximation is that it views the computational domain as made up of probabilistic volume fraction contributions arising from interpenetrating continua, i.e., each phase occupying a computational cell, without requiring detailed knowledge of the local porous medium geometry. In such description in particular, the identity of the individual particles making up the porous medium is lost and each phase is treated as a pseudo-continuum in each computational cell (Drew and Passman, 1998). Using such *k*-fluid Euler formulation, Dudukovic and coll. (Jiang et al., 1999, 2000, 2001, Kumar, 1995, Khadilkar, 1998) succeeded in obtaining numerical representations of the bed hydrodynamics and of maldistribution in gas-liquid flow trickle beds.

Plugging of packed beds is by nature multidimensional and non-steady state, in which the bed properties, the flowing behavior of phases, and the gas-liquid-solid interactions evolve in space and time. Given these characteristics, computational fluid dynamics is the perfect tool for modeling deep bed filtration in trickle-bed reactors as it permits visualization and tracking of the bed properties and hydrodynamics during the filtration cycle both at global and local scales. It is also expected that in near future with the aid of powerful non-invasive visualization techniques, it will become possible to benchmark detailed multidimensional models asserting the fine structure of plugging in trickle beds.

Computational fluid dynamics modeling has proved its potential when applied to the plugging in single-phase flow in packed beds (Ortiz-Arroyo et al., 2002) in which closure equations for the collector-fluid interaction as well as a representation of the surface of the collectors was proposed. Using the CFDLIB library of codes from Los Alamos National Laboratory (Kashiwa et al., 1994), the flow in packed beds was modeled with an Euler-Euler model in which the fines were introduced as a pseudo-phase included in the liquid that exchanged mass (i.e., fines) with the collectors. Local porosity and permeability were tracked in time throughout the whole bed, and the bed pressure drop during plugging was compared favorably with the experimental data of Narayan et al., 1997.

By extension to our previous works (Ortiz-Arroyo et al., 2002, Iliuta et al., 2003a, 2003b, 2004), the objective of this contribution is to develop a new Lagrange-Euler-Euler computational fluid dynamic approach to model fines deposition and the rise of two-phase pressure drop in deep bed filtration in trickle-bed reactors. Specifically, a new model is proposed to estimate the rate of deposition of colloidal and non-colloidal fines in gas-liquid trickle flow by extending the Lagrangian trajectory analysis to two-phase flows using the inclined slit as collector geometry. While the inclined slit model could represent a rudimentary model unable to fully capture the truly complex bed geometry as well as possible fines accumulation at the gas-liquid interface, it is still adopted in our work because of its simplicity and widespread use in the circle of researchers dealing with trickle-bed reactors hydrodynamics. The inclined slit model is used to obtain new equations for the collection efficiencies and the filter coefficients for the various filtration stages including single-phase, clean bed trickle flow (monolayer collection) and trickle flow in the ripening stage (multilayer collection). Following a previously proposed area model (Ortiz-Arroyo et al., 2002, Iliuta et al., 2003, Stephan and Chase, 2000), the increase of pressure drop during plugging was explained by an increasing local surface area and decreasing local porosity due to fines deposition. These obtained filtration equations are embedded in an unsteady-state multidimensional computational fluid dynamics code to simulate the deep bed filtration process in trickle flow reactors.

3.2 Modeling

While traveling in a liquid through a porous medium, the trajectories of the fines are influenced by the flowing fluids [either being carriers (e.g., liquid) or non-carriers (e.g., a flowing gas)], by the fines own inertia, and by several surface phenomena as fines get increasingly closer to the collector or to the gas-liquid interface. In deep bed filtration, *trajectory analysis* refers to a powerful Lagrangian methodology that enables estimation of the collection efficiency from integration of the ballistic trajectories of fines as they move towards a collector. This methodology requires specification of the collector geometry and porous medium model, the flow fields in the vicinity of the collector, and the forces acting upon the fines (Tien, 1989, Tien and Payatakes, 1979, Tien, 2000).

The trajectory equation is constructed by formulating the force and torque balances on the traveling fine. It broadly encompasses (long-range) forces/torques acting on the fine remote from the collector, and those (short-range) affecting the fine when it gets *close* to the collector. In non-polar non-Brownian systems, the long range forces/torques include gravitational, drag and inertial effects caused by the movement of the liquid (and gas) and the mass of fine, whereas short range forces/torques are triggered by the presence of the collector surface as well as molecular dispersion forces (London force/torque). Solution of the trajectory equation is attempted in the case of the *limiting trajectory* which is determined by backward integration from some point at a distance from the collector equal to a fine radius until a point far upstream or at the collector entry. In the capillary model for instance, the limiting trajectory is the path of the fine that is captured at the collector exit, tracking backwards the fine until the entry point.

As will be discussed in the forthcoming sections, knowledge of the limiting trajectory enables access to the collection efficiency and filter coefficient both in monolayer and multilayer deposition conditions either in single-phase (liquid) or two-phase (gas-liquid) operation.

3.2.1 Limiting trajectory and (monolayer) collection efficiency in slit geometry

The slit model is adopted to represent the porous medium geometry because of its simplicity and demonstrated capacity to predict the trickle-bed hydrodynamic parameters (Holub et al., 1992, 1993, Iliuta et al., 1998). The liquid velocity distribution is derived using the film flow assumption in the slit (Fig. 3.1a) so that the trajectory analysis for the fines in this geometry can be implemented both for single-phase and multiphase flow conditions. To extend the trajectory analysis to two-phase trickle flow it is necessary to postulate that the capture mechanisms in two-phase flows are essentially similar to those occurring in single-phase flows; the main difference being the effect of the gas phase on the liquid film velocity distribution. Hence it is reasonable to use the same structure of the capture equation as well as the same procedure to obtain the collection efficiencies as in single-phase flow. It must be stressed out however that some phenomena known to manifest at the gas-liquid interface have been neglected in the present analysis of fines accumulation. An example is fines migration to the gas-liquid interface caused by fine surface properties akin to froth flotation in mineral processing. The importance of such migration of fines in trickle bed flows is still to be elucidated as well as the criteria to be used to identify whether it is important or not. Another issue relates to size and wettability (or contact angle) of fines which may have an importance and that has also been neglected in the present development.

For organic non-electrolytic non-polar petroleum-like liquids, the main mechanism that drives collection of non-colloidal fines (>1μm) is interception (Tien, 1989). The dimensionless groups representing the relative importance of gravitational and viscous forces, N_G, the interception parameter, N_R, and the relative importance of the London - van der Waals forces and the viscous forces, N_{Lo}, are defined respectively, as:

$$N_G = \frac{\left(\rho_f - \rho_\ell\right) d_f^2 \, g}{18\pi\mu_\ell \, u_\ell} \tag{3.1}$$

$$N_R = \frac{d_f}{d_c} \tag{3.2}$$

$$N_{Lo} = \frac{4Ha}{9\pi\mu_\ell \, d_f^2 \, u_\ell} \tag{3.3}$$

The trajectory equation can be established using the collection model for periodic constricted tubes (Tien, 1989, Tien and Payatakes, 1979, Payatakes et al., 1974b). The equation describing the two-dimensional trajectories of fines in cartesian coordinates is easily found with the aid of the collection model in periodic constricted tubes after simplification of the electrochemical force terms:

$$\frac{\mathrm{d}y}{\mathrm{d}z}=\frac{-N_G\sin\theta-\dfrac{N_{Lo}\alpha_{sp}}{\delta^{+2}\left(2+\delta^+\right)^2}}{B^+F_4y+D^+F_5y^2+N_GF_6\cos\theta} \tag{3.4}$$

In the original equation, the angle θ describes the changing curvature of the collectors. If the angle is constant and equal to the slit inclination, it can be readily recognised that Eq.3.4 represents that of an inclined wall. In Eq.3.4, F_4, F_5, F_6 are *universal* functions expressed as a function of the dimensionless fine-wall distance, δ^+. They are computed using the approximate expressions developed by Payatakes, 1973 and revised by Tien and coll. (Tien, 1989, Vaidyanathan and Tien, 1988). The retardation factor, α_{sp}, for the London forces as a function of the fine-wall distance δ^* is calculated using the approximate expressions developed by Payatakes, 1973 and provided in Tien, 1989. B^+ and D^+ are constants that depend on the local liquid velocity profile. These constants are estimated by assuming that the flow field is parabolic and therefore knowledge of the liquid film flow distribution is mandatory. y and z are the coordinates crosswise from the slit wall and streamwise from the slit entry, respectively (Fig. 3.1a).

The limiting trajectory is calculated by backward integration of Eq.3.4 starting from the farthest point of capture of the fine (the slit exit) backwards to the slit entry; i.e., from $z=L$ to $z=0$, where L is the slit length. The initial condition for integration is $y=a_p$ (the radius of a fine) and finalizing integration upstream at $y=Y_c$ and $z=0$ (Fig. 3.1b).

Integration of the trajectory differential equation is made by an Adams-Bashforth-Moulton solver in which special attention is given to the first integration step as detailed by Payatakes, 1973 and Tien, 1989.

Provided the liquid velocity distribution, $u_{\ell z}(y)$, across liquid thickness δ in the slit is known, the *non-Brownian* monolayer collection efficiency can be calculated considering a uniform inlet concentration of fines in the feed stream:

$$\eta^{nB}=\frac{\text{fines deposition rate}}{\text{incoming fines rate}}=\frac{\int_{a_p}^{Y_c}u_{\ell z}(y)\mathrm{d}y}{\int_0^{\delta-a_p}u_{\ell z}(y)\mathrm{d}y} \tag{3.5}$$

For fines in the colloidal range (≤1μm), the Brownian motion has to be accounted for. Inclusion of a term due to the Brownian movement of submicron particles in the force balance of the trajectory equation leads to a stochastic trajectory equation of difficult solution (Rajagopalan and Tien, 1976). To overcome this additional complexity, it is usually assumed that collection exhibits simple additive property (Rajagopalan and Tien, 1976, Tien and Payatakes, 1979). To account for the collection due to Brownian forces, a term is added to the monolayer collection efficiency, Eq.3.5:

$$\eta^o = \eta^{nB} + \eta^B \tag{3.6}$$

The contribution of Brownian diffusion to deposition is generally assumed to be akin to a pure mass transfer process in the absence of surface interaction forces (Tien, 1989). To evaluate η^B, the Brownian diffusivity D_B and the liquid-solid mass transfer coefficient in the slit are required. As no specific liquid-solid mass transfer correlations are known to exist for the slit geometry, use is made of general liquid-solid mass transfer correlations developed for trickle-beds Larachi et al, 2003a, Larachi et al., 2003b where the ordinary diffusion coefficient appearing in the Sherwood and Schmidt numbers is replaced by D_B (Tien, 1989):

$$D_B = \frac{c_s kT}{3\pi d_f \mu_\ell} \tag{3.7}$$

Where c_s is the Cunningham correction factor and k is the Boltzmann constant.

To compute the monolayer collection efficiency from Eq.3.6, the liquid velocity profiles in single- and two-phase trickle flow conditions are required.

3.2.1.1 Liquid velocity distribution in single-phase flow

The slit half-wall thickness, S, half-void thickness, w, length, L, and liquid film thickness, δ, are expressed as a function of the bed porosity, ε, bed specific surface area, $a_{\ell s}$, and liquid holdup, ε_ℓ (which is equal here to the bed porosity). For a complete description of the slit model, the reader can consult the following references (Holub et al., 1992, Iliuta et al., 2002, Holub, 1990):

$$S = \frac{1-\varepsilon}{a_{\ell s}} \tag{3.8}$$

$$\frac{w}{S}=\frac{\varepsilon}{1-\varepsilon} \quad (3.9)$$

$$\frac{\delta}{S}=\frac{\varepsilon_\ell}{1-\varepsilon} \quad (3.10)$$

In single-phase flow, the liquid velocity profile in the slit with an inclination angle θ (Fig.3.1) is obtained from integration of the differential momentum balance equation for a pressure-driven (Poiseuille) flow in an inclined slit with non-slip boundary conditions at the walls:

$$u_{\ell z}(y)=-\frac{y^2-S^2}{2\mu_\ell}\left(\rho_\ell g\cos\theta-\frac{\mathrm{d}P}{\mathrm{d}z}\right) \quad (3.11)$$

The parabolic velocity distribution in the liquid phase is calculated using Eq.3.11 after the slit pressure gradient, -d*P*/d*z*, is calculated from the (clean) bed pressure drop $-\Delta P/H$ using the single-phase flow slit model (Holub et al., 1992):

$$\frac{1}{\cos\theta}\left(-\frac{\mathrm{d}P}{\mathrm{d}z}+\rho_\ell g\cos\theta\right)=-\frac{\Delta P}{H}+\rho_\ell g \quad (3.12)$$

Where in single-phase flow, the bed pressure model structure is Ergun-like:

$$-\frac{\Delta P}{H}+\rho_\ell g=E_1\frac{Re_\ell}{Ga_\ell}+E_2\frac{Re_\ell^2}{Ga_\ell} \quad (3.13)$$

Combining integration of Eq.3.4 with Eq.3.6 after inclusion of Eq.3.11 enables computation of the monolayer collection efficiency in single-phase flow, η^o.

It is worth to pinpoint that the slit model remains a simplistic approach to model the actual pore space in trickle beds. As no sophisticated pore-level models are available at present in the trickle bed literature, as such the slit model provides a preliminary platform for particle trajectory analysis since neither surface curvatures nor converging-diverging features in the liquid flow field are accounted for yet. However, being geometrically close to the capillary model of Payatakes et al., 1974a, the slit model is expected to provide closer collection efficiency values.

Moreover, although it is assumed here that the fines trajectories in the slit-shaped pores keep a two-dimensional character, there is no restriction to adopt more elaborated three-dimensional trajectory analyses such as those developed recently by Payatakes and coworkers (Paraskeva et al., 1991, Burganos et al., 1992, Burganos et al., 1995).

3.2.1.2 Liquid velocity distribution in two-phase flow

In two-phase flow, the liquid is postulated to fully wet the slit wall with a uniform-thickness film, δ, while the gas fills the remaining slit core, w- δ. As in single-phase flow, the slit inclination angle θ is related to the Ergun constants representing the bed structure and depends on bed tortuosity, T, as cos θ = T^{-1} (Holub et al., 1992). Both θ and T can be inferred from the Ergun creeping and inertial constants, E_1 and E_2, to be determined *a priori* using single-phase pressure drop measurements across the dry bed or using empirical correlations. Such latter constants reflect at the bed level, the average inclination of the randomly oriented interstices in the porous bed and are related to the slit inclination and the slit wall friction factor f_w as (Holub et al., 1992): $E_1=72T^2$ and $E_2=6f_wT^3$.

A z-momentum balance over a liquid film of cross-section thickness Δy bounded by planes z and $z+\Delta z$ in the liquid film (Figs.3.1a,b) yields the following differential equation:

$$\frac{\mathrm{d}^2}{\mathrm{d}y^2}u_{\ell z}(y) = -\frac{1}{\mu_\ell}\left(\rho_\ell g\cos\theta - \frac{\mathrm{d}P}{\mathrm{d}z}\right) \tag{3.14}$$

Subject to the boundary conditions:

- $y = 0$: $u_{\ell z} = 0$ (3.15)
- $y = \delta$: $\frac{\mathrm{d}}{\mathrm{d}y}u_{\ell z}(y) = \frac{f_s(w-\delta)}{\mu_\ell}\left(\rho_g g\cos\theta - \frac{\mathrm{d}P}{\mathrm{d}z}\right)$ (3.16)

Eq.3.15 expresses the non-slip condition at the wall, while Eq.3.16 expresses the shear stress jump at the gas-liquid interface postulated in the Holub et al. model (Holub et al., 1992, 1993). Double integration of Eq.3.14 and insertion of Eqs.3.15, 3.16 give the following velocity distribution in the liquid:

$$u_{\ell z} = \left(\rho_\ell g\cos\theta - \frac{dP}{dz}\right)\frac{\delta^2}{2\mu_\ell}\left[2 - \frac{y}{\delta}\right]\frac{y}{\delta} + \left(\rho_g g\cos\theta - \frac{dP}{dz}\right)\frac{(w-\delta)\delta f_s}{\mu_\ell}\frac{y}{\delta} \tag{3.17}$$

Solution of the slit model in two-phase flow in the trickle bed can be cast as an implicit set of two equations of the pressure drop and the liquid holdup (Holub et al., 1992, 1993):

$$-\frac{\Delta P}{H}+\rho_g g=\rho_g g\frac{\varepsilon^3}{\varepsilon_g^3}\left[E_1\frac{\left(Re_g-f_v\varepsilon_g Re_i\right)}{Ga_g}+E_2\frac{\left(Re_g-f_v\varepsilon_g Re_i\right)^2}{Ga_g}\right] \tag{3.18}$$

$$-\frac{\Delta P}{H}+\rho_\ell g=\rho_\ell g\left\{\frac{\varepsilon^3}{\varepsilon_\ell^3}\left[E_1\frac{Re_\ell}{Ga_\ell}+E_2\frac{Re_\ell^2}{Ga_\ell}\right]-f_s\frac{\varepsilon_g}{\varepsilon_\ell}\left(\frac{\rho_g}{\rho_\ell}-\frac{1}{\rho_\ell g}\frac{\Delta P}{H}\right)\right\} \tag{3.19}$$

Where, similarly to the single-phase flow case:

$$\frac{1}{\cos\theta}\left(-\frac{\mathrm{d}P}{\mathrm{d}z}+\rho_g g\cos\theta\right)=-\frac{\Delta P}{H}+\rho_g g \tag{3.20}$$

$$\frac{1}{\cos\theta}\left(-\frac{\mathrm{d}P}{\mathrm{d}z}+\rho_\ell g\cos\theta\right)=-\frac{\Delta P}{H}+\rho_\ell g \tag{3.21}$$

The collection efficiency Eq.3.6 for the slit model requires knowledge of the liquid film thickness, δ, the elevation Y_c of the point of entry for the limiting trajectory, and the liquid velocity profile. Moreover, the gas and liquid throughputs are systematically verified to coincide with the trickle flow regime using the Larachi et al., 1999 flow regime transition correlation. Solving the trickle-bed model Eqs.3.18, 3.19 yields the liquid holdup and the pressure gradient for given operating conditions. Consequently, the liquid film thickness and the slit pressure gradient, $-\mathrm{d}P/\mathrm{d}z$, are intuited respectively from Eq.3.10 and Eq.3.20. The parabolic velocity distribution in the liquid phase is thus calculated using Eq.3.17. The hydrodynamic state of the slit being completely defined, backward integration of Eq.3.4 is resumed from the slit outlet to inlet to determine the coordinates of the limiting trajectory entry point (Y_c,0). The constants B^+ and D^+ in Eq.3.4 are estimated using an interpolation method Tien 1989. It is worth noting that this procedure is valid only for the calculation of the initial deposition efficiency (Eq.3.6), $\eta^o_{g\ell}$, when bed operation is initiated with clean collectors.

3.2.2 Limiting trajectory and (multilayer) collection efficiency in slit geometry

Once bed plugging has advanced to a point where the collectors' surface is completely covered with fines, filtration becomes driven by interactions of the incoming fines with the previously trapped ones instead of the clean collector-fine interactions. The trajectory equation must take into consideration the fine-fine interactions. The dominant collection mechanism in the slit geometry is assumed to be through interception. Another approximation assumes that the slit geometry does not change during deposition except that the fines are allowed to form a smooth and uniform layer on the slit walls to preserve the one-dimensional flow assumption (Fig.3.1c). The thus formed porous multilayer deposit allows for a secondary flow described as a Brinkman flow inside a permeable wall modified with an effective viscosity. As in the single and two-phase flow cases, the liquid velocity profile and the porous medium model need to be adapted.

The interaction between fines, calculated by the fine-fine London forces is estimated using a Hammaker constant approximated by the theory of Lifschitz (Cushing and Lawler, 1998, Israelachvili, 1985). The new constant is introduced in Eq.3.3 to compute the new value of the London group and in the limiting trajectory Eq.3.4 as well.

3.2.2.1 Trickle flow liquid velocity distribution in the presence of porous multilayer deposit

When a porous layer of fines covers the slit wall, the liquid velocity profile in the film and in the porous multilayer deposit need be calculated. In a strict sense, the slit model must be adapted to include the pressure drop occasioned in the porous multilayer deposit, along with the liquid film and gas flow pressure drop contributions. For the sake of simplicity, the same pressure gradient is assumed to hold along the three zones. As in the monolayer case, the momentum balance Eq.3.14 is still valid for the film flow outside the porous multilayer deposit. Inside the porous multilayer deposit of depth κ (Fig.3.1c), the equation obtained from the z-momentum balance, over a cross-section Δy considering a Brinkman flow with an effective viscosity μ_e, writes as (Kim and Russel, 1985, Martis et al., 1994):

$$\frac{\mathrm{d}^2}{\mathrm{d}y^2} v_{\ell z}(y) - \frac{\mu_\ell}{k_d \mu_e} v_{\ell z}(y) = -\frac{1}{\mu_e}\left(\rho_\ell g \cos\theta - \frac{\mathrm{d}P}{\mathrm{d}z} \right) \tag{3.22}$$

The effective viscosity has been introduced to account for the liquid flow in the porous multilayer layer. For simplicity and due to lack of empirical relationships pertinent to the studied system, μ_e is assumed to obey an Einstein-like structure:

$$\frac{\mu_e}{\mu_\ell} = 1 + 2.5(1-\varepsilon_d) + 5.9(1-\varepsilon_d)^2 \tag{3.23}$$

In Eqs.3.22, 3.23, k_d and ε_d designate, respectively, the permeability and porosity of the porous multilayer deposit.

It can easily be shown that the slit (or bed) porosity ε, following accumulation of a layer of fines equivalent to the local specific deposit σ and porosity ε_d, departs from that of the clean slit (or bed) state of porosity ε_o as follows:

$$\varepsilon(\sigma) = \varepsilon_o - \frac{\sigma}{1-\varepsilon_d} \tag{3.24}$$

As a result of deposition, the void-to-solid volume ratio equivalent to Eq.3.9 thus becomes:

$$\frac{w-\kappa}{S+\kappa} = \frac{\varepsilon(\sigma)}{1-\varepsilon(\sigma)} \tag{3.25}$$

Combining Eqs.3.9, 3.24, 3.25, enables to express the thickness of the porous multilayer deposit as a function of the bed and filtration characteristic variables:

$$\frac{\kappa}{S} = \frac{\sigma}{(1-\varepsilon_o)(1-\varepsilon_d)} \tag{3.26}$$

The boundary conditions in the film and in the porous multilayer deposit are:

- $y = \kappa+\delta$: $u_{\ell z} = u_i$ (3.27)

where the gas-liquid interface velocity u_i can be estimated using one of the several velocity expressions available for the slit models (see for example Iliuta et al. 2002):

$$u_i = \frac{\delta^2}{2\mu_\ell}\left(-\frac{\mathrm{d}P}{\mathrm{d}z} + \rho_\ell g\cos\theta\right) + \frac{\delta(w-\delta)}{\mu_\ell}\left(-\frac{\mathrm{d}P}{\mathrm{d}z} + \rho_g g\cos\theta\right) \tag{3.28}$$

- $y = 0$: $v_{\ell z} = 0$ (3.29)

standing for the absence of slip at the slit wall of liquid creeping flow within porous multilayer deposit.

- $y = \kappa$: $u_{\ell z} = v_{\ell z} = v_i$ and $\mu_e \dfrac{\mathrm{d}v_{\ell z}}{\mathrm{d}y} = \mu_\ell \dfrac{\mathrm{d}u_{\ell z}}{\mathrm{d}y}$ (3.30)

These equalities stand for the velocity and the shear stress continuity conditions at the interface between the liquid-film flow and the liquid creeping flow within the porous multilayer deposit.

Solving the coupled momentum balance equations Eqs.3.14 and 3.22 using the boundary conditions Eqs.3.27-3.30 yields the liquid velocity distributions for the liquid film and the liquid creeping flow inside the porous multilayer deposit, respectively:

$$\begin{aligned} u_{\ell z}(y) = & -\frac{y^2}{2\mu_\ell}\left(\rho_\ell g\cos\theta - \frac{\mathrm{d}P}{\mathrm{d}z}\right) + \frac{y}{2\delta}\left(\frac{\delta(2\kappa+\delta)}{\mu_\ell}\left(\rho_\ell g\cos\theta - \frac{\mathrm{d}P}{\mathrm{d}z}\right) + 2(u_i - v_i)\right) \\ & - \frac{\kappa(\kappa+\delta)}{2\mu_\ell}\left(\rho_\ell g\cos\theta - \frac{\mathrm{d}P}{\mathrm{d}z}\right) - \frac{\kappa}{\delta}(u_i - v_i) + v_i \end{aligned} \tag{3.31}$$

$$\begin{aligned} v_{\ell z}(y) = & \frac{k_d}{\mu_\ell}\left(\rho_\ell g\cos\theta - \frac{\mathrm{d}P}{\mathrm{d}z}\right) + \frac{k_d\mu_e}{\mu_\ell\left(e^{2\kappa\sqrt{\frac{\mu_\ell}{k_d\mu_e}}} - 1\right)} \times \\ & \left\{ e^{y\sqrt{\frac{\mu_\ell}{k_d\mu_e}}}\left(\frac{1}{\mu_e}\left(\rho_\ell g\cos\theta - \frac{\mathrm{d}P}{\mathrm{d}z}\right)\left(1 - e^{\kappa\sqrt{\frac{\mu_\ell}{k_d\mu_e}}}\right) + \frac{v_i\mu_\ell}{k_d\mu_e}e^{\kappa\sqrt{\frac{\mu_\ell}{k_d\mu_e}}}\right) \right. \\ & \left. + e^{(\kappa - y)\sqrt{\frac{\mu_\ell}{k_d\mu_e}}}\left(\frac{1}{\mu_e}\left(\rho_\ell g\cos\theta - \frac{\mathrm{d}P}{\mathrm{d}z}\right)\left(1 - e^{\kappa\sqrt{\frac{\mu_\ell}{k_d\mu_e}}}\right) - \frac{v_i\mu_\ell}{k_d\mu_e}\right)\right\} \end{aligned} \tag{3.32}$$

Substitution into Eq.3.32 of the shear stresses equality at $y = \kappa$ yields the interfacial velocity v_i:

$$\begin{aligned} v_i = & -\frac{1}{2\frac{\mu_\ell^2}{k_d\mu_e}\left(1 - e^{-2\kappa\sqrt{\frac{\mu_\ell}{k_d\mu_e}}}\right) + 2\mu_e\delta\left(\frac{\mu_\ell}{k_d\mu_e}\right)^{\frac{3}{2}}\left(1 + e^{-2\kappa\sqrt{\frac{\mu_\ell}{k_d\mu_e}}}\right)} \times \\ & \left\{ \frac{\mu_\ell^2}{k_d\mu_e}\left(1 - e^{-2\kappa\sqrt{\frac{\mu_\ell}{k_d\mu_e}}}\right)\left(2u_i - \frac{\delta^2}{\mu_\ell}\left(\rho_\ell g\cos\theta - \frac{\mathrm{d}P}{\mathrm{d}z}\right)\right) \right. \\ & \left. - 2\delta\left(\rho_\ell g\cos\theta - \frac{\mathrm{d}P}{\mathrm{d}z}\right)\sqrt{\frac{\mu_\ell}{k_d\mu_e}}\left(1 - 2e^{-\kappa\sqrt{\frac{\mu_\ell}{k_d\mu_e}}} + e^{-2\kappa\sqrt{\frac{\mu_\ell}{k_d\mu_e}}}\right)\right\} \end{aligned} \tag{3.33}$$

The fractional liquid flow rates splitting in the porous multilayer deposit and in the film, as well as the total flow rate are, respectively:

$$Q_{layer} = \int_0^{\kappa} v_{\ell z}(y)\mathrm{d}y\,;\; Q_{film} = \int_{\kappa}^{\kappa+\delta} u_{\ell z}(y)\mathrm{d}y\,;\; Q = Q_{layer} + Q_{film} \tag{3.34}$$

Eq.3.6 is used to obtain the multilayer collection efficiency after solving the trajectory equation Eq.3.4 and the velocity profile Eq.3.31, and accounting for the fine-fine interaction in the Hammaker constant. Backward integration of Eq.3.4 is started at $z=L$ and $y=a_p+\kappa$ and halted when reaching the slit entrance point at $y=\kappa+Y_c$ and $z=0$. Also it is important to evaluate the fractional liquid flow rate in the porous multilayer deposit (Eq.3.34) as the fines fraction conveyed by this fluid is considered as collected. In those instances, similarly to Eq.3.5, the new expression for the non-Brownian collection efficiency in the presence of the porous multilayer deposit is computed as:

$$\eta^{nB} = \frac{\int_{\kappa+a_p}^{\kappa+Y_c} u_{\ell z}(y)\mathrm{d}y + \int_{a_p}^{\kappa} v_{\ell z}(y)\mathrm{d}y}{\int_{\kappa}^{\kappa+\delta-a_p} u_{\ell z}(y)\mathrm{d}y + \int_0^{\kappa-a_p} v_{\ell z}(y)\mathrm{d}y} \tag{3.35}$$

To obtain a practical explicit numerical correlation for the multilayer collection of fines in two-phase flow from Eqs.3.6, 3.35, an approach inspired from the work of Choo and Tien, 1995 is used. In this approach, the ratios between the collection efficiencies (or filtration coefficients) under multilayer and monolayer conditions for two-phase flow are expressed as a weighted average of the limiting cases of an impermeable layer (k_d=0) and an infinitely permeable layer ($k_d\rightarrow\infty$) as follows:

$$\frac{\eta_{g\ell}}{\eta_{g\ell}^o} = \frac{\lambda_{g\ell}}{\lambda_{g\ell}^o} = \zeta \left.\frac{\lambda_{g\ell}}{\lambda_{g\ell}^o}\right|_{k_d=0} + (1-\zeta)\left.\frac{\lambda_{g\ell}}{\lambda_{g\ell}^o}\right|_{k_d\rightarrow\infty} \tag{3.36}$$

The two limiting collection efficiencies (or filter coefficients) must be obtained; one in which k_d=0, *i.e.*, no liquid flow is allowed inside the porous layer, and another one when $k_d\rightarrow\infty$ for both the monolayer ($\lambda^o_{g\ell}$, $\eta^o_{g\ell}$) and the multilayer ($\lambda_{g\ell}$, $\eta_{g\ell}$) cases. The weighting factor ζ is calculated fitting an approximate expression structurally similar to that given by Choo and Tien, 1995.

3.2.3 Transport equations for filtration at trickle bed scale

An Euler *k*-fluid, two-dimensional, unsteady-state computational fluid dynamic (CFD) model is formulated to describe the space-time evolution of fines accumulation and the resulting build-up of pressure drop as a function of the average specific deposit under two-phase flow conditions. After setting the Lagrangian methodology to model the monolayer and multilayer collection efficiencies using the slit analogy, multiphase flow simulations of filtration are conducted at the trickle-bed reactor scale using the Los Alamos CFDlib multiphase flow simulation library (Kashiwa et al., 1994a, 1994b). The ensemble-averaged Euler *k*-fluid multi-material formalism is used to integrate over finite control volumes (or grid cells) representing the computational grid, the time-dependent gas and liquid conservation equations. For details about the CFDlib numerical schemes, several references from the Los Alamos group can be consulted (Kashiwa et al., 1994a, 1994b, Padial et al. 2000).

The liquid/fine/gas/porous medium multiphase system representing the filtration problem is treated as a system of three interpenetrating continuum phases: i) a dilute liquid phase consisting of the liquid embracing fines present at tiny volume fractions in the incoming stream, ii) a pseudo-continuous solid phase made up of the packing particles (or collectors) of the porous bed along with the fines being attached to their surface due to capture, iii) and an ideal and incompressible gas phase. The three phases within each finite control volume of the computational domain are assumed to have ensemble-averaged volume fractions which, due to plugging by fines, evolve in time. To ensure resolution and convergence the grid cells should be specified of such a size to be sufficiently small in comparison of the dimensions of the bed to assume constancy at the cell level of volume fractions, velocity, pressure, or any advected scalar or vector (Kashiwa, 1994a).

To perform the flow field simulations, the packed bed was discretized in a r-z framework into cells by assigning at every grid point $\underline{\mathbf{a}}$ in the computational domain, a cell volume $v(\underline{\boldsymbol{a}})$ and an initial local porosity $\varepsilon_o(\underline{\boldsymbol{a}})$. The local voidage per cell is obtained by means of a simple simulation program that assigns porosity values randomly by using a normal Gaussian probability density function around the prescribed mean bed porosity (Jiang et al., 2001).

The following assumptions are inherent to the proposed formulation:

- The liquid suspension physical properties are unaffected by the presence of fines,
- The density of the packing is not affected by the collected mass of fines, i.e., dilute solid phase,
- No re-entrainment of deposited fines is allowed, and bed plugging through *sieving effect* and *blocking mode* (Tien, 1989) is ignored;
- The coupling between the gas, liquid and solid phases is handled through the use of the fines filter equation (Eq.3.42) and the interaction drag or momentum exchange force terms (Eqs.3.45, 3.49).

The conservation equations of volume, mass, momentum and species (i.e., the fines) are provided in the form of the Euler-Euler formulation. These equations consist of the conservation of volume, the continuity and the Navier-Stokes equations for the gas and liquid phases, a continuity equation for the solid stationary phase and a species balance equation for the fines being displaced from the liquid phase to the solid phase.

<u>Conservation of volume</u>

$$\varepsilon_g + \varepsilon_\ell = \varepsilon \tag{3.37}$$

<u>Continuity equation for the gas and liquid phases</u>

$$\frac{\partial}{\partial t}\varepsilon_g \rho_g + \nabla \bullet \varepsilon_g \rho_g \underline{\boldsymbol{u}}_g = 0 \tag{3.38}$$

$$\frac{\partial}{\partial t}\varepsilon_\ell \rho_\ell + \nabla \bullet \varepsilon_\ell \rho_\ell \underline{\boldsymbol{u}}_\ell + \rho_f N = 0 \tag{3.39}$$

<u>Continuity equation for the solid phase</u>

$$\frac{\partial}{\partial t}(1-\varepsilon)\rho_s = \rho_f N \tag{3.40}$$

<u>Species balance equation for the fines</u>

$$\frac{\partial}{\partial t}\varepsilon_\ell c + \nabla \bullet \varepsilon_\ell c \underline{\boldsymbol{u}}_\ell + N = 0 \tag{3.41}$$

The filtration rate *N* in Eqs.3.40-3.42 is calculated by the Iwasaki, 1937 logarithmic equation:

$$N = \lambda c \left\| \underline{\boldsymbol{u}}_\ell \right\| \tag{3.42}$$

This phenomenological equation ties the fines concentration in the liquid suspension and the local liquid velocity to the filtration rate. Similarly, to the numerical simulations of single-phase flow filtration presented in Ortiz-Arroyo et al. 2002, it is assumed that the Iwasaki equation is symbolically preserved at the grid cell level so that the per-cell filtration rate is proportional to the local concentration and the interstitial liquid velocity. Furthermore, it is also assumed to be valid under two-phase flow conditions.

In Eq.3.42, λ is the filter coefficient, which can be thought of as the probability for a fine to be captured as it travels a unit distance through the bed (Tien, 1989). The form of the filter coefficient is dictated by the nature of the capture phenomena in play, and by the amount of capture as bed plugging evolves.

The relationship between the filtration coefficient and the slit-based collection efficiency is considered to be the same as for the capillary model (Tien, 1989):

$$\lambda = \sqrt[3]{\frac{6(1-\varepsilon)}{\pi}}\,\frac{\eta}{d_c} \tag{3.43}$$

In Eq.3.43, η is either the monolayer collection efficiency $\eta^{o}_{g\ell}$ calculated in section 3.3.1 or the multilayer collection efficiency $\eta_{g\ell}$ calculated in section 3.3.2. They have been simulated off the CFDlib code by solving Eq.3.4 for different conditions. Then empirical fitting numerical correlations such as Eq.3.57-3.60 are embedded in the CFDlib code.

Momentum balance equation for the gas and liquid phases

$$\frac{\partial}{\partial t}\varepsilon_i\rho_i\underline{\boldsymbol{u}}_i + \nabla\bullet\varepsilon_i\rho_i\underline{\boldsymbol{u}}_i\otimes\underline{\boldsymbol{u}}_i = -\varepsilon_i\underline{\nabla}P + \varepsilon_i\rho_i\underline{\boldsymbol{g}} + \nabla\bullet\mu_i\varepsilon_i\left(\nabla\underline{\boldsymbol{u}}_i + \left[\nabla\underline{\boldsymbol{u}}_i\right]^T\right) + \underline{\boldsymbol{F}}_{i(j,k)} \tag{3.44}$$

It can be noted from Eq.3.44, that the turbulent transport (*via* the Reynolds shear stress) and the net sink for liquid momentum (mass exchange source) due to fines capture have been neglected. In Eq.3.44, $\underline{\boldsymbol{F}}_{i(j,k)}$ represents the momentum exchange vector or drag force between the fluid phase *i*, and either of the fluid phase *j* or the solid phase *k*. At any given point of the computational domain, the momentum exchange vector between two phases can be formulated as the product of the volume fractions of two among the *k* phases, the corresponding momentum exchange rate coefficient X_{ij}, and the local relative velocity between the *k* phases (Kashiwa et al., 1995):

$$\boldsymbol{F}_{ij} = \varepsilon_i\varepsilon_j X_{ij}\left(\boldsymbol{u}_i - \boldsymbol{u}_j\right) \tag{3.45}$$

According to this formalism and using the slit model drag formulations, the gas-solid and the liquid-solid momentum exchange rates take the following expressions Jiang et al., 2002:

$$X_{is} = \frac{A_{is}\mu_i U_i + B_{is}\rho_i U_i^2}{(1-\varepsilon_o)|u_i|} \tag{3.46}$$

$$A_{is} = \frac{E_1(1-\varepsilon_o)^2}{\varepsilon_i^3 d_p^2};\; B_{is} = \frac{E_2(1-\varepsilon_o)}{\varepsilon_i^3 d_p} \tag{3.47}$$

In these expressions, the relationship between superficial velocity U_i and interstitial velocity u_i is:

$$u_i = \frac{U_i}{\varepsilon_i} \tag{3.48}$$

Contrarily to the drag expressions previously used in the one-dimensional filtration model of Iliuta et al., 2003, the interaction force between the gas and liquid phases was neglected for simplicity in the present treatment. This simplification remains acceptable as long as the fluids' throughputs and the operating pressure ensure that flow regime is trickle flow with low gas-liquid interaction. Otherwise, there will be no particular difficulty to account for all the fluid-fluid and fluid-solid interactions in a more comprehensive set of drag forces such as those proposed by Iliuta et al., 2000 and Attou et al., 1999.

With the progress of plugging, the collectors' surface becomes progressively covered with fines, so that the local packing specific area increases as a function of time with the growing available area of fines being captured. The total specific surface area is calculated by adding to the collector surface area, the surface area of the collected fines that actually contribute to the momentum exchange with the liquid phase (O'melia and Ali, 1978, Ortiz-Arroyo et al., 2002, Iliuta et al., 2003a). The momentum exchange terms are thus modified as:

$$X_{is} = \frac{A_{is}\mu_i U_i + B_{is}\rho_i U_i^2}{(1-\varepsilon)|u_i|} \tag{3.49}$$

$$A_{is} = \frac{E_1 a_{\ell s}^2 (1-\varepsilon)^2}{36\,\varepsilon_i^3}\,;\; B_{is} = \frac{E_2 a_{\ell s}(1-\varepsilon)}{6\,\varepsilon_i^3} \tag{3.50}$$

At every point $\underline{\mathbf{a}}$ of the computational domain, the *instantaneous* specific surface area, expressed per unit *total solid volume in grid cell*, can be summarized in the following compact relationship (Stephan and Chase, 2000, Ortiz-Arroyo et al., 2002, Iliuta et al., 2003a):

$$a_{\ell s}(t,\underline{\boldsymbol{a}}) = \frac{\gamma_c(t,\underline{\boldsymbol{a}})N_c(\underline{\boldsymbol{a}})\pi d_c^2(t,\underline{\boldsymbol{a}}) + N_c(\underline{\boldsymbol{a}})\partial N_f(t,\underline{\boldsymbol{a}})\left[\gamma_f \pi d_f^2 - A_\Delta(t,\underline{\boldsymbol{a}})\right]}{N_c(\underline{\boldsymbol{a}})\frac{\pi}{6}d_{co}^3 + N_f(t,\underline{\boldsymbol{a}})\frac{\pi}{6}d_f^3} \tag{3.51}$$

The first term in Eq.3.51 numerator reflects the area contributed by the collectors whereas the second term, the area contributed by the fines. Since not all the geometrical area of the collectors and the deposited fines is available for momentum transfer, geometrical correction parameters γ_f and $\gamma_c(t,\underline{\boldsymbol{a}})$ are introduced to account for the peripheral areas effectively involved in interception (Stephan and Chase, 2000, Ortiz-Arroyo et al., 2002, Iliuta et al., 2003a).

$N_c(\underline{\boldsymbol{a}})$ and $N_f(\mathrm{t},\underline{\boldsymbol{a}})$ are, respectively, the number of collectors and the number of captured fines in a computational cell of volume $v(\underline{\boldsymbol{a}})$:

$$N_c(\underline{\mathbf{a}}) = \frac{6v(\underline{\mathbf{a}})}{\pi d_{c0}^3}(1-\varepsilon_o(\underline{\mathbf{a}})) \tag{3.52}$$

$$N_f(t,\underline{\boldsymbol{a}}) = \frac{6v(\underline{\boldsymbol{a}})}{\pi d_f^3}(\varepsilon_o(\underline{\boldsymbol{a}}) - \varepsilon(t,\underline{\boldsymbol{a}}))(1-\varepsilon_d) \tag{3.53}$$

$\partial N_f(t,\underline{\boldsymbol{a}})$ represents the number of fines, per collector, that culminate at the periphery of the collector + deposit assemblage at time t (see Ortiz-Arroyo et al., 2002 for details):

$$\partial N_f(t,\underline{\boldsymbol{a}}) = 4\gamma_c(t,\underline{\boldsymbol{a}})(1-\varepsilon_d)\left[\frac{d_c(t,\underline{\boldsymbol{a}})}{d_f}\right]^2 \tag{3.54}$$

The collector area loss, A_Δ, occasioned by the shadow effect (Tien and Payatakes, 1979) per attached fine is estimated from the shadow left by an equilateral triangle in which the fine is inscribed (Stephan and Chase, 2000):

$$A_\Delta(t,\underline{\boldsymbol{a}}) = \frac{d_c^2(t,\underline{\boldsymbol{a}})}{8}\left[2\sqrt{3}\frac{d_f}{d_c(t,\underline{\boldsymbol{a}})} - \sin\left(2\sqrt{3}\frac{d_f}{d_c(t,\underline{\boldsymbol{a}})}\right)\right] \tag{3.55}$$

To account for the growth of the deposit on the collector surface, the increase in the collector diameter is calculated as a function of the smooth specific deposit (Choo and Tien, 1995):

$$\frac{d_c(t,\underline{\boldsymbol{a}})}{d_c^o} = \sqrt[3]{1 + \frac{\sigma(t,\underline{\boldsymbol{a}})}{(1-\varepsilon_d)(1-\varepsilon_o(\underline{\boldsymbol{a}}))}} \tag{3.56}$$

In the above expressions of the momentum exchange terms, it is assumed that the permeability drop off due to fines accumulation is conveyed strictly through increased local specific surface area and through decreased local porosity within each computational cell. Strictly speaking, however, this representation of the plugging behavior in the packed bed is still incomplete because the permanent modulation of local bed tortuosity with the progress of plugging has not been accounted for in the present analysis. Porous medium tectonics due to deposition indeed strongly depends on the history of collection which in turn must be a complex function of the non-steady state two-phase flow. As a result bed tortuosity may evolve in time because of the peculiarity of the medium being formed of entities differing in sizes, i.e., collectors and fines. For instance, findings by Mota et al., 1999 show that permeability is a function of the packing procedure of entities differing in size, which renders as a matter of fact, use of invariant E_1 and E_2 constants illusory. Despite this limitation, we have assumed that changes due to fines buildup in bed tortuosity and thus E_1 and E_2 constants are negligible. Further refinements of the deep bed filtration model could account for a more rigorous bed tectonics model for tracking the fate of tortuosity.

The simple cylindrical geometry of the bed suggests using a single-block computational mesh of a structured type in the CFDlib finite volume solver with explicit temporal differencing (Padial et al., 2000). The boundary conditions for the liquid and gas are of four types: specified inflow, conserving outflow, centerline symmetry, and reflective-wall (or free-slip wall) condition. Liquid velocities and fines concentration are specified as inlet boundary conditions. Outflow boundary condition to ensure mass conservation of the liquid and gas is specified at the bottom of the column. At the vessel vertical boundaries, a free-slip wall condition is imposed. Transient simulations of *clean* bed gas-liquid flow are run until the flow fields reach steady state. Under these circumstances, the conservation equations are solved in the absence of fines in the liquid. Transient simulations with fines-containing liquid are then resumed by solving the whole set of equations.

3.3 Results and Discussion

3.3.1 Monolayer collection efficiency in slit geometry

Several series of trajectory simulations in single-phase flow have been performed using the trajectory equation (Eq.3.4) for the following ranges of bed porosity, gravitational, interception and London dimensionless groups, respectively, $0.32 \leq \varepsilon_o \leq 0.44$; $0.16 \leq N_G \leq 0.22$; $10^{-3} \leq N_R \leq 10^{-2}$; $3 \cdot 10^{-5} \leq N_{Lo} \leq 3 \cdot 10^{-4}$. The fine diameters ranged between 0.1 and 10 μm, and the collector diameters between 1 and 3 mm. The non-Brownian collection efficiencies calculated from Eq.3.5 for the slit geometry have been benchmarked using the numerical collection efficiency correlation of Rajagopalan and Tien, 1976 developed for the sphere-in-cell model.

Fig.3.2 illustrates the behavior of typical trajectory calculations in the slit model where the single-phase flow monolayer collection efficiency η^o is plotted as a function of the interception number for different values of the London dimensionless group and fine diameters in the [1-10 μm] range. The simulations used liquid velocity values which correspond to the trickle flow regime which will be simulated later using the *k*-fluid approach detailed in §3.2.3. In the explored ranges of variables, the trends exhibited by the η^o vs. N_R and N_{Lo} groups (solid lines) are comparable to those predicted with the numerical correlation (dashed lines) of Rajagopalan and Tien, 1976. Note that the slight overestimation of collection efficiencies by the latter correlation is ascribed to the sphere-in-cell formulation which differs from the capillary model (Payatakes et al., 1974). The smooth trends shown in the figure indicate that the trajectory equation reflects quantitatively and qualitatively the single-phase collection behavior and that the London forces effect is properly handled by the integration algorithm.

Further numerical experiments have been performed for two-phase flow using the same dimensionless groups, porosity, collector and fine diameters as in the simulations above, in addition to a gas Reynolds number, Re_g. The gas superficial velocity has been varied between 10^{-4} and 0.5 m/s, and the liquid holdup resulting from the solution of the Holub et al., 1992 model (Eqs.3.18-3.21) for clean collectors varied between 0.11 and 0.22. The liquid viscosity and density have been maintained in the limits of representative petroleum-like and refinery processing liquids.

Based on the simulations from the trajectory equation in two-phase flow over the ranges swept by the variables, a computationally-friendly numerical correlation has been derived for the monolayer collection efficiency which is expressed as a function of the single-phase monolayer collection efficiency, η^o, the gas Reynolds number, the liquid holdup and the porosity in the slit as follows:

$$\eta_{g\ell}^o = 1.28\left(\eta^o\right)^{0.83}\left(\frac{\varepsilon_\ell}{\varepsilon_o}\right)^{1.43}\left(1 - 0.31 Re_g^{0.22}\right) + \eta^B \tag{3.57}$$

Note that Eq.3.57 does not yield in the asymptotic limit, the single-phase collection efficiency, η^o, as zero gas throughput in downward trickle flow stands for stagnant gas with $\varepsilon_\ell < \varepsilon^o$, and not for flooded bed state ($\varepsilon_\ell = \varepsilon^o$).

Eq.3.57 indicates that in trickle flow, the two-phase monolayer collection efficiency increases with increasing the liquid holdup and decreases with increasing the gas Reynolds number (or gas throughput). Fig.3.3, showing simulations for [1-10 μm] fines, confirms indeed that monolayer collection efficiencies in two-phase flow are smaller than their single-phase counterparts, everything else being identical. In addition with increasing gas velocity, the collection efficiencies undergo a decreasing trend. It is plausible that stiffer liquid velocity gradients at the slit wall in two-phase flow due to the shearing action of the gas flow in the slit core might be responsible for the less interceptive collectors in comparison with the single-phase flow situation. Increased gas velocities are indeed tantamount to decreasing liquid holdups which combined with the negative coefficient of Re_g in Eq.3.57 strengthen the decrease of the two-phase collection efficiency.

The simulations shown in Fig.3.3 predict either a minimum or a plateau region for the collection efficiency as function of the interception group N_R for any given gas velocity. This feature can be taken advantage of when searching for optimum conditions in terms of collector size and operating conditions for preventing deposition of fines. For example, higher gas velocities combined with N_R values larger than $5 \cdot 10^{-4}$ would keep at minimum the deposition for the conditions shown in Fig.3.3.

The effect of liquid holdup on the two-phase flow collection efficiency is illustrated in Fig.3.4 for various gas throughputs and increasing liquid throughputs in the slit. In principle, trajectory analysis in single-phase flow is unable to answer this issue as the liquid fills the whole porosity space in classical deep bed filtration. For a given constant gas throughput, $\eta^{o}_{g\ell}$ decreases with increasing liquid throughput and liquid holdup in the slit. Increasing liquid holdup has a tendency to increase collection of fines as suggested by the liquid holdup dependence in Eq.3.57. Higher amounts of fines flowing inside the porous bed mean as a matter of fact higher probabilities of deposition. *A contrario*, increasing liquid velocity has a tendency to retard collection of fines. The net outcome seems to be dictated by this latter factor rather than by the increased amount of fines with liquid holdup.

3.3.2 Multilayer collection efficiency in slit geometry

Plugging evolves smoothly from a monolayer capture mechanism driven by clean collector-fine interactions to a multilayer mechanism (ripening stage) prompted by fine-fine interactions. Once the filter operates in the ripening stage, capture by the porous multilayer deposit topping the collector must be taken into account. Using the collection model depicted in §3.2.2.1, a series of explicit numerical correlations derived from the trajectory analysis of Eq.3.4 can be established. The ratios between the collection efficiencies (or filter coefficients) under multilayer and monolayer conditions for two-phase flow are expressed as a weighted average of the limiting cases of an impermeable porous multilayer deposit (k_d=0) and an infinitely permeable porous multilayer deposit ($k_d \rightarrow \infty$) as follows:

When k_d=0, the multilayer collection efficiency (or filter coefficient) correlation in two-phase flow writes as:

$$\left.\frac{\eta_{g\ell}}{\eta_{g\ell}^{o}}\right|_{k_d=0} = \left.\frac{\lambda_{g\ell}}{\lambda_{g\ell}^{o}}\right|_{k_d=0} = 1 + \frac{\sigma(1-\varepsilon_o)^{0.11}}{1-\varepsilon_d} \tag{3.58}$$

Similarly, when $k_d \to \infty$, collector efficiencies (or filter coefficients) are calculated using the clean velocity profile by varying the width of the slit after accounting for the depth κ of the deposit layer with the slit half thickness S. With this approach, the new expression arrived at is:

$$\left.\frac{\eta_{g\ell}}{\eta_{g\ell}^{o}}\right|_{k_d\to\infty} = \left.\frac{\lambda_{g\ell}}{\lambda_{g\ell}^{o}}\right|_{k_d\to\infty} = 1 + 0.96\left(\frac{\sigma}{1-\varepsilon_d}\right)^{0.579} \tag{3.59}$$

For the general case where the permeability is between these asymptotic limits, the weighting factor ζ is assumed to follow a form given in Choo and Tien, 1995:

$$\zeta = \frac{0.234k_d(1-\varepsilon_o)^{-2}\left(1+\dfrac{0.0128}{N_R}\right)\left(\dfrac{\sigma}{5(1-\varepsilon_d)}\right)^{1.13+\frac{0.2\times10^{-4}}{N_R}}}{1+0.834k_d(1-\varepsilon_o)^{-2}\left(1+\dfrac{0.0128}{N_R}\right)\left(\dfrac{\sigma}{5(1-\varepsilon_d)}\right)^{1.01+\frac{0.5\times10^{-4}}{N_R}}} \tag{3.60}$$

As the permeability of the porous multilayer deposit increases, less resistance is experienced during the flight of the liquid. This allows more liquid to easily engulf inside the porous layer. Moreover, during a time increment, the differential fraction of liquid entering the porous layer has necessarily lost the fines being carried by in the previous instant. The fines get captured and deposited over the porous multilayer deposit. This feature explains the increasingly multilayer two-phase collection efficiencies with increasing deposit permeabilities as bed switches to the ripening stage. Figs.3.5, 3.6 illustrates the increment of filter coefficient (and collection efficiency) ratios for a range of permeability and deposit porosity values. Fig.3.7 depicts a typical variation of the collection efficiency (or filter coefficient) ratio as a function of the specific deposit and the interception number.

3.3.3 Validation of the trickle-bed filtration model

Validation of the Euler *k*-fluid model is based on the two-phase pressure drop measurements of Gray et al., 2002 during trickle bed plugging. Ambient plugging tests (room temperature and atmospheric pressure) were run using kerosene as the liquid phase (seeded with kaolinite fines of 0.7 μm) and air as the gas phase flowing through a column of 0.9 m height and 3.8 cm of internal diameter. Trilobe (Ni+Mo on γ-alumina) 1.6×3.6 mm in diameter and 4-mm spherical (γ-alumina) catalytic particles were used as collectors. The experimental conditions are listed in Table 1. In their experiments, the pressure drop in trickle and pulse flow regimes was found to vary linearly as a function of the specific deposit. Apparently, the shape of the collector is a key factor that differentiates the behavior of the pressure drop of the bed in trickle flow, giving lower pressure drops for the trilobe than for the spherical catalysts. Gray et al., 2002 concluded that the reduction of the porosity from the initial porosity due to deposited fines can explain the pressure build up in the bed.

Figs.3.8a,b illustrate the increase of two-phase pressure drops as a function of time under filtration conditions as predicted using the present Euler *k*-fluid model for the spherical and trilobe catalysts in trickle flow regime. The transient bed response of the experimental pressure drops reported by Gray et al., 2002 for the same conditions is also shown for comparison. Two types of simulations have been carried out under the assumptions: i) filtration evolves under monolayer conditions regardless of time and location in the bed, ii) after a certain time, filtration switches from monolayer to multilayer deposition when the local specific deposit exceeds the critical specific deposit (Ortiz-Arroyo et al., 2002) which is required for completion of a monolayer of fines around the collectors.

Under both assumptions, the fitting capability of the model is acceptable for the initial portion of the graph where presumably the rise in pressure gradient is controlled by monolayer interactions. However, when plugging becomes relatively severe around 300-400 minutes, the experimental pressure drop profile is bracketed between the simulations of the monolayer scenario and that where a shift towards multilayer deposition is allowed. The pressure drop measurements are systematically over-predicted by the multilayer simulations suggesting that the collection efficiencies determined from the slit model may not be universally applicable with an invariant set of geometric parameters. Among the reasons that could be advanced to explain this divergence is the fact that the same assortment of Ergun constants (constant tortuosity) is used regardless of the location of the computational cells in the bed. There is no reason, nonetheless, that under multilayer deposition conditions, the Ergun constants will not evolve as a function of specific deposit. The time invariance of the multilayer deposit porosity and permeability is another factor that is difficult to ascertain. It is plausible that with the progress of deposition, the reduced space left for the liquid flow, thereby increasing the liquid interstitial velocity, would impose time-varying compressive constraints on the deposit. Such compression would result in thinner deposits than predicted with constant k_d and ε_d parameters, yielding, overall lesser obstruction and therefore a lower pressure drop rise. Another promising approach to explore in further numerical investigations of deposition in two-phase flow porous media could be the lattice-gas automata approach recently published by Biggs, Tüzün and coworkers, 2003. This approach has the merit of solving the fines trajectories when suspended fines as well as developing deposits affect in non-weak conditions the flow fields in the porous medium, contrarily to the conventional trajectory analyses such as the one used in this work.

Axisymmetrical contour plots of the local specific deposit (Eq.3.24) and local total solids volume fraction are illustrated in Fig.3.9 for the bed packed with spherical catalyst as three snapshots at t=0, 180 and 480 min. In qualitative agreement with the observations of Gray et al., 2002, in the early collection process and up to 300 min, the fines appear to be distributed relatively evenly along the bed with very small values of local specific deposit. As time evolves, a plugging front appears and starts to progressively fill up the column. For the simulated time range, plugging is more confined in the entrance region of the bed. The bed appears to undergo more inhomogeneous plugging with sharper contrasts in the specific deposits between the entrance and the exit regions. This suggests that the multilayer collection mechanism is more active in the upper bed portion whereas the monolayer mechanism prevails in the bed lower portion. Shift from monolayer to multilayer deposition explains the change in trend of the pressure drop curve that took place around 300-400 min of bed operation, see Figs.3.8a,b. It is clear from the simulations that the rise of pressure drop with plugging is determined by both surface and volumetric phenomena. As the monolayer collection mechanism is unable to bring about significant drop off in bed porosity, it is likely that the incremental surface of fines that are captured by the collectors contribute via drag and specific surface area (Eq.3.51) to raise the pressure drop. Multilayer collection on the other hand may induce significant reduction of the local porosity thereby rising the pressure drop due to the narrowing of space left to the gas-liquid flow, besides the increased drag and specific surface area. However, to prove whether these contentions are valid or not, it is necessary to carry out further experimental studies capable of unveiling the internal structure of the trickle bed during filtration.

3.4 Concluding remarks

A gap between conventional deep-bed filtration in single-phase flows and filtration in gas-liquid flows in trickle-bed reactors has been filled with the proposition of a new Lagrange-Euler-Euler computational fluid dynamics framework. The approach revolves around the development of an ad-hoc trajectory analysis model using the inclined slit geometry model to establish the relationships required for the collection efficiency and the filter coefficient for monolayer and multilayer depositions in single-phase and two-phase flow conditions. For this purpose, formulations based on the Holub slit model and combined slit-Brinkman flow models were used. These slit-based expressions were established for non-polar and non-electrolytic petroleum-like liquids where there is a need in the refining industry to model deep-bed filtration in multiphase flow. They were correlated in terms of London, gravitational, interception, and gas Reynolds numbers, liquid holdup, specific deposit, and deposit permeability and porosity for fines encompassing the colloidal and the non-colloidal range up to 10 microns. The slit-based collection efficiencies and filter coefficients were fed to an Euler *k*-fluid unsteady state two-dimensional axisymmetrical CFD model to describe the evolution of two-phase pressure drop as a function of time. The model outputs showed acceptable agreement, especially during the first stages of collection, when compared with experimental pressure drop data for systems akin to those encountered in the petroleum refining industry. The model was also able to procure maps of time and space distributions of the specific deposit and the bed porosity. Future work on the subject can include experimental verification of the plugging structure in multiphase flow and refinements of the multilayer deposition model, for example by allowing evolution of the geometrical properties of the deposits in the bed (e.g., tortuosity, Ergun constants). Other refinements can include:

1. Instead of the presented global pressure drop validations, comparisons between measured and predicted local pressure gradient (or permeability).
2. Extension of the simulation times well over the 10^2 - 10^3 minutes range to approach several months time horizons reminiscent of the true actual hydrotreating time scale operation.
3. Modeling of fines re-entrainment/re-deposition via aggregate migration adapting approaches similar to those proposed by Payatakes, 1981, 2001 for the context of viscous oil flows and high shear stress in two-phase flows.
4. Modeling fines migration and buildup at the gas-liquid interface and the points of contacts between collectors (static liquid holdup).

Acknowledgements

The Los Alamos National Laboratory is acknowledged for giving us access to the CFDLIB library of codes. Arturo Ortiz Arroyo would like to acknowledge the financial support of CONACyT México and the Universidad Autónoma de Tlaxcala, México. Financial support from the Natural Sciences & Engineering Research Council of Canada is also acknowledged. Professor Chi Tien is acknowledged for his valuable comments and suggestions.

Nomenclature

$a_{\ell s}$	bed specific surface area, m^{-1}
a_p	fine radius, m
A_{Δ}	shadow area loss, m^{2}
A_{is}	laminar term in momentum exchange
B^{+}	constant
B_{is}	inertial term momentum exchange
c	fine volumetric concentration (liquid volume basis), –
c_s	Cunningham correction factor
D^{+}	constant
$d_{p,c,f}$	particulate effective diameter (collector or fine), m
D_B	Brownian diffusion coefficient, m^{2}/s
E_1, E_2	Ergun constants, –
f_s	slit model shear stress jump function, –
f_v	slit model velocity jump function, –
F_{ij}	drag force between phases i and j, N/m^{3}
$F_i(\delta^{+})$	Universal functions of the fine-collector dimensionless distance, δ^{+}
g	gravitational acceleration, m/s^{2}
Ga_{α}	α-phase Galileo number, –
Ha	Hammaker constant, J
H	Bed height, m

k	Boltzmann constant, J/K
k_d	permeability of the deposit layer, m^2
L	slit length, m
N	filtration rate (reactor volume basis), s^{-1}
N_c	number of collectors in computational cell volume $\boldsymbol{v}$, –
N_f	number of trapped fines in computational cell volume $\boldsymbol{v}$, –
∂N_f	number of peripheral fines per collector, –
N_G	gravitational dimensionless group
N_{Lo}	London-van der Waals dimensionless group
N_R	interception dimensionless group
P	pressure, Pa
Re_α	α-phase Reynolds number, –
S	slit half wall thickness, m
T	Temperature, K
$u_{\ell z}(y)$	liquid velocity profile in slit, m/s
u_α	average interstitial velocity of α-fluid, m/s
u_i	gas-liquid interfacial velocity, m/s
U_α	average superficial velocity of α-phase, m/s
$\boldsymbol{v}$	computational cell volume, m^3
v_i	liquid-deposit layer interfacial velocity, m/s
$\mathrm{v}_{\ell z}(\mathrm{y})$	liquid velocity profile in the porous layer, m/s
w	half void thickness, m
X_{ij}	momentum exchange term between phases i and j, -
y	crosswise coordinate measured from wall, m
Y_c	coordinate of the trajectory at slit inlet, i.e., $z=0$
z	streamwise coordinate measured from slit entrance, m

Greek Letters

α_{sp}	retardation factor, –
δ^*	fine-collector distance, m
δ^+	fine-collector distance dimensionless, –
δ	liquid film thickness, m

ε	slit, local bed porosity, –
ε_{α}	α-phase holdup,–
ε_{d}	porosity of the deposit layer,–
γ_{f}	fine cross-section fraction, –
γ_{c}	collector cross-section fraction, –
η	collector efficiency, –
$\eta_{g\ell}$	two-phase collection efficiency, –
λ	filter coefficient, m^{-1}
μ_{α}	α phase dynamic viscosity, kg/m·s
μ_{e}	effective viscosity , kg/m·s
κ	thickness of the porous multilayer deposit
θ	inclination angle of the slit
ρ_{α}	density of α phase, kg/m^3
σ	specific deposit (reactor volume basis), –
ζ	weighting factor in Eq.36

Subscripts/Superscripts

B	Brownian
c	collector
f	fine
g	gas
ℓ	liquid
nB	non-Brownian
o	clean bed state, monolayer
s	solid

References

Attou A. and Ferschneider G. (1999) A simple model for pressure drop and liquid hold-up in packed-bed bubble reactors.*Chem. Eng. Sci.* **54**, 5139.

Bauquis P.R. (2002) A reappraisal of energy supply and demand in 2050. The Institute of Energy Economics, Japan, July, (http://eneken.ieej.or.jp/en/outlook/).

Biggs M.J., Humby S.J., Buts A. and Tüzün U. (2003) Explicit numerical simulation of suspension flow with deposition in porous media: influence of local flow field variation on deposition processes predicted by trajectory methods, *Chem. Eng. Sci.* **58**, 1271.

Brossard D.N. (1996) *Chevron RDS/VRDS hydrotreating-Transportation fuels from bottom of the barrel*. In R.A. Meyers (Ed.), *Handbook of petroleum refining processes*, 2nd edition, McGraw-Hill, NY, USA, Chapter 8.1.

Burganos V.N., Paraskeva C.A. and Payatakes A.C. (1992) Three-dimensional trajectory analysis and network simulation of deep bed filtration. *J. Colloid. Interface Sci*. **148**, 167.

Burganos V.N., Paraskeva C.A. and Payatakes A.C. (1995) Monte Carlo network simulation of horizontal, upflow, and downflow depth filtration. *AIChE J.* **41**, 272.

Burganos V.N., Skouras E.D., Paraskeva C.A. and Payatakes A.C. (2001) Simulation of the dynamics of depth filtration of non-Brownian particles, *AIChE J.* **47**, 880.

Choo C.U. and Tien C. (1995) Analysis of the transient behavior of deep-bed filtration. *J. Colloid Interface Sci.* **169**, 13.

Cushing R.S. and Lawler D.F. (1998) Depth filtration; fundamental investigation through three dimensional trajectory analysis. *Env. Sci. Tech*. **32**, 3793.

Dixon A.G. and Nijemeisland M. (2001) CFD as a design tool for fixed bed reactors. *Ind. Eng. Chem. Res*. **40**, 5246.

Drew D.A., and Passman S.L. (1998) *Theory of multicomponent fluids* (Applied Mathematical Sciences Springer-Verlag). Vol. 135, Springer, New York.

Dudukovic M.P., Larachi F. and Mills P.L. (1999) Multiphase reactors-revisited. *Chem. Eng. Sci*. **54**, 1975.

Dudukovic M.P., Larachi F. and Mills P.L. (2002) Multiphase catalytic reactors: A perspective on current knowledge and future trends. *Catalyst Reviews.* **44**, 123.

Gray M.R., Srinivasan N. and Masliyah J.H. (2002) Pressure buildup in gas-liquid flow through packed beds due to deposition of fine particles. *Can. J. Chem. Eng*. **80**, 346.

Holub R.A. (1990) *Hydrodynamics of trickle bed reactors*. Ph.D. Thesis, Washington University, St. Louis, Missouri, USA.

Holub R.A, Dudukovic M.P. and Ramachandran P.A. (1992) A phenomenological model for pressure drop, liquid holdup and flow regime transition in gas-liquid trickle flow. *Chem. Eng. Sci*. **47**, 2343.

Holub R.A., Dudukovic M.P. and Ramachandran P.A. (1993) Pressure drop, liquid holdup, and flow regime transition in trickle flows. *AIChE J.* **39**, 302.

Iliuta I., Larachi F. and Grandjean B.P.A. (1998) Pressure drop and liquid holdup in trickle flow reactors: Improved Ergun constants and slip correlations for the slit model. *Ind. Eng. Chem. Res.* **37**, 4542.

Iliuta I., Larachi F. and Al-Dahhan M.H. (2000) Double slit model for partially wetted trickle flow hydrodynamics. *AIChE J.* **46**, 597.

Iliuta I.,Grandjean B.P.A. and Larachi F. (2002) New mechanistic film model for pressure drop and liquid holdup in trickle flow reactors. *Chem. Eng. Sci*. **57**, 3359.

Iliuta I., Larachi F. and Grandjean B.P.A.. (2003a) Fines deposition dynamics in gas-liquid trickle flow reactors. *AIChE J.* **49**, 485.

Iliuta I. and Larachi F. (2003b) Fines deposition dynamics in packed-bed bubble reactors. *Ind. Eng. Chem. Res.* **42**, 2441.

Iliuta I. and Larachi F. (2004) Onset of pulsing in gas-liquid trickle bed filtration. *Chem. Eng. Sci.,* accepted paper

Israelachvili J. (1985) *Intermolecular and surface forces*, Academic Press. London.

Iwasaki T. (1937) Some notes on sand filtration. *J. Amer. Water Works Assoc.* **29**, 1591.

Jiang Y., Khadlikar M.R., Al-Dahhan M.H. and Dudukovic M.P. (1999) Two-phase flow distribution in 2D trickle bed reactors. *Chem. Eng. Sci.* **54**, 2409.

Jiang Y., Khadlikar M.R., Al-Dahhan M.H. and Dudukovic M.P. (2000) Single-phase flow modeling in packed beds: Discrete cell approach revisited. *Chem. Eng. Sci.* **55,** 1829.

Jiang Y., Al-Dahhan M.H. and Duduković M.P. (2001) Statistical characterization of macroscale multiphase flow structures in trickle beds. *Chem. Eng. Sci*. **56**, 1647.

Jiang Y., Khadilkar M.R., Al-Dahhan M.H. and Duduković M.P. (2002) CFD of multiphase flow in packed-bed reactors: I. k-fluid modeling issues. *AIChE J.* **48**, 701.

Kashiwa B.A. and Rauenzahn R.M. (1994a) A multimaterial formalism. ASME *Symposium on Numerical Methods in Multiphase Flows*. FED-vol. 185.

Kashiwa B.A., Padial N.T., Rauenzahn R.M., and VanderHeyden W.B. (1994b) A cell centered ICE method for multiphase flow simulations. ASME Symp. *Numerical Methods for Multiphase Flows*, Lake Tahoe, Nevada.

Khadilkar M.R. (1998) Performance studies of trickle-bed reactors. Ph.D. Thesis, Washington University, St. Louis, Missouri, USA.

Kim S. and Russel W.B. (1985) Modelling of porous media by renormalization of the Stokes equations. *J. Fluid Mech.* **154**, 269.

Kumar S. (1995) Simulation of multiphase flow system using CFDLIB code. CREL Annual Meeting Workshop, St. Louis, Missouri, USA.

Larachi F., Alix C., Grandjean B.P.A. and Bernis A. (2003b) Nu/Sh correlation for particle-liquid heat and mass transfer coefficients in trickle beds based on Péclet similarity. *Chem. Eng. Res. Des. (Trans IChemE part A)*. **81**, 689.

Larachi F., Belfares L., Iliuta I. and Grandjean B.P.A. (2003a) Heat and mass transfer in cocurrent gas-liquid packed beds: Analysis, recommendations, and new correlations. *Ind. Eng. Chem. Res*. **42**, 222.

Larachi F., Iliuta I., Chen M. and Grandjean B.P.A. (1999) Onset on pulsing on trickle beds; Evaluation of current tools and state-of-the-art correlation. *Can. J. Chem. Eng.* **77**, 751.

Martis N., Bentz D.P. and Garboczi E.J. (1994) Computer simulation study of the effective viscosity in Brinkman's equation. *Phys. Fluids.* **6**, 1434.

Mota M., Teixeira J.A. and Yelshin A. (1999) Image analysis of packed beds of spherical particles of different sizes. *Sep. Pur. Tech.* **15**, 59.

Narayan R., Coury J.R., Masliyah J.H. and Gray M.R. (1997) Particle capture and plugging in packed bed reactors. *Ind. Eng. Chem. Res.* **36,** 4620.

O'Melia C.R. and Ali W. (1978) The role of retained particles in deep bed filtration. *Prog. Wat. Tech.* **10**, 167.

Ortiz-Arroyo A., Larachi F., Grandjean B. P. A. and Roy S. (2002) CFD modeling and simulation of clogging in packed beds with non-aqueous media. *AIChE J.* **48,** 1596.

Padial N.T., VanderHeyden W.B., Rauenzahn R.M. and Yarbro S.L. (2000) Three-dimensional simulation of a three phase draft-tube bubble column. *Chem. Eng. Sci*. **55**, 3261.

Paraskeva C.A., Burganos V.N. and Payatakes A.C. (1991) Three-dimensional trajectory analysis of particle deposition in constricted tubes, *Chem. Eng. Commun*. **108**, 23.

Payatakes A.C. (1973) A new model for granular porous media –application to filtration through packed beds. Ph.D. Thesis, Syracuse University, New York.

Payatakes A.C., Park H.Y. and Petrie J. (1981) A visual study of deposition and reentrainment during depth filtration of hydrosols with a polyelectrolyte, *Chem. Eng. Sci.* **36**, 1319.

Payatakes A.C., Rajagopalan R. and Tien C. (1974a) Application of porous media models to the study of deep filtration. *Can. J. Chem. Eng.* **52**, 722.

Payatakes A.C., Tien C. and Turian R.M. (1974b) Trajectory calculation of particle deposition in deep bed filtration: Part I. Model formulation. *AIChE J.* **20**, 889.

Rahimi P., Gentzis T., Taylor E., Carson D., Nowlan V. and Cotté E. (2001) The impact of cut point on the processability of Athabasca bitumen. *Fuel*. **80**, 1147.

Rajagopalan R. and Tien C. (1976) Trajectory analysis of deep bed filtration with the sphere-in-cell porous media model. *AIChE J.* **22**, 523.

Rege S.D. and Fogler H.S. (1988) A network model for deep bed filtration of solid particles and emulsion drops. *AIChE J.* **34**, 1761.

Saez A.E. and Carbonell R. G. (1985) Hydrodynamic parameters for gas-liquid cocurrent flow in packed beds. *AIChE J.* **31**, 52.

Sanaie N., Watkinson A.P., Bowen B.D. and Smith K.J. (2001) Effect of minerals on coke precursor formation. *Fuel.* **80**, 1111.

Speight J.G. (1999) *The chemistry & technology of petroleum.* 3rd edition, Marcel Dekker Inc., New York, 909 p.

Speight J.G. (2001) *Handbook of petroleum analysis.* John Wiley & Sons, Inc., 477p.

Stanek V.J. and Szekely J. (1974) Three-dimensional flow of fluids through nonuniform packed beds. *AIChE J.* **20**, 974.

Stephan E.A. and Chase G.G. (2000) Development of volume average theory for deep bed filtration. *AIChE J.* **46**, 1918.

Tanabe K. and Gray M.R. (1997) Role of fine solids in the coking vacuum residues. *Energy & Fuels*. **11**, 1041.

Thompson G.J. (1996) *UOP RCD Unionfining process*, in R.A. Meyers (Ed.), Handbook of petroleum refining processes. 2nd edition, McGraw-Hill, NY, USA, Chapter 8.4.

Tien C. (1989) *Granular filtration of aerosols and hydrosols.* Butterworth-Heinemann series in Chemical Engineering, Boston MA.

Tien C. (2000) Hydrosol deposition in porous media: The effect of surface interactions. *Adv. Pow. Technol*. **11**, 9.

Tien C. and Payatakes A.C. (1979) Advances in deep bed filtration. *AIChE J.* **25**, 737.

Vaidyanathan R. and Tien C. (1988) Hydrosol deposition in granular beds. *Chem. Eng. Sci*. **43**, 289.

Wang S., Chung K.H., Masliyah J.H. and Gray M.R. (1999) Deposition of fine particles in packed beds at hydrotreating conditions: Role of surface chemistry. *Ind. Eng. Chem. Res.* **38**, 4878.

Wang S., Chung K.H. and Gray M.R. (2001) Role of hydrotreating products in deposition of fine particles in reactors. *Fuel*. **80**, 1079.

Wauquier J.P. (1994) Pétrole brut, produits pétroliers, schémas de fabrication. Éditions Technip, 478p.

Figure captions

Figure 3.1 Slit geometry for determining collection efficiency and filter coefficient in trickle-bed reactors.

Figure 3.2 Single-phase (monolayer) collection efficiency vs. N_R and N_{Lo}.

Figure 3.3 Effect of gas throughput on two-phase (monolayer) collection efficiency vs. N_R

Figure 3.4 Combined effects of liquid velocity and holdup on two-phase (monolayer) collection efficiency.

Figure 3.5 Effect of deposit porosity on the multilayer two-phase collection efficiency.

Figure 3.6 Effect of deposit permeability on the multilayer two-phase collection efficiency.

Figure 3.7 Effect of interception group on the multilayer two-phase collection efficiency.

Figure 3.8 Comparison of the experimental data of Gray et al. (2002) vs. CFD simulations (a) spherical catalyst, (b) trilobe catalyst.

Figure 3.9 Snapshots of the contour plots of the specific deposit buildup and the rise of solids volume fraction with respect to the initial clean bed state in the trickle bed containing 4 mm spherical catalysts.

Table 3.1 Experimental filtration conditions simulated in CFD (Gray et al. 2002 data).

Experimental conditions	
Properties of materials	
Liquid	Kerosene
Viscosity	2 mPa·s
Density	801 kg/m^3
Gas	Air
Density	1.3 kg/m^3
Fines	Kaolinite
Average diameter	0.7 μm
Density	2000 kg/m^3
Porosity of deposit layer	
	0.80 (spherical)
	0.74 (trilobe)
Packing	
1. Spherical catalyst	
Diameter	0.004 m
Bed porosity	0.385
2. Trilobe catalyst	
Effective diameter	0.00129 m
Bed porosity	0.425
Bed size	
Diameter	0.038 m
Height	0.9 m

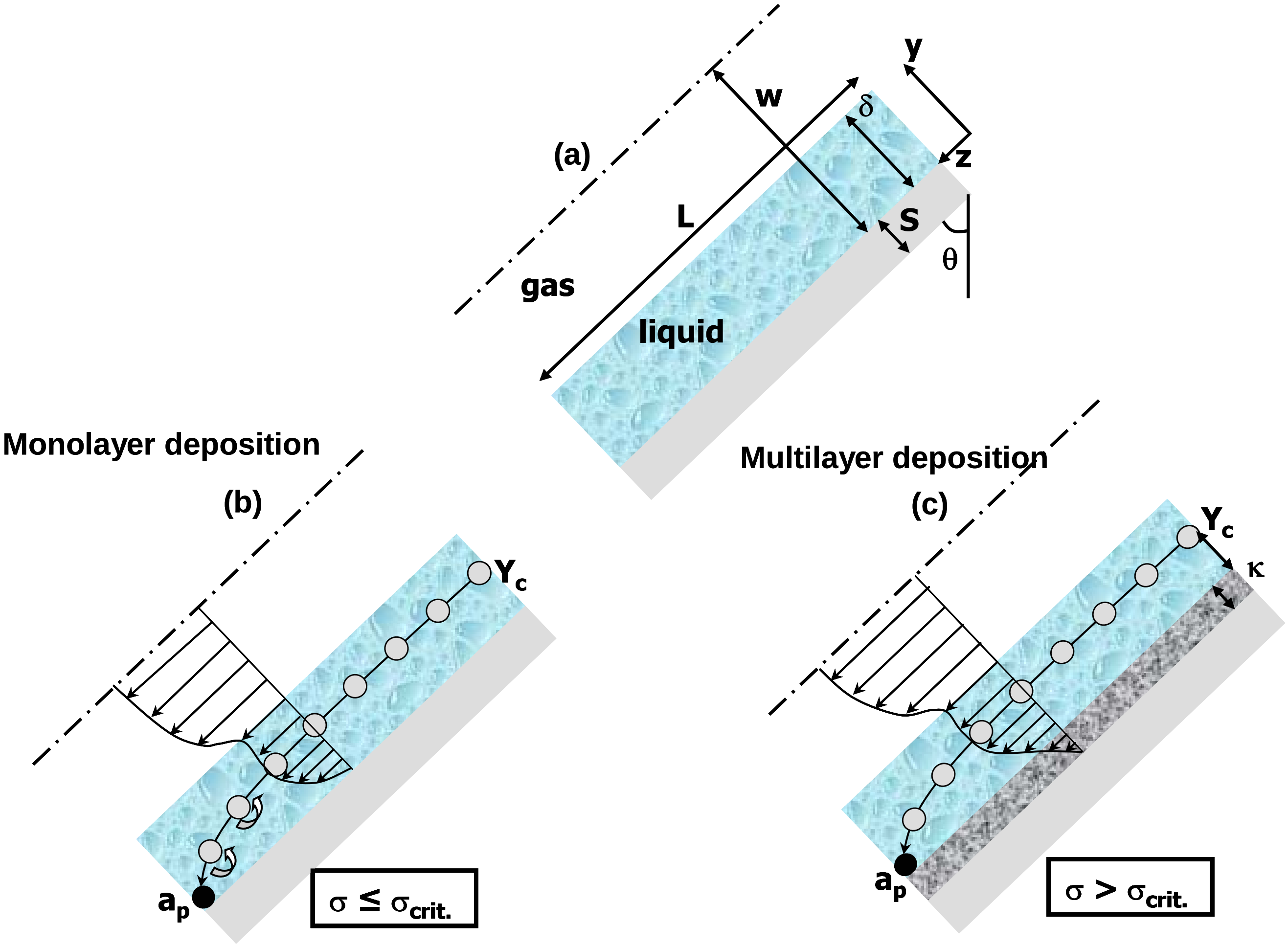

Figure 3.1 Slit geometry for determining collection efficiency and filter coefficient in trickle-bed reactors.

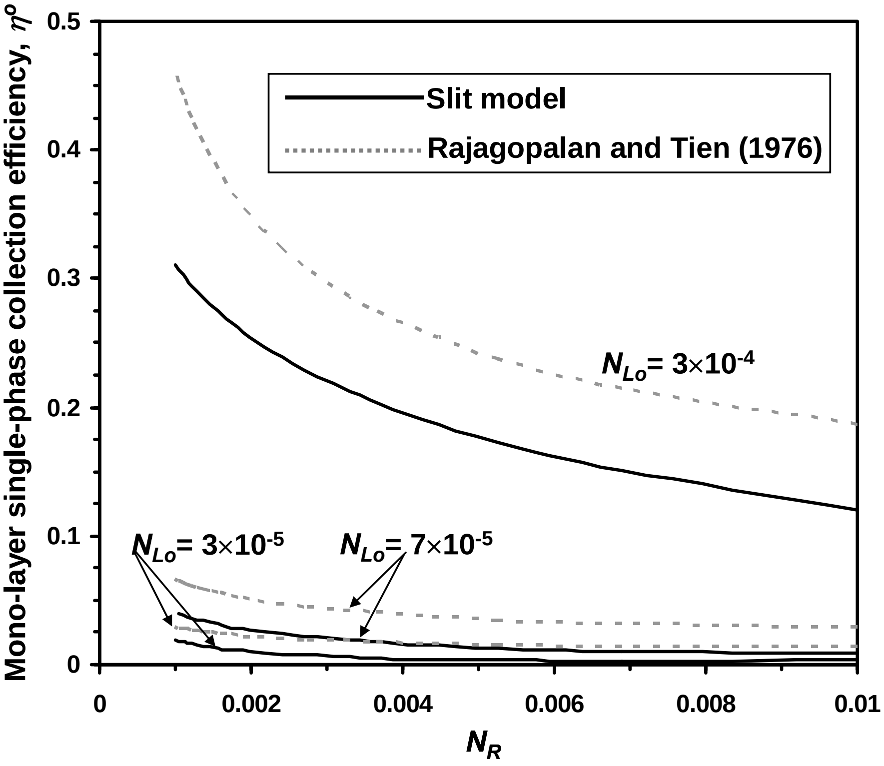

Figure 3.2 Single-phase (monolayer) collection efficiency vs. N_R and N_{Lo}.

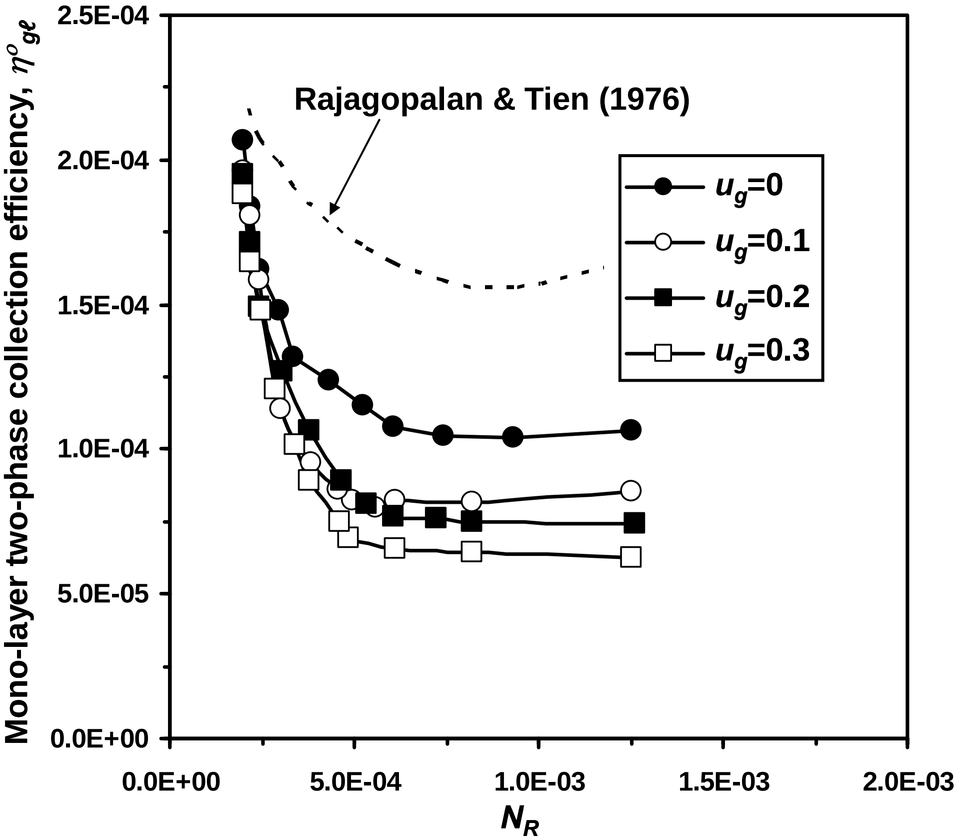

Figure 3.3 Effect of gas throughput on two-phase (monolayer) collection efficiency vs. N_R.

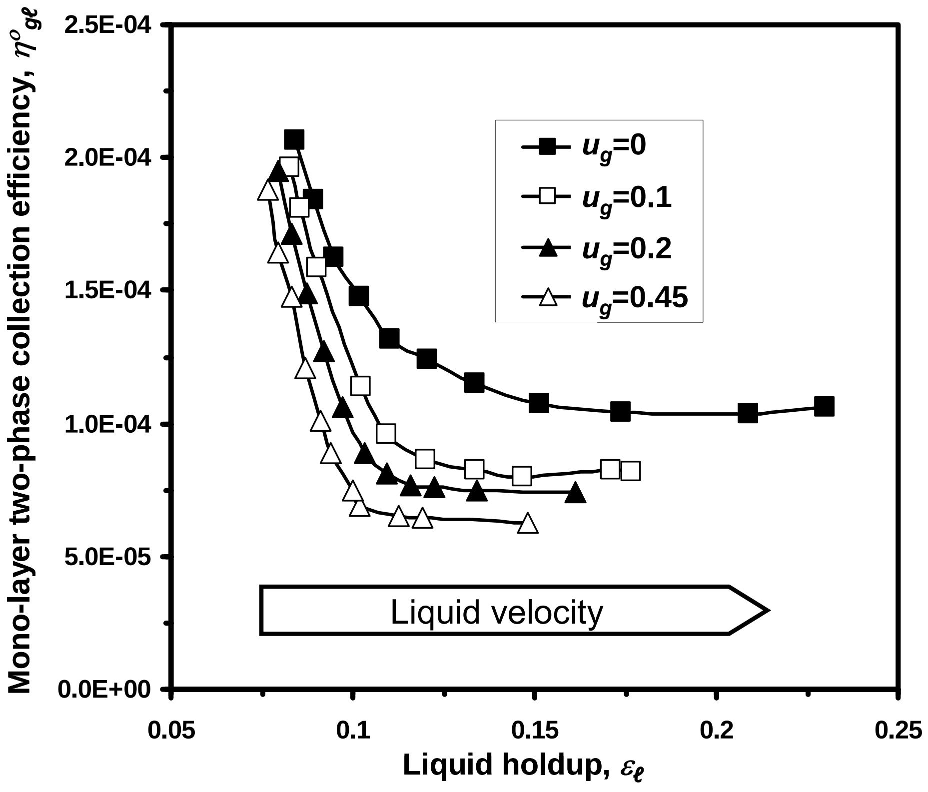

Figure 3.4 Combined effects of liquid velocity and holdup on two-phase (monolayer) collection efficiency.

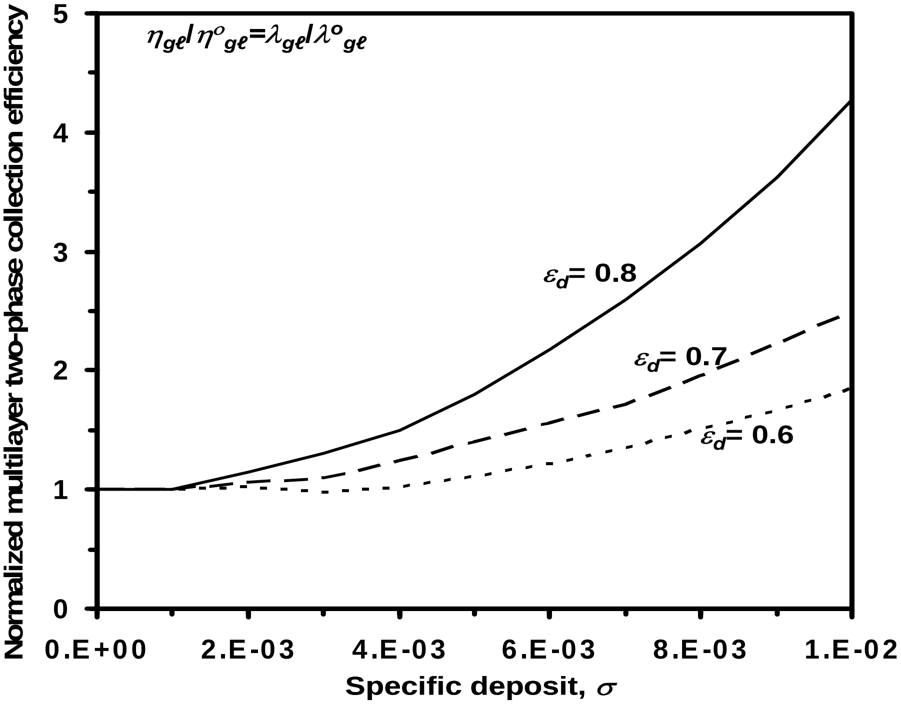

Figure 3.5 Effect of deposit porosity on the multilayer two-phase collection efficiency.

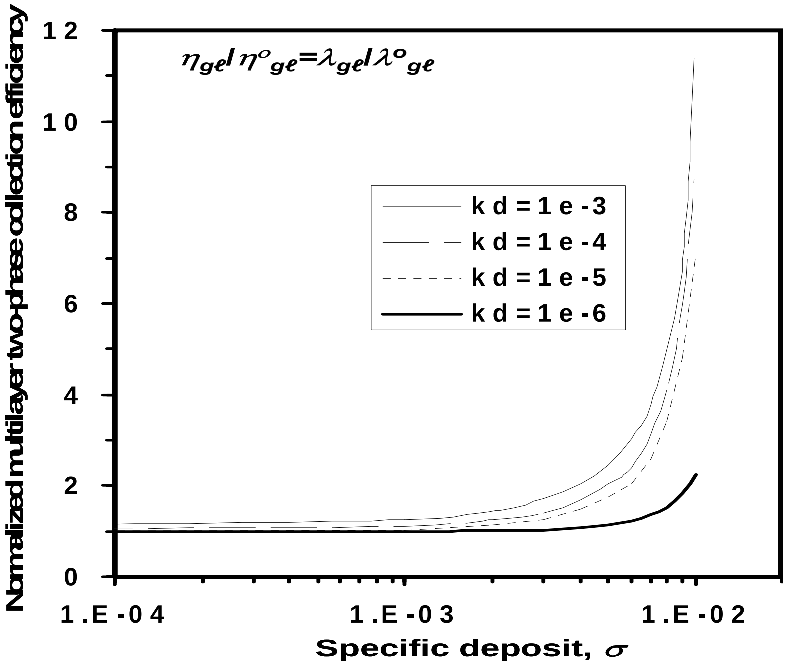

Figure 3.6 Effect of deposit permeability on the multilayer two-phase collection efficiency.

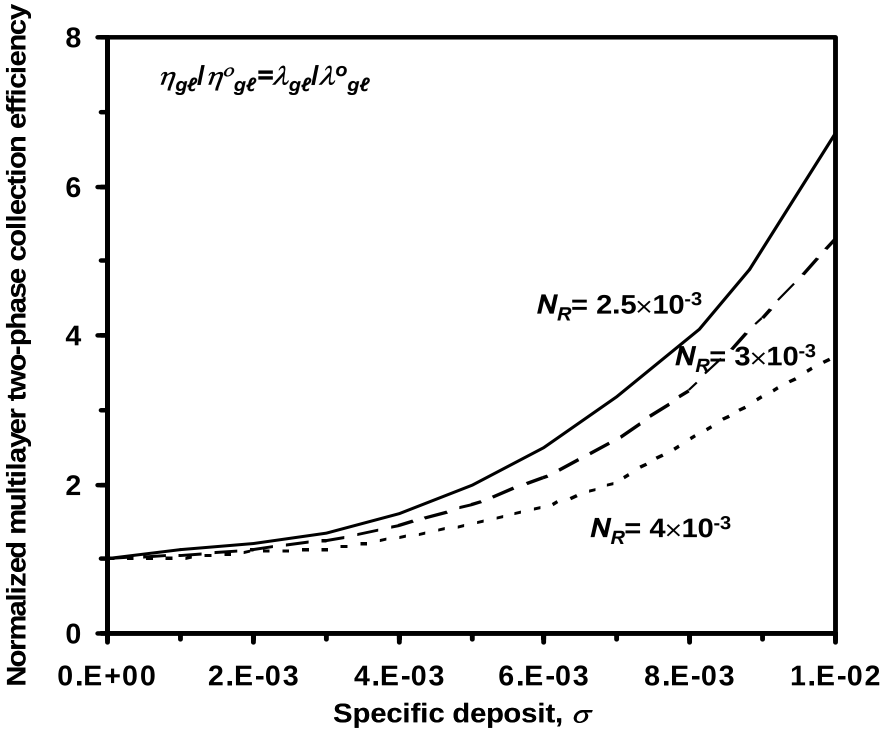

Figure 3.7 Effect of interception group on the multilayer two-phase collection efficiency.

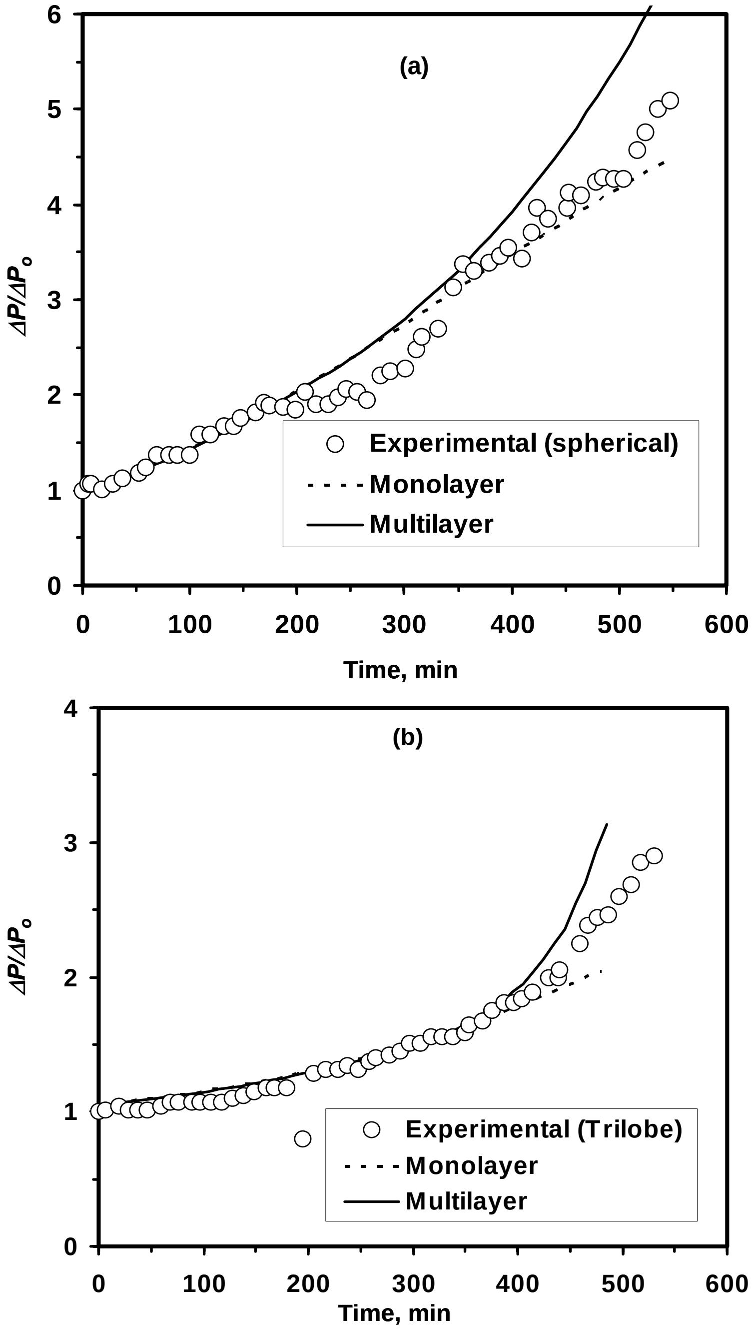

Figure 3.8 Comparison of the experimental data of Gray et al. (2002) vs. CFD simulations (a) spherical catalyst, (b) trilobe catalyst.

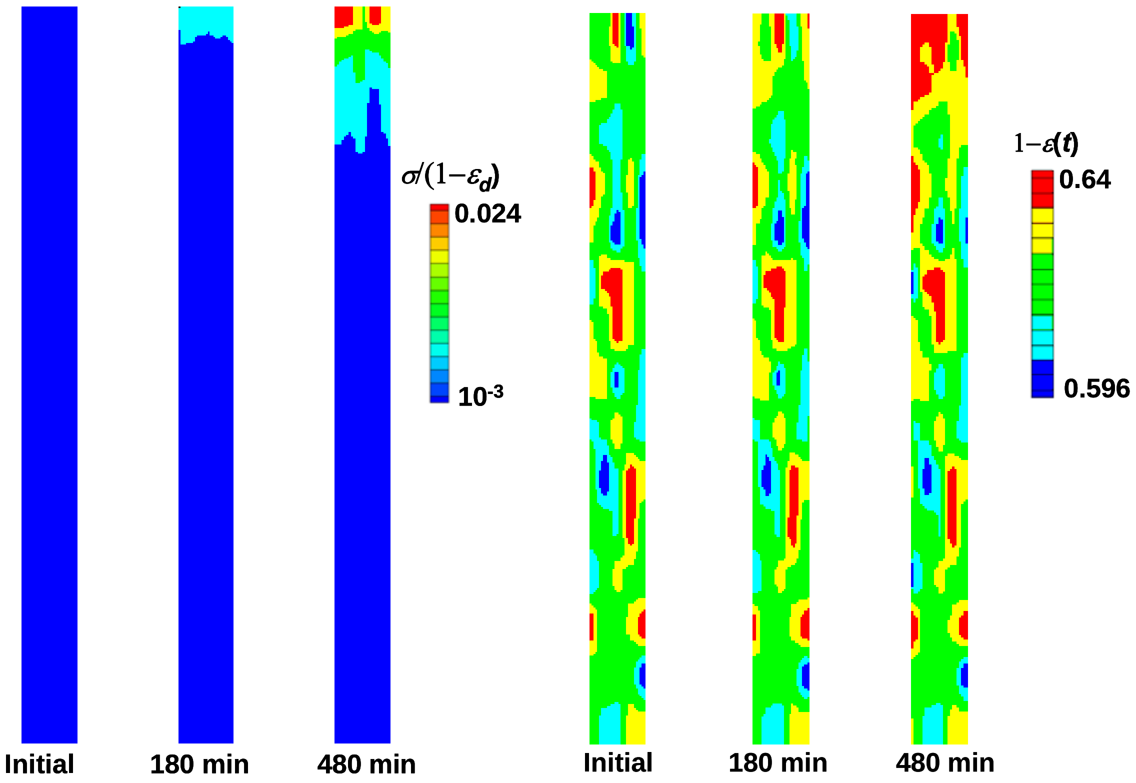

Figure 3.9 Snapshots of the contour plots of the specific deposit buildup and the rise of solids volume fraction with respect to the initial clean bed state in the trickle bed containing 4 mm spherical catalysts.

CHAPTER 4

A method to estimate static liquid holdup in packed beds

Résumé

La rétention liquide statique (SLH), est une mesure de la limite supérieure de la fraction liquide passive de volume présent dans les lits fixes. Ce paramètre est important dans la conception de plusieurs procédés de design de réaction, séparation et transport ainsi que dans des corrélations de variables hydrodynamiques fondamentales telles que la rétention liquide totale, l'efficacité de mouillage et la perte de pression. Les données expérimentales de la rétention liquide statique rapportée jusqu'à présent semblent se stabiliser à un plateau près de 5% quand la force capillaire domine la force de gravité. Par conséquent, la plupart des corrélations publiées ont été construites tenant compte de ce comportement asymptotique, malgré le fait que des valeurs fiables de SLH bien au delà de 5% ont été également rapportées en particulier pour des nombres de Bond tendant vers zéro. La thermodynamique et l'analyse dimensionnelle de l'équation de bilan de forces (Young-Laplace) suggèrent que SLH dépend, mis à part du nombre de Bond (Bo) et des caractéristiques géométriques du lit et du garnissage, de l'angle de contact à la jonction où les interfaces gaz-liquide et liquide-garnissage se réunissent. L'angle de contact, étant difficile à mesurer, a été généralement négligé dans la plupart des analyses, et dans la pratique, rarement incorporés comme quantité calculable dans la majorité de corrélations publiées de SLH. Par conséquent dans ce travail, on a proposé une méthode pour inclure théoriquement l'angle de contact à partir d'une analyse d'énergie des interfaces de ménisque obtenue à partir de la résolution de l'équation bidimensionnelle de Young-Laplace pour deux sphères en contact alignées à la verticale. L'approche a prouvé que des angles de contacts obtenus par cette approche sont comparables à ceux mesurés au laboratoire avec une erreur moyenne de 17%. D'après cette détermination, une nouvelle corrélation de SLH basée sur l'angle de contact (θc), le nombre de Bond (Bo), le rapport solide-volume vide $(1-\varepsilon)/\varepsilon$, la sphéricité de garnissage (φ), et le rapport de volume de lit-volume de garnissage, BPR, a été proposée et analysée à la lumière de la plupart des données publiées de SLH, c.-à-d., 239 mesures pendant les cinquante dernières années. La corrélation de SLH conduit à une erreur moyenne de 23%. L'analyse de sensibilité de ses poids a montré un impact important de l'angle de contact comme variable d'entrée. La corrélation s'est également avérée capable de capturer des valeurs de SLH excédant 5% dans la limite où $Bo \rightarrow 0$.

Method for Inferring Contact Angle and for Correlating Static Liquid Hold-up in Packed Beds

(By Arturo Ortiz-Arroyo, Faïçal Larachi and Ion Iliuta)

Published in *Chem. Eng. Sci.* 58, n13*,* 2835-2855, 2003

Abstract

Static liquid hold-up (SLH), which is an upper bound measure of the passive liquid volume fraction in packed beds, comes into play in several reaction-separation-transport design models and in correlations of fundamental hydrodynamic variables such as total liquid hold-up, wetting efficiency and pressure gradient. Early reported experimental static liquid hold-ups in packed beds seemed to level off at a plateau of *ca.* 5% when capillary force dominates over gravity. Hence, most of the published correlations were constructed taking this asymptotic feature into account, despite the fact that reliable SLH values well beyond 5% were also reported particularly for Bond numbers tending towards zero. Thermodynamics and dimensional analysis of the interfacial momentum balance (Young-Laplace) equation suggests that SLH depends, besides the Bond number (Bo) and some packing and bed characteristic lengths, on an *effective* contact angle at the junction where the gas-liquid interface and the packing-gas boundary meet. The contact angle, being difficult to measure, was generally disregarded in most analyses, and in practice, seldom incorporated as a computable quantity in the majority of published SLH correlations. Therefore in this work, a method was proposed for inferring *theoretically* the contact angle from an energy analysis of the meniscus interfaces' area obtained from solving the 2-D Young-Laplace equation for two vertically-aligned touching equivalent spheres. The approach showed that the intuited contact angles matched the measured ones, when available, with an average error of 8.6%. Following this determination, a new SLH correlation based on the contact angle (θ_c), the Bond number (Bo), the solid-to-void volume ratio $(1-\varepsilon)/\varepsilon$, the packing sphericity (ϕ), and the bed-to-packing volume ratio, BPR, was proposed and analyzed in the light of most published SLH data, i.e., 338 measurements over the past five decades. The SLH correlation yielded an average error of 23%. Sensitivity analysis of its weights showed an important impact of the contact angle as an input variable. The correlation was also found to capture SLH values exceeding 5% in the limit of Bo → 0.

Keywords Static holdup, packed bed, Young-Laplace equation, meniscus, contact angle, correlation

4.1 Introduction

Gas-liquid flow fixed beds are common tubular contacting devices in a great deal of industries, *e.g.*, biotechnology, petroleum and chemical processing, wastewater treatment, and so forth. Due to their importance, small improvements in the operation of such processing units usually translate into huge savings for the involved industries. However, the design and scale-up/down of these columns are by and large commanded by art when the scientific knowledge is lacking. The development of robust experimentally-validated and physically-sound models to predict the hydrodynamic, and the reaction/separation performance parameters involved in these systems remains a permanent and important task to which reactor engineers are confronted.

Liquid hold-up plays a key role in the hydrodynamics, in the heat and mass transfers as well as in the reaction and separation performances of these three-phase systems. Static liquid hold-up (SLH), which is an upper bound measure of the passive liquid volume fraction in porous media, comes into play in several reaction-separation-transport design models and in correlations of the transport parameters. SLH is an outcome of the balance between gravity force, which tends to chase the liquid out of the porous medium, and capillary force, which on the contrary opposes to it. These forces act on the liquid held, in the form of pendular menisci, at the contact points of the particles making up the bed. SLH is known to be detrimental for the mass transfer efficiency. The liquid contributing to SLH remains stagnant and covers a fraction of the packing surface thus impeding transport of the reactant or species in their way down to the porous catalyst or up to the gas-liquid interface. In this sense, it is of interest to minimise the impact of SLH in the operation of multiphase fixed bed reactors.

Two types of external SLH are reported in the literature: SLH measured by bed draining (i.e., residual liquid hold-up) and SLH obtained from a tracing technique (i.e., the liquid in the static hold-up is either totally stagnant or simply flows at a velocity much lower than the liquid bulk). The basic difference between the methods used for evaluation of these two hold-ups is that in tracer experiments the column hydrodynamics is not disturbed as it is during draining. Moreover, the amount of liquid collected by draining the bed depends on the characteristics of the liquid and those of the packing as well as on the draining time. Several researchers concluded that SLH measured by tracing and draining methods are not equivalent, with the former technique yielding a lower hold-up than the latter one (Bennett and Goodridge, 1970; Schubert et al. 1986; Kushalkar and Pangarkar, 1990). In this work, an SLH database was built using *solely* the measurements obtained by draining because this is the most frequent technique used so far in the literature.

SLH in porous media depends on a number of physical variables of the gas-liquid-solid system including shape, size, orientation and coordination of the particles in the porous medium, bed porosity and dimensions, method of packing of the column, purity and properties of the liquid as well as of the solid surface, capillary and gravitational forces, and other physical and thermodynamic properties such as contact angle, dimensionless datum pressure, equilibrium shape and stability of pendular menisci (Saez et al. 1991; Mao et al. 1993). In some studies, besides these variables, viscosity was mentioned as being a factor either weakly (Shulman et al.1955a, b; Standish, 1968) or strongly (Goto and Gaspillo, 1992) influencing SLH so this effect was sometimes included in the SLH correlations. According to Zisman (1964), liquid viscosity could affect liquid adhesion to the solid thus conferring more or less important effects of this factor.

To date, few efforts have been invested in elucidating and obtaining SLH estimation methods based on first-principle conservation equations and rational arguments (Mao et al. 1993, 1994; Kramer, 1998; Stein, 2000) despite the importance and applicability of SLH. For instance, it can be mentioned that some correlations for the external liquid hold-up (Kohler and Richarz, 1985; Stiegel and Shah, 1977) include SLH as a component. Saez and Carbonell (1985) and Nemec et al. (2001) used SLH to estimate the interfacial drag forces during gas-liquid flow in trickle flow regime in atmospheric and high pressure conditions. Grosser et al. (1988) and Dankworth et al. (1990) used similar expressions, with SLH embedded within, to analyse the stability of trickle flow in cocurrent downflow trickle beds. In the multiple-slit model of Iliuta et al. (2000), knowledge of SLH is required to quantify the extent of wetting contributed by both static and dynamic wetting efficiencies in trickle flow. Works on theoretical models for SLH are very scarce (Saez and Carbonell, 1987, 1990; Mao et al. 1993, 1994; Stein, 1999; Kramer, 1998), and the results are still far from being exhaustive.

Early reported experimental SLH in packed beds appeared to level off at a maximum value of 5% for low Bond numbers (Dombrowski and Brownell, 1954; Charpentier et al. 1968). Hence, most of the published correlations were constructed taking this feature into account, despite the fact that reliable SLH values well beyond 5% were also reported particularly for Bond numbers tending towards zero (Mersmann, 1972; Saez et al. 1991; Mao et al. 1993).

Furthermore, dimensional analysis of the interfacial momentum balance equation and of the hydrostatic law suggests that SLH is a function of a Bond number, packing and bed characteristic lengths, datum pressure, and contact angle of the pendular menisci at the junction where the gas-liquid and the packing-gas boundaries meet. The contact angle is very difficult to measure in this configuration and was generally disregarded in most analyses, and in practice, seldom incorporated quantitatively in the majority of published SLH correlations.

To fill in this gap, a method was proposed in this work for inferring *theoretically* the contact angle from an energy analysis of the meniscus interfaces' area obtained from solving the 2-D Young-Laplace equation for two vertically-aligned touching equivalent spheres. Following this determination, an SLH correlation based on the contact angle (θ_c), Bond number (Bo), solid-to-void volume ratio $(1-\varepsilon)/\varepsilon$, packing sphericity ($\phi$), and bed-to-packing volume ratio, BPR, was proposed and analyzed in the light of most published SLH data over the past fifty years.

4.2 Theory

The wettability between a liquid and a solid surface is measured by means of the contact angle between a droplet of liquid in thermal equilibrium and a horizontal surface. The liquid is said to be wetting when the contact angle, θ_c, falls in the range [90 – 180°], and non-wetting when it lies in the range [0 – 90°]. The case where $\theta_c = 0$ or 180° corresponds to perfect wetting and the drop spreads forming a film on the surface.

In the case of particles in a packed bed, the contact angle has an impact on the curvature of the meniscus and therefore has a direct influence on the amount of liquid that can be held in the meniscus.

To determine experimentally the contact angle several problems are encountered. First, the angle depends on the purity of the liquid and the solid surface, any contamination will modify the contact angle. Also, when a liquid moves over a surface, the so called dynamic contact angle is not unique and may have any value between two extremes, depending on whether the liquid is tending to advance over a dry surface or to recede from a previously wetted one. Advancing angles are often larger than receding ones.

The draining method of packed beds gives rise to a receding contact angle of the liquid meniscus. This observation is sustained by the contact angle measurements of Moseley and Dhir (1996) study in which experimental advancing and receding angles were reported for water over spheres. These receding contact angles agreed with those reported by Mao et al. (1993) in their study of SLH in trickle beds. Unfortunately, contact angles on spherical or on any other particle shapes are seldom reported so that incorporation of the contact angle as a *calculable* contribution in an SLH correlation is at present illusory. Therefore an effort is made in this work to extract theoretically the contact angle and to include it in a general SLH correlation.

The contact angle is obtained theoretically from an analysis of the solutions of the Young-Laplace equation for the idealized case of a pendular meniscus anchored at the contact point of two vertically aligned and touching particles. For simplification, spherical shape of the packing is assumed with the two spheres, of equal radius R, centred at (0,R) and (0,-R), respectively (Fig. 4.1). Non-spherical effects are handled *a posteriori* in the SLH correlation via the sphericity factor. These assumptions turn the problem 2-D with menisci exhibiting azimuthally symmetric shapes. It is further assumed that accurate experimental SLH measurements are obtained after the bed is allowed to attain a state of thermodynamic and hydrostatic equilibrium. Under these circumstances, the formed menisci are postulated also to be in thermodynamic and hydrostatic equilibrium. This enables to formulate a mapping relationship between the liquid volume held in a meniscus and the experimentally measured SLH data which reflects the integral contribution of all menisci throughout the whole porous medium.

Under hydrostatic conditions, the interfacial momentum balance equation reduces to the dimensionless Young-Laplace equation (YLE) (Saez and Carbonell, 1987, 1990):

$$\mathrm{Bo}\, C_P + 2H = 0 \tag{4.1}$$

where H is the dimensionless mean curvature of the gas-liquid interface, C_P is a dimensionless datum pressure at the gas-liquid-solid interface and Bo is the Bond number defined as:

$$\mathrm{Bo} = \frac{\rho_\ell g R^2}{\sigma_\ell} \tag{4.2}$$

Eq.4.1 takes the following form in 2-D axisymmetric geometry:

$$\frac{d^2 r}{dx^2}\left(1+\left(\frac{dr}{dx}\right)^2\right)^{-3/2} - r^{-1}\left(1+\left(\frac{dr}{dx}\right)^2\right)^{-1/2} = \mathrm{Bo}\, x - C_P \tag{4.3}$$

where r and x, scaled with respect to R, are respectively the polar (horizontal) and vertical dimensionless coordinates of the interface locus of the meniscus. The meniscus gas-liquid interface intersects the spheres at the contact lines x_1 and x_2 at which the polar components r, lying on the sphere surface (Fig.4.1), are:

$$r(x) = \begin{cases} \sqrt{1-(1+x)^2}, & -2 \le x \le 0 \\ \sqrt{1-(1-x)^2}, & 0 \le x \le 2 \end{cases} \quad (4.4)$$

At the contact lines, the surface of the spheres and the gas-liquid interface meet at an angle θ_c, the contact angle that depends only on the nature of the three phases. The contact angle boundary conditions to be satisfied there are:

$$\left.\frac{dr}{dx}\right|_{x_1} = \left.\frac{dr}{dx}\right|_{x_2} = -\cot(\theta_c) \quad (4.5)$$

The volume of the meniscus, scaled to R^3, writes as:

$$v_\ell = \pi \int r(x)^2 dx - \frac{1}{3}\pi x^2 (3-x) \Big|_{x_1}^{x_2} \quad (4.6)$$

for which the volume restriction is imposed:

$$v_\ell\big|_{x_2} = \breve{v}_\ell = \frac{4\pi}{3(0.298)(1-\varepsilon)N_p} SLH \quad (4.7)$$

where $\breve{v}_\ell$ is the volume of a single meniscus calculated from the experimental SLH and the meniscus-to-bed mapping expression proposed by Mao et al.(1993). The coordination number, N_p, is estimated from empirical correlations or geometrical arguments using one of the three expressions below:

$$N_p = \begin{cases} 4 \\ 3.1/\varepsilon \\ 26.49 - 10.73/(1-\varepsilon) \end{cases} \quad (4.8)$$

proposed respectively by Mao et al. (1993) for centred cubic array, Haughey and Beveridge (1969) for porosities in the range [0.2595 – 0.4764] and German (1989) for the other cases.

At this stage, the problem still possesses infinity of solutions satisfying Eq.4.3. In principle, for a given set (Bo, C_P) and boundary conditions (x_1, x_2, θ_c), only one solution yields the meniscus geometry that exhibits the *thermodynamically stable shape*. The criterion to select this stable solution is obtained from an energy analysis borrowed from the work of Mao et al. (1993). This analysis concerns the change of internal energy of the isolated system consisting of two contacting spheres and a reservoir of liquid when a pendular ring is built up by adding liquid little by little to the spheres contacting point. The thermodynamic equilibrium condition requires minimisation of the interfacial energy equation (Mao et al. 1993):

$$\Delta E_i = \sigma_{g\ell}\left(A_{g\ell} + A_{\ell s}\cos\theta_c\right) \qquad (4.9)$$

where the liquid-solid wetted interface, $A_{\ell s}$, is given by (Spiegel and Liu, 1999):

$$A_{\ell s} = 4\pi x \qquad (4.10)$$

and the gas-liquid interface area is:

$$A_{g\ell} = \int 2\pi r(x)\sqrt{1+\left(\frac{dr}{dx}\right)^2}\,dx \qquad (4.11)$$

The problem of finding the contact angle from Eq. 4.3 is a boundary value problem with the boundary conditions Eq. 4.5. The value to be assigned to parameter C_P determines the solvability of Eq.4.3. The other unknowns to be estimated are the coordinates x_1, x_2 of the lines at which the meniscus intersects the particles. Eq. 4.3 was solved by a collocation method implemented in the MATLAB program bvp4c described in Kierzenka and Shampine (2001). This routine is appropriate for solving boundary value problems involving an unknown parameter, here C_P.

The calculation algorithm for the contact angle proceeds as follows:

1. For a known SLH value, the volume of a single meniscus $\breve{v}_\ell$ is estimated according to Eq. 4.7.

   This equation is a control constraint to direct the search towards stable menisci having a volume compatible with the experimentally determined SLH.
2. The contact angle is initialized at $\theta_c = 0$.

3. Rough initial estimates are assigned for the coordinates of the meniscus on the spheres, x_1 and x_2. Initial estimates for x_1 and x_2 coordinates are calculated considering a cylinder with volume $\breve{\overset{\frown}{\mathrm{v}}}_\ell$ from which is subtracted the volume of the spheres covered by the cylinder.
4. As an initial guess of the datum pressure, C_P was the theoretical value obtained by Cuvelier and Schulkes (1990) for the YLE solved in free boundary conditions: $C_P = \breve{\overset{\frown}{\mathrm{v}}}_\ell \, \mathrm{Bo} - 2\cos\theta_c$.
5. Starting from x_1, an estimate of the gas-liquid interface locus r(x) is obtained from which is calculated the contact angle at the arrival point x_2. This point is iterated until the boundary condition Eq. 4.5 yields the same contact angles at x_1 and x_2 within a prescribed tolerance (typically ±1%).
6. Location x_1 is iterated using a *Regula falsi* method and step 5 is repeated until the volume constraint Eq. 4.7 is fulfilled.
7. The interfacial energy given by Eq. 4.9 is evaluated and stored with the solution ($r(x)$, x_1, x_2, θ_c, C_P).
8. The contact angle is incremented and the algorithm is resumed again at step 3. Fig. 4.2 illustrates some simulated menisci shapes parameterised by the contact angle for a system described by Bo = 0.0516 and SLH = 0.115. All such solutions satisfy the volume constraint Eq. 4.7 so that energy discrimination is required to choose the most stable one.
9. After sweeping a wide θ_c interval, the interfacial energy is plotted versus the contact angle θ_c. The one corresponding to the minimum energy is chosen as the most probable contact angle for the given SLH value and experimental conditions. An illustration of the search for the minimum energy meniscus is given in Fig. 4.3 for different SLH and Bo number values in the SLH database.

The proof-of-concept for extracting theoretical estimates of contact angles from knowledge of the experimental SLH values is validated against truly measured contact angle data. Mao et al. (1993) measured the contact angle for liquids with different surface tensions on spheres and three-lobed extrudates. The proposed procedure was tested by comparing the theoretical contact angles to the measured ones and the results are summarized in Table 4.1. The approach showed that the theoretical contact angles matched the measured ones with an average error of 8.6%. It is worth mentioning that the proposed approach reflects an effective (or averaged) contact angle of all the menisci that occur in the bed rather than a contact angle measured in controlled clean liquid and surface conditions.

4.3 Development of a new SLH correlation

4.3.1 SLH database

SLH data (338 experimental points) expressed as the volume fraction of the porous space with respect to reactor volume, were collected from 42 references published over the past fifty years. Many such SLH data are single averages of a set of SLH data. A wide range of liquid physical properties, packing and column geometries are included (see Table 4.2 for a summary of the database). Draining was always the experimental method for SLH determination. The SLH data of Gelbe (1968), Andrieu (1975), Rehani (1983) and Kücükkafa (1985) were taken from the database presented in Stein (2000). It was not possible to exploit all the data available in the literature because of a lack of information on the experimental conditions, e.g., packing dimensions and height of packing not specified. Finally, the data from Rao et al. (1983) were discarded considering that these authors reported atypically high SLH up to 26% for conventional packings.

4.3.2 ANN SLH correlation

A three-layer feed-forward artificial neural network (ANN) was retained as a regression model for SLH. Several variables that include information about SLH in packed beds were tried such as the number of contact points, numerous functions of porosity, modified forms of the Bond number, etc. Only those that gave better statistical performance and congruency in the functional tendency of the correlation were retained. Details on such ANN model building are provided elsewhere and will not be repeated here for the sake of brevity (Larachi et al. 2001). Table 4.3 lists the set of equations of the SLH ANN correlation wherein the network output, i.e., normalized SLH, was correlated to five input dimensionless variables chosen to include the most pertinent physical variables of the problem in accordance with the dimensional analysis of the Young-Laplace equilibrium equation:

- The Bond number (Bo), representing the capillary and gravitational forces ratio.
- $(1-\varepsilon)/\varepsilon$, is the solid-to-void volume ratio in the bed accounting for the number of points of contact between particles and the dependency of SLH on porosity.
- The packing sphericity (ϕ) is proposed as a means to handle the mismatch to spherical shape, e.g., Raschig rings, three-lobed extrudates, etc., for which the YLE was not directly solved. The sphericity factor is defined as the ratio of the surface area of an equivalent sphere of equal volume to the actual surface area of the particle.

- The bed-to-packing ratio, BPR, defined as the ratio of the packed bed volume to that of an individual particle to account for the number of particles in the vessel.
- The contact angle (θ_c) which embeds the thermodynamic state of the three-phase system and the stability of the stagnant liquid menisci.

The NNfit software (Cloutier et al. 1996) was used to develop the ANN correlation. In Table 4.3, H_3 and U_6 are the bias constants set equal to 1. The weighting factors (or connectivity weights) ω_{ij} and ω_j of the ANN correlation (Table 4.3) are obtained through nonlinear least-squares regression on a set of input and output data taken from the SLH database. To overcome the over-fitting problem which may alter the network generalization capabilities, the database was split in two sets of historical data. The first set of historical data, obtained from randomly sampling 70% of the SLH database served for the identification of the weighting factors and for the training of the correlation. The second set of historical data was then used to test the neural correlation on how well it was trained. To determine the optimal number of hidden nodes, *j* was varied from 1 to 5. Hidden layers with up to two neurons were found to be the optimal neural architectures leading to the smallest average absolute relative error and standard deviation on the training and generalization sets and were judged sufficient to keep the number of weights to a minimum given the limited number of data used.

4.3.2 Analysis of the proposed SLH correlation

The importance and pertinence of the input variables into the SLH ANN correlation were evaluated using a partition method of the neural network connection weights proposed by Garson (1991). The results of this analysis are summarised in Table 4.4. As can be seen and as expected, Bo number is most influential on SLH with 51% of the effect on the connectivity weights. It is followed in order of decreasing importance by the solid-to-void volume ratio (18.1%) and the contact angle (16.8%) which both exhibit moderate influence on SLH. Finally, the sphericity factor (9.8%) and the bed-to-packing ratio (5.2%) convey the minor effects on SLH. Definitely, the contact angle represents a non-negligible contribution in explaining the SLH variation and must be included in any meaningful SLH correlation.

Fig. 4.4 shows a parity plot of the measured static liquid hold-ups included in the database versus the predicted SLH values given by the ANN correlation summarized in Table 4.3. More than 90% of the SLH experiments fall within the ± 44.6% envelopes (2 times the average absolute relative error, AARE). The AARE by the SLH ANN correlation is 3 to 10 times less than any AARE given by the available literature SLH correlations/models (Table 4.5). The agreement achieved by this new correlation is very good on the 239 SLH data of the database. It is followed by the well known Saez and Carbonell (1985) and Stein (2000) correlations which are recognized to be among the best SLH correlations. Here the predictions by the Saez and Carbonell (1985) correlation were compared to 83 SLH data that fulfilled the valid ranges of the correlation. The Stein (2000) correlation was more general and embraced 184 SLH data. It is noteworthy that in this case, we have used the contact angle estimated by our present method since θ_c is one of the Stein (2000) correlation inputs. The method of Mao et al. (1993) produced less satisfactory predictions because the meniscus volume was not estimated from integration of the YLE geometric solution but rather approximated from the maximum meniscus volume given by an empirical correlation proposed by Turner and Hewitt (1959) for large-sized particles. Moreover, instead of using the tetra-coordination assumption of Mao et al. (1993), we have used the coordination number correlation of German (1989) which produced less scatter.

The proposed SLH correlation was exhaustively tested to avoid physical inconsistencies or functional misbehaviour. These tests were performed by varying one characteristic variable of interest at a time while keeping all the others constant. The packing size, liquid density, liquid surface tension, bed porosity, sphericity factor, and contact angle were chosen for the evaluation of the SLH correlation.

As an illustration in Fig 4-5a, the behaviour of the SLH correlation is shown as a function of the packing diameter. Consistent with knowledge from the literature (Saez and Carbonell, 1985; Saez et al. 1991; Stein, 2000), the smaller the particle size the larger the static liquid hold-up. The effects of liquid density and surface tension appear to adhere congruently to the physics of the phenomenon, i.e., higher SLH corresponding to lower liquid density and higher surface tension (Fig. 4.5b). Porosity effects on SLH are illustrated in Fig.4-5c. In the literature some contradictions seem to occur. According to Saez and Carbonell (1985) and Saez et al. (1991), porosity affects very marginally SLH in the typical porosity range, i.e., 30-50 %. However, Kramer (1998) model indicates a strongly decreasing trend of SLH with the increase in bed porosity. Conversely, analysis of Stein (2000) and Mao et al. (1993) models suggests that SLH is an increasing function of bed porosity. The presently developed correlation appears to be in agreement with these last observations (Fig4-5c). Finally, departure from the spherical shape configuration seems to favour an increase in SLH as shown in Fig. 4.5d.

When analysing the behaviour of the predicted SLH while varying the contact angle, no clear cuts could be drawn because most of the surfaces dealt with yielded a contact angle varying between 25 and

31 degrees. However, a general trend observed was that increased contact angles entrained a reduction in SLH especially for relatively high Bond numbers. In this case, the simulated menisci were distorted by the gravity effect pulling the upper triple point (gas-liquid-solid interface location) towards the sphere-sphere contact point. To fulfil the meniscus volume constraint and thus SLH value, the contact angle was correspondingly increased to allow a stable meniscus to be obtained.

4.4 Conclusion

Static liquid hold-up is an important parameter in the operation, design and scale up of packed beds. Using an algorithm based on the solution of the Young-Laplace equation that governs the formation of liquid meniscus imprisoned between two spheres, a bed-averaged contact angle was calculated by a suitable algorithm. The procedure used a constant volume restriction based on the experimental SLH and a minimum energy thermodynamic criterion to ensure identification of the contact angle corresponding to the most stable meniscus. With the calculated contact angle, a new SLH correlation was obtained from an exhaustive search of experimental data in the available literature. The result was a more complex correlation involving five dimensionless numbers all coherent with the dimensional analysis of the Young-Laplace equation for a stable meniscus. The new expression has achieved a far better accuracy than the known literature correlations.

Nomenclature

ANN	artificial neural network
AARE	average absolute relative error (–)
$A_{g\ell}$	meniscus gas-liquid area (m^2)
$A_{\ell s}$	wetted area by meniscus on the spheres (m^2)
Bo	Bond number (–)
BPR	bed-to-packing volume ratio (–)
C_P	dimensionless datum pressure (–)
D_c	column diameter (m)
d_v	equivalent particle diameter of sphere having equal volume (m)
$\mathbf{g}$	gravitational acceleration (m/s^2)
H	dimensionless mean curvature of the meniscus interface (–)
Hb	packed bed height (m)
N	number of SLH data
Np	coordination number (–)
R	radius of equivalent sphere having same volume as particle (m)
r	dimensionless polar coordinate of the gas-liquid interface locus (–)
SLH	static liquid hold-up (–)
$\tilde{\breve{v}}_{\ell}$	dimensionless liquid volume in a single meniscus (–)
YLE	Young-Laplace equation
x	dimensionless vertical coordinate of the gas-liquid interface locus (–)
x_1,x_2	vertical coordinates where meniscus meets spheres (–)

Greek letters

ΔE_i	interfacial energy change (J)
ε	bed porosity (–)
ϕ	packing sphericity factor (–)
$\omega_{i,j}$	weight factors in neural network correlation (–)
ρ_ℓ	liquid density (kg/m^3)

σ_ℓ	liquid surface tension (N/m)
θ_c	contact angle (°)

References

Al-Dahhan M.H. (1993) Effects of high pressure and fines on the hydrodynamics of trickle bed reactors. D. Sc. Dissertation, Washington University, St. Louis Missouri.

Aleabaei A.M. (1986) Messung und Korrelation des Flüssigkeitsinhaltes in Vollzylinder und Kugelschüttungen. Diplomarbeit D-21/86, Institut für Thermodynamik und Anlagentechnik der TU Berlin, Germany.

Andrieu J. (1975) Influence of wettability on liquid phase texture in a countercurrently irrigated packing. *Chem. Eng. Sci.* **30**, 217.

Azzaz M.J. (1984) Réacteurs gaz-liquide-solide à lit fixe. Réactions catalytiques, hydrodynamique et transfert de matière. Ph.D. Thesis, Institut Polytechnique de Lorraine, Nancy, France.

Bakos M. and Charpentier J.C. (1970) Taux de rétention pour des écoulements gaz-liquide à co-courant vers le bas dans les colonnes à garnissage arrosé et noyé. *Chem. Eng. Sci.* **25**, 1822.

Basu A.K. (1984) Messung und Korrelation des Flüssigkeitsinhaltes in Füllkörperschüttungen. Diplomarbeit. D-18/84, Institut für Thermodynamik und Anlagentechnik der TU Berlin, Germany.

Bennett A. and Goodridge F. (1970) Hydrodynamics and mass transfer studies in packed absorption columns. Part 1: Axial liquid dispersion. *Trans. Inst. Chem. Eng*. **48**, 232.

Buchanan J.E. (1969) Pressure gradient and liquid hold-up in irrigated packed towers. *Ind. Eng. Chem. Fund.* **8**, 502.

Charpentier J.C., Prost C., Van Swaaij W.P.M. and Le Goff P. (1968) Étude de la rétention de liquide dans une colonne à garnissage arrosé à co-courant et à contre-courant de gaz-liquide. Représentation de sa texture par un modèle à filets et gouttes. *Chimie et Ind.-Génie Chimique.* **99**, 803.

Charpentier J.C. and Favier M. (1975) Some liquid hold-up experimental data in trickle bed reactors for foaming and nonfoaming hydrocarbons. *AIChE J.* **21**, 1213.

Cloutier P., Tibirna C., Grandjean B.P.A. and Thibault J. (1996) NNfit, logiciel de régression utilisant les réseaux neuronaux à couches. http ://www.gch.ulaval.ca/~nnfit,

Colombo A.J., Baldi G. and Sicardi S. (1976) Solid-liquid contacting effectiveness in trickle bed reactors. *Chem. Eng. Sci*. **31**, 1101.

Cuvelier C. & Schulkes R.M.S.M. (1990) Some numerical methods for the computation of capillary free boundaries governed by the Navier-Stokes equations. *SIAM Review,* **32**, 335.

Dankworth D.C., Kevrekidis I.G. and Sundaresan S. (1990) Dynamics of pulsing flow in trickle beds. *AIChE J.* **36**, 605.

Dombrowski H.S. and Brownell L.E. (1954) Residual equilibrium saturation of porous media. *Ind. Eng. Chem.* **46**, 1207.

Gardner G.C. (1956) Hold-up and pressure drop for water irrigating 'non-wettable' coke. *Chem. Eng. Sci.* **5**, 101.

Garson G.D. (1991) Interpreting neural-network connection weights. *AI Expert*. **4**, 47.

Gelbe H. (1968) A new correlation for liquid hold-up in packed beds. *Chem. Eng. Sci.*, **23**, 1401.

German R.W. (1989) *Particle Packing Characteristics.* Metal Powders Industries Federation, Princeton, USA.

Goto S. and Smith J.M. (1975) Trickle bed reactor performance. Part I. Hold-up and mass transfer effects. *AIChE J*. **21**, 706.

Goto S. and Gaspillo P.D. (1992) Multiple hydrodynamic states in gas-liquid upflow and downflow through beds of small packings. *Ind. Eng. Chem. Res*. **31**, 629.

Grosser K., Carbonell R.G. and Sundaresan S. (1988) Onset of pulsing in two phase cocurrent downflow through a packed bed. *AIChE J.* **34**, 1850.

Haughey D.P. and Beveridge G.S.G. (1969) Structural properties of packed beds-Review. *Can. J. Chem. Eng.* **47**, 130.

Iliuta I. (1996) Hydrodynamics and mass transfer in multiphase fixed bed reactors. Ph.D. Thesis, Université Catholique de Louvain, Louvain, Belgium.

Iliuta I., Larachi F. and Al-Dahhan M.H. (2000) Multiple-zone model for partially wetted trickle flow hydrodynamics. *Trans. Inst. Chem. Eng.* **78**, 982.

Khan A., Khan A.A. and Varma Y.B.G. (2000) An analysis of phase hold-up in concurrent gas-liquid upflow through packed beds using (I) drift flux model, and (II) slip ratio. *Bioproc. Eng.* **22**, 165.

Kierzenka J. and Shampine L. (2001) A BVP solver based on residual control and the MATLAB PSE. *ACM Trans. Math. Soft.* **3**, 199.

Kohler M. and Richarz W. (1985) Investigation of liquid hold-up in trickle bed reactors. *Ger. Chem. Eng.* **8**, 295.

Kramer G.J. (1998) Static liquid hold-up and capillary rise in packed beds. *Chem. Eng. Sci.* **53**, 2985.

Kücükkafa A. (1985) Messung und Korrelation des Flüssigkeitsinhaltes in Raschigring-, stegring- und pallring- Schüttungen. Diplomarbeit D-20/85, Institut für thermodynamik und Anlagentechnik der TU Berlin, Germany.

Kushalkar K.B. and Pangarkar V.G. (1990) Liquid hold-up and dispersion in packed columns. *Chem. Eng. Sci.* **45**, 759.

Lakota A. (1990) Hydrodynamics and mass transfer characteristics of trickle bed reactors. Ph.D. Thesis. University of Ljubljana, Slovenia,.

Larachi F., Belfares L., Iliuta I. and Grandjean B.P.A. (2001) Three-phase fluidization macroscopic hydrodynamics revisited. *Ind. Eng. Chem. Res.* **40**, 993.

Levec J., Saez A.E. and Carbonell R.G. (1986) The hydrodynamics of trickling flow in packed beds. Part II. Experimental observations. *AIChE J.* **32***,* 369.

Mao Z.S., Xiong T.Y. and Chen J.Y. (1993) Theoretical prediction of static liquid hold-up in trickle bed reactors and comparison with experimental results. *Chem. Eng. Sci.* **48**, 2697.

Mao Z.S., Xiong T.Y., Wang R. and Chen J.Y. (1994) Note on the hydrodynamic stability of pendular rings between solid particles. *Chem. Eng. Sci.* **49**, 3519-3521.

Mekuc L. and Levec J. (1994) On the static (residual) liquid hold-up in trickle bed reactors. *Acta Chimica Slovenica.* **41**, 305.

Mersmann A. (1972) Restflüssigkeit in schüttungen. *Verfahrenstechnik.* **6**, 203.

Mersmann A. (1975) Fluid dynamics of fluid two-phase system. Int. Congr. Chem. Engng Equipment Design Automation, I2.1, Prague, Czechoslovakia,

Morsi B.I., Midoux N. and Charpentier J.C. (1978) Flow patterns and some hold-up experimental data in trickle bed reactors for foaming, non-foaming and viscous organic liquids. *AIChE J.* **24**, 357.

Morsi B.I. (1982) Hydrodynamique, aires interfaciales et coefficients de transfert de matière gaz-liquide dans les réacteurs catalytiques à lit fixe arrosé: Les résultats obtenus en milieu liquide aqueux académique sont-ils encore représentatifs en milieu organique industriel?. PhD Thesis, Institut National Polytechnique de Lorraine, Nancy, France.

Moseley W.A. and Dhir V.K. (1996) Capillary pressure-saturation relations in porous media including the effect of wettability. *J. Hydrol.* **178**, 33.

Nemec D., Bercic G. and Levec J. (2001) The hydrodynamics of trickling flow in packed beds operating at high pressures. The relative permeability concept. *Chem. Eng. Sci.* **56**, 5955.

Nenniger E. and Storrow J.A. (1958) Drainage of packed beds in gravitational and centrifugal-force fields. *AIChE J.* **4**, 305.

Pironti F., Mizrahi D., Acosta A. and Gonzalez-Mendizabal D. (1999) Liquid-solid wetting factor in trickle-bed reactors; its determination by a physical method. *Chem. Eng. Sci.* **54**, 3793.

Purwasasmita M. (1985) Contribution à l'étude des réacteurs gaz-liquide à lit fixe fonctionnant à co-courant vers le bas à fortes vitesses du gaz et du liquide. Hydrodynamique, transfert de matière et de chaleur pour des liquides aqueux et organiques. Ph.D. Thesis, Institut National Polytechnique de Lorraine, Nancy, France.

Rao V.G., Ananth M.S. and Varma Y.B.G. (1983) Hydrodynamics of two-phase co-current downflow through packed beds. Part II: Experiments and correlations. *AIChE J.* **29**, 473.

Rehani D.V. (1983) Untersuchung des Flüssigkeitsinhaltes in Dünnwandigen Raschigring- und in Vorbehandelten und Unbehandelten Pallringschüttungen. Studienarbeit S-12/83, Institute für Thermodynamik und Anlagentechnik der Berlin, Germany.

Saez A.E. and Carbonell R.G. (1985) Hydrodynamic parameters for gas-liquid cocurrent flow in packed beds. *AIChE J.* **31**, 52.

Saez A.E. and Carbonell R.G. (1987) The equilibrium shape and stability of menisci formed between two touching cylinders. *J. Fluid Mech.* **176**, 357.

Saez A.E. and Carbonell R.G. (1990) The equilibrium and stability of menisci between touching spheres under the effect of gravity. *J. Coll. Int. Sci.* **140**, 408.

Saez A.E., Yepes M.M., Cabrera C. and Soria E.M. (1991) Static liquid holudp in packed beds of spherical particles. *AIChE J.* **37**, 1733.

Schubert C.N., Lindner J.R. and Kelly R.M. (1986) Experimental methods for measuring static liquid hold-up in packed columns. *AIChE J.* **32**, 1920.

Shulman H.L., Ullrich C.F. and Wells N. (1955a) Performance of packed columns I. Total, static and operational hold-ups. *AIChE J.* **1**, 247.

Shulman H.L., Ulrich C.F., Wells N. and Proulx A.Z. (1955b) Performance of packed columns. III Hold-up for aqueous and non-aqueous systems. *AIChE J.* **1**, 259.

Specchia V. and Baldi G. (1977) Pressure drop and liquid hold-up for two-phase co-current flow in packed beds. *Chem. Eng. Sci.* **32**, 515-523.

Spiegel M.R. and Liu J. (1999) *Mathematical handbook of formulas and tables*. Schaum's Series 2nd Ed., McGraw Hill.

Standish N. (1968) Some observations on the static hold-up of aqueous solutions and liquid metals in packed beds. *Chem. Eng. Sci.* **23**, 945.

Stein W.A. (1999) Benetzung und Zwickelflüssigkeit bei zwei nebeneinander liegenden zylindern. *Forschung in Ingenieurwesen*. **12**, 329.

Stein W.A. (2000) Der Statische Flüssigkeitsanteil in Packungskolonnen. *Forschung in Ingenieurwesen*. **66**, 129.

Stiegel G.J. and Shah Y.T. (1977) Backmixing and liquid hold-up in a gas-liquid co-current upflow packed column. *Ind. Eng. Chem. Proc. Des. Dev.* **16**, 37.

Tsochatzidis N.A., Ntampegliotis K.I. and Karabelas A.J. (1998) Effect of viscosity on hydrodynamic properties of pulsing flow in trickle beds. *Chem. Eng. Comm.* **166**, 137.

Turner G.A. and Hewitt G.F. (1959) The amount of liquid held at the point of contact of spheres and the static liquid hold-up in packed beds. *Trans. Inst. Chem. Eng.* **37**, 329.

Van Swaaij W.P.M., Charpentier J.C. and Villermaux J. (1969) Residence time distribution in the liquid phase of trickle flow in packed columns. *Chem. Eng. Sci.* **24**, 1083.

Wammes W.J.A. (1990) Hydrodynamics in a cocurrent gas-liquid trickle-bed reactors at elevated pressures. Ph.D. thesis, Twente University, Enschede, The Netherlands.

Wammes W.J.A., Mechielsen S.J. and Westerterp K.R. (1990) The transition between trickle flow and pulse flow in a cocurrent gas-liquid trickle bed reactor at elevated pressures. *Chem. Eng. Sci.* **45**, 3149.

Warner N.A. (1959) Liquid metal irrigation of a packed bed. *Chem. Eng. Sci.*, **11**, 149.

Yang X.L., Wild G. and Euzen J.P. (1993) Study of liquid retention in fixed bed reactors with upward flow of gas and liquid. *Int. Chem. Eng.* ***33***, 72.

Zisman W.A. (1964) Relation of equilibrium contact angle to liquid and solid constitution. *Advances in Chemistry Series.* **43**, 1-52.

Zun I., Perpar M. and Filipic B. (1997) Probe measurements of local carrying gas fraction in trickle bed reactor. *Exp. Therm. Fluid Sci.* **15**, 163.

Figure captions

Figure 4.1 Domain and geometry definition for solving the Young-Laplace equation.

Figure 4.2 Calculated menisci for various contact angles at constant Bo and SLH values (Bo=0.052, SLH=0.115).

Figure 4.3 Typical simulations of interfacial energy change versus contact angle showing minimum energy corresponding to the contact angle for the stable menisci. Simulation for low, moderate and high Bond numbers at various SLH values.

Figure 4.4 Parity plot of the measured versus predicted SLH (AARE=22.3%, N=239). Envelopes correspond to within ± 2 AARE predictions.

Figure 4.5 Neural network correlation simulations, SLH vs. (a) particle size, (b) surface tension and liquid density, (c) bed porosity, (d) sphericity factor at various liquid densities while keeping all other properties constant**.**

Table 4.1 Measured contact angles from Mao et al. (1993) compared with the contact angles estimated with the algorithm proposed in this work

Liquid	Experimental ($\theta_{c,\ exp}$)	Bo	Calculated ($\theta_{c,calc}$)	ARE(%)
Water (Glass beads)	31.7	0.089	30.5	3.8
Water (Glass beads)	31.7	0.289	28.0	11.7
Water (Al_2O_3: 3-L)	15.8	0.051	14.0	11.39
10% Glycerol (Glass beads)	37.4	0.094	33.0	11.76
10% Glycerol (Glass beads)	37.4	0.305	34.0	9.09
10% Glycerol (Al_2O_3 3-L)	17.7	0.054	16.0	9.6
50% Glycerol (Al_2O_3 3-L)	17.0	0.057	15.5	8.82
90% Ethanol (Al_2O_3 3-L)	14.9	0.044	14.5	2.6
			AARE =	8.6 %*

3-L: Three lobbed extrudate; ARE = 100 x $|\theta_{exp}-\theta_{calc}|/\theta_{exp}$

Table 4.2 Database summary including calculated contact angles, measured SLH, packing and fluid characteristics.

Ref	Liquid	ρ_l kg/m^3	μ_l Pa·s	σ_l N/m	Packing	Packing Material	d_v m	ϕ	ε	D_c m	H_c m	θ_c (°)	SLH
Al-Dahhan, 1993	Hexane	663	0.0003	0.0188	Spheres	Silica shell	0.0015	1.0000	0.4119	0.0222	0.5125	28.5	0.0566
	Hexane	663	0.0003	0.0188	Spheres	Glass	0.0011	1.0000	0.3920	0.0219	0.5171	29.0	0.0578
	Hexane	663	0.0003	0.0188	Cylinders	Catalyst porous	0.0025	0.7936	0.3548	0.0219	0.5161	33.0	0.0235
	Water	1000	0.0010	0.0720	Cylinders	Catalyst porous	0.0025	0.7936	0.3548	0.0219	0.5161	31.0	0.0395
	Water	1000	0.0010	0.0720	Spheres	Glass	0.0011	1.0000	0.3920	0.0219	0.5171	26.0	0.0952
	Water	1000	0.0010	0.0720	Spheres	Silica shell	0.0015	1.0000	0.4306	0.0219	0.5481	25.0	0.1040
Aleabaei,1986	Water	1000	0.0010	0.0720	Spheres	Aluminium	0.0020	1.0000	0.7970	0.0750		7.0	0.0688
	Water	1000	0.0010	0.0720	Spheres	Glass	0.0060	1.0000	0.6540	0.0750		27.0	0.0328
	Ethyleneglycol	1109	0.0200	0.0480	Spheres	Glass	0.0060	1.0000	0.6540	0.0750		28.5	0.0262
	Water	1000	0.0010	0.0720	Spheres	Glass	0.0080	1.0000	0.6700	0.0750		26.0	0.0367
	Ethyleneglycol	1109	0.0200	0.0480	Spheres	Glass	0.0080	1.0000	0.6700	0.0750		28.5	0.0240
	Water	1000	0.0010	0.0720	Spheres	Glass	0.0100	1.0000	0.6710	0.0750		29.5	0.0329
	Ethyleneglycol	1109	0.0200	0.0480	Spheres	Glass	0.0100	1.0000	0.6710	0.0750		28.0	0.0240
	Water	1000	0.0010	0.0720	Spheres	Ceramic	0.0120	1.0000	0.6070	0.1500		27.0	0.0347
	Ethyleneglycol	1109	0.0200	0.0480	Spheres	Ceramic	0.0120	1.0000	0.6070	0.1500		28.5	0.0299
	Water	1000	0.0010	0.0720	Spheres	Ceramic	0.0160	1.0000	0.5520	0.1500		29.0	0.0324
	Ethyleneglycol	1109	0.0200	0.0480	Spheres	Ceramic	0.0160	1.0000	0.5520	0.1500		30.0	0.0252
	Water	1000	0.0010	0.0720	Spheres	Ceramic	0.0210	1.0000	0.6290	0.1500		30.5	0.0203
	Ethyleneglycol	1109	0.0200	0.0480	Spheres	Ceramic	0.0210	1.0000	0.6290	0.1500		29.0	0.0166
Andrieu,1975	Water	1000	0.0010	0.0720	Raschig rings	Glass		0.4300	0.3100	0.1500			0.0373
	Water	1000	0.0010	0.0720	Raschig rings	Parafined		0.4300	0.3100	0.1500			0.0159
Azzaz,1984	Water	999	0.0010	0.0724	Spheres	Glass	0.0031	1.0000	0.3840	0.0500	1.0000	31.0	0.0357
	Sulfite+water	1098	0.0018	0.0491	Spheres	Glass	0.0031	1.0000	0.3840	0.0500	1.0000	32.0	0.0346
	Kerosene	784	0.0011	0.0250	Spheres	Glass	0.0031	1.0000	0.3840	0.0500	1.0000	33.0	0.0311
	Gasoil	838	0.0052	0.0291	Spheres	Glass	0.0031	1.0000	0.3840	0.0500	1.0000	31.0	0.0323
	Ethyleneglycol	1109	0.0208	0.0470	Spheres	Glass	0.0031	1.0000	0.3840	0.0500	1.0000	32.0	0.0342
	Polyethylene glycol	1124	0.0646	0.0398	Spheres	Glass	0.0031	1.0000	0.3840	0.0500	1.0000	34.0	0.0334
	Polyethylene glycol	1124	0.0646	0.0398	Raschig rings		0.0018	0.3987	0.4850	0.0500	1.0000	32.0	0.0257
	Gasoil	838	0.0052	0.0291	Raschig rings		0.0018	0.3987	0.4850	0.0500	1.0000	30.0	0.0233
	Kerosene	784	0.0011	0.0250	Raschig rings		0.0018	0.3987	0.4850	0.0500	1.0000	29.0	0.0209

Bakos & Charpentier,1970	Water	1000	0.0010	0.0720	Spheres	Glass	0.0030	1.0000	0.3850	0.0100		31.0	0.0327
	Water	1000	0.0010	0.0720	Spheres	Porous Al catalyst	0.0030	1.0000	0.3850	0.0100		32.0	0.0173
Basu,1984	Water	1000	0.0010	0.0720	Raschig rings	Aluminium		0.4030	0.5050	0.1500			0.0207
	Ethyleneglycol	1109	0.0200	0.0480	Raschig rings	Aluminium		0.4030	0.5050	0.1500			0.0201
	Methanol	791	0.0006	0.0230	Raschig rings	Aluminium		0.4030	0.5050	0.1500			0.0146
	Water	1000	0.0010	0.0720	Raschig rings	Aluminium		0.4030	0.4090	0.1500			0.0192
	Ethyleneglycol	1109	0.0200	0.0480	Raschig rings	Aluminium		0.4030	0.4090	0.1500			0.0204
	Methanol	791	0.0006	0.0230	Raschig rings	Aluminium		0.4030	0.4090	0.1500			0.0144
	Water	1000	0.0010	0.0720	Raschig rings	Aluminium		0.4030	0.2290	0.1500			0.0232
	Ethyleneglycol	1109	0.0200	0.0480	Raschig rings	Aluminium		0.4030	0.2290	0.1500			0.0206
	Methanol	791	0.0006	0.0230	Raschig rings	Aluminium		0.4030	0.2290	0.1500			0.0148
	Water	1000	0.0010	0.0720	Raschig rings	Aluminium		0.4030	0.1670	0.1500			0.0283
	Ethyleneglycol	1109	0.0200	0.0480	Raschig rings	Aluminium		0.4030	0.1670	0.1500			0.0195
	Methanol	791	0.0006	0.0230	Raschig rings	Aluminium		0.4030	0.1670	0.1500			0.0152
Bennett &Goodbridge,1970	Water	1000	0.0010	0.0720	Raschig rings	Ceramic		0.3900	0.6800	0.0510			0.0620
	Water	1000	0.0010	0.0720	Raschig rings	Ceramic		0.3900	0.6900	0.0760			0.0400
Buchanan,1969	Water	1000	0.0010	0.0710	Raschig rings	Ceramic	0.0149	0.3987	0.7010	0.1461	1.3970	27.0	0.0260
	45% sucrose+water	1204	0.0055	0.0650	Raschig rings	Ceramic	0.0149	0.3987	0.7010	0.1461	1.3970	28.5	0.0220
	60% sucrose+water	1263	0.0450	0.0690	Raschig rings	Ceramic	0.0149	0.3987	0.7010	0.1461	1.3970	28.0	0.0220
	67.5% sucrose+water	1331	0.2000	0.0690	Raschig rings	Ceramic	0.0149	0.3987	0.7010	0.1461	1.3970	29.0	0.0210
	Dieseline	810	0.0020	0.0270	Raschig rings	Ceramic	0.0149	0.3987	0.7010	0.1461	1.3970	30.0	0.0170
Charpentier & Favier,1975	Water	1000	0.0011	0.0750	Spheres	Glass	0.0030	1.0000	0.3800	0.0500	1.2000	31.0	0.0399
	Water	1000	0.0011	0.0750	Spheres	Catalyst	0.0030	1.0000	0.3900	0.0500	1.2000	29.0	0.0429
	Kerosene	790	0.0010	0.0253	Spheres	Catalyst	0.0030	1.0000	0.3900	0.0500	1.2000	32.5	0.0300
	Cyclohexane	780	0.0009	0.0250	Spheres	Catalyst	0.0030	1.0000	0.3900	0.0500	1.2000	32.0	0.0300
	Water	1000	0.0011	0.0750	Cylinders	Catalyst	0.0031	0.7628	0.3900	0.0500	1.2000	32.0	0.0312
	Kerosene	790	0.0010	0.0253	Cylinders	Catalyst	0.0024	0.7520	0.3700	0.0500	1.2000	33.0	0.0285
	Cyclohexane	780	0.0009	0.0250	Cylinders	Catalyst	0.0024	0.7520	0.3700	0.0500	1.2000	32.0	0.0285
	Gasoline	840	0.0006	0.0252	Cylinders	Catalyst	0.0024	0.7520	0.3700	0.0500	1.2000	33.0	0.0285

	Desulfurized gasoil	860	0.0050	0.0288	Cylinders	Catalyst	0.0024	0.7520	0.3700	0.0500	1.2000	32.0	0.0296
	Non desulfurized gasoil	860	0.0050	0.0283	Cylinders	Catalyst	0.0024	0.7520	0.3700	0.0500	1.2000	31.0	0.0296
	Petroleum ether	650	0.0003	0.0190	Cylinders	Catalyst	0.0024	0.7520	0.3700	0.0500	1.2000	32.5	0.0222
Charpentier et al.1968	Water	1000	0.0010	0.0715	Raschig rings	Glass	0.0056	0.3781	0.7000	0.1000	2.1000	30.0	0.0252
	80% isopropanol+ water	870	0.0034	0.0270	Raschig rings	Glass	0.0096	0.4142	0.6700	0.1000	2.0800	26.5	0.0275
	Water	1000	0.0010	0.0715	Raschig rings	Glass	0.0096	0.4142	0.6700	0.1000	2.0800	27.5	0.0261
	70% saccharose +water	1260	0.0500	0.0645	Raschig rings	Glass	0.0096	0.4142	0.6700	0.1000	2.0800	27.0	0.0302
	Water	1000	0.0010	0.0715	Raschig rings	Glass siliconed	0.0096	0.4142	0.6900	0.1000	2.0500	31.0	0.0097
	Water	1000	0.0010	0.0715	Raschig rings	Polyethylene	0.0201	0.4367	0.7300	0.2000	2.7200	27.5	0.0168
Colombo et al.1976	Water	1000	0.0010	0.0720	Crushed particles	Carbon activated	0.0010	0.6500	0.3610	0.0300	1.0000	31.0	0.0440
	Water	1000	0.0010	0.0720	Cylinders		0.0047	0.8684	0.4190	0.0300	1.0000	27.0	0.0760
Dombrowski & Brownell,1954	Lead solution	1464	0.0021	0.0665	Spheres	Glass	0.000023	1.0000	0.3560	0.1000	0.1079	31.0	0.0235
	Lead solution	1464	0.0021	0.0665	Spheres	Glass	0.000077	1.0000	0.3520	0.1000	0.0220	23.0	0.0151
	Lead solution	1464	0.0021	0.0675	Spheres	Glass	0.000014	1.0000	0.3670	0.1000	0.4359	32.0	0.0286
	Lead solution	1464	0.0021	0.0685	Spheres	Glass	0.000010	1.0000	0.3790	0.1000	0.5907	34.0	0.0277
	Lead solution	1467	0.0021	0.0699	Spheres	Glass	0.000038	1.0000	0.3670	0.1000	0.5907	31.0	0.0314
	Lead solution	1467	0.0021	0.0699	Spheres	Glass	0.000046	1.0000	0.3700	0.1000	0.0789	31.0	0.0263
	Lead solution	1467	0.0021	0.0709	Spheres	Glass	0.000077	1.0000	0.3520	0.1000	0.0789	28.0	0.0299
	Lead solution	1467	0.0021	0.0719	Spheres	Glass	0.000046	1.0000	0.3700	0.1000	0.0789	30.0	0.0281
	Lead solution	1467	0.0021	0.0729	Spheres	Glass	0.000038	1.0000	0.3670	0.1000	0.1234	33.0	0.0273
	Water	995	0.0010	0.0742	Spheres	Glass	0.000077	1.0000	0.3520	0.1000	0.0701	29.0	0.0186
	Water	995	0.0010	0.0741	Spheres	Glass	0.000046	1.0000	0.3700	0.1000	0.1899	32.0	0.0222
	Water	995	0.0010	0.0741	Spheres	Glass	0.000077	1.0000	0.3520	0.1000	0.1591	28.0	0.0282
	Water	995	0.0010	0.0741	Spheres	Glass	0.000046	1.0000	0.3700	0.1000	0.1981	31.5	0.0220
	Mineral oil	876	0.1893	0.0366	Spheres	Glass	0.000077	1.0000	0.3520	0.1000	0.0552	33.0	0.0300
	Water	995	0.0010	0.0739	Spheres	Glass	0.000016	1.0000	0.3760	0.1000	0.4511	31.0	0.0414
	Water	995	0.0010	0.0739	Spheres	Glass	0.000016	1.0000	0.3760	0.1000	0.4511	30.0	0.0323

	Water	995	0.0010	0.0739	Spheres	Glass	0.000038	1.0000	0.3670	0.1000	0.3420	32.0	0.0295
	Water	995	0.0010	0.0739	Spheres	Glass	0.000038	1.0000	0.3670	0.1000	0.3347	31.0	0.0288
	Mineral oil	876	0.1893	0.0368	Spheres	Glass	0.000046	1.0000	0.3700	0.1000	0.2225	28.0	0.0259
	Water	995	0.0010	0.0738	Spheres	Glass	0.003380	1.0000	0.3280	0.1000	0.0199	34.0	0.0120
	Water	995	0.0010	0.0733	Spheres	Glass	0.000016	1.0000	0.3760	0.1000	0.5304	29.0	0.0252
	Water	995	0.0010	0.0733	Spheres	Glass	0.000077	1.0000	0.3520	0.1000	0.0881	30.0	0.0222
	Water	995	0.0010	0.0734	Spheres	Glass	0.000108	1.0000	0.4350	0.1000	0.0710	32.0	0.0335
	Water	995	0.0010	0.0734	Spheres	Glass	0.003380	1.0000	0.3280	0.1000	0.0710	33.0	0.0169
	Mineral oil	876	0.1893	0.0366	Spheres	Glass	0.003380	1.0000	0.3280	0.1000	0.0710	31.0	0.0248
	Water	995	0.0010	0.0734	Spheres	Glass	0.004420	1.0000	0.4080	0.1000	0.0710	32.0	0.0271
	Mineral oil	876	0.1893	0.0366	Spheres	Glass	0.004420	1.0000	0.4080	0.1000	0.0710	33.0	0.0215
	Mineral oil	876	0.1893	0.0368	Spheres	Glass	0.003380	1.0000	0.3280	0.1000	0.0710	33.0	0.0225
	Mineral oil	876	0.1893	0.0366	Spheres	Glass	0.005300	1.0000	0.4300	0.1000	0.0710	32.0	0.0163
	Mineral oil 2	966	0.0550	0.0355	Spheres	Glass	0.000038	1.0000	0.3670	0.1000	0.0710	31.0	0.0257
	Hyvac oil	886	0.1846	0.0364	Crushed particles	Quartz	0.000171	0.9200	0.4380	0.1000	0.0229	28.0	0.0521
	Hyvac oil	902	0.1856	0.0374	Crushed particles	Quartz	0.000077	0.9200	0.4410	0.1000	0.3277	29.0	0.0426
Gardner,1956	Water	1000	0.0010	0.0720	Spheres	Carbon	0.0095	1.0000	0.5830	0.2290		28.0	0.0321
	Water	1000	0.0010	0.0720	Spheres	Carbon	0.0159	1.0000	0.5440	0.2290		31.0	0.0213
	Water	1000	0.0010	0.0720	Spheres	Glass	0.0222	1.0000	0.5380	0.2290		32.5	0.0163
Gelbe,1968	Water	1000	0.0010	0.0720	Raschig rings	Glass		0.4100	0.2970	0.0760			0.0340
	Ethyleneglycol	1109	0.0200	0.0480	Raschig rings	Glass		0.4100	0.2900	0.0450			0.0320
	Methanol	791	0.0006	0.0230	Raschig rings	Glass		0.4100	0.2900	0.0450			0.0320
	Water	1000	0.0010	0.0720	Raschig rings	Glass		0.4000	0.2400	0.0760			0.0300
	Ethylenglycol	1109	0.0200	0.0480	Raschig rings	Glass		0.4000	0.2400	0.0760			0.0280
	Methanol	791	0.0006	0.0230	Raschig rings	Glass		0.4000	0.2400	0.0760			0.0310
	Water	1000	0.0010	0.0720	Raschig rings	Glass		0.4200	0.2440	0.0760			0.0340
	Ethyleneglycol	1109	0.0200	0.0480	Raschig rings	Glass		0.4200	0.2440	0.0760			0.0300
	Methanol	791	0.0006	0.0230	Raschig rings	Glass		0.4200	0.2440	0.0760			0.0280
	Water	1000	0.0010	0.0720	Raschig rings	Glass		0.4400	0.2560	0.0760			0.0330
	Ethyleneglycol	1109	0.0200	0.0480	Raschig rings	Glass		0.4400	0.2560	0.0760			0.0300
	Methanol	791	0.0006	0.0230	Raschig rings	Glass		0.4400	0.2560	0.0760			0.0240
Goto & Smith,1975	Water	1000	0.0010	0.0720	Spheres	Glass	0.0041	1.0000	0.3710	0.0258	0.1520	31.0	0.0282
	Water	1000	0.0010	0.0720	Spheres	Cu-Zn Catalyst	0.0029	1.0000	0.4410	0.0258	0.1520	28.0	0.0580
	Water	1000	0.0010	0.0720	Spheres	Cu-Zn	0.0005	1.0000	0.4530	0.0258	0.1520	22.0	0.1230

						Catalyst							
Iliuta,1996	Water	1000	0.0010	0.0720	Spheres	Glass	0.0030	1.0000	0.3700	0.0510	0.9200	31.0	0.0464
	CMC 0.1%+water	1000	0.0033	0.0720	Spheres	Glass	0.0030	1.0000	0.3700	0.0510	0.9200	30.0	0.0511
	CMC 0.5%+ Water	1001	0.0094	0.0700	Spheres	Glass	0.0030	1.0000	0.3700	0.0510	0.9200	28.0	0.0641
	CMC 1%+ Water	1005	0.0214	0.0660	Spheres	Glass	0.0030	1.0000	0.3700	0.0510	0.9200	28.0	0.0837
	Water	1000	0.0010	0.0720	Spheres	Porous cat. SiO2-AlO3	0.0033	1.0000	0.3560	0.0510	0.9200	32.5	0.0304
	CMC 0.1%+ Water	1000	0.0033	0.0720	Spheres	Porous cat. SiO2-AlO4	0.0033	1.0000	0.3560	0.0510	0.9200	32.0	0.0423
	CMC 0.5%+ Water	1001	0.0094	0.0700	Spheres	Porous cat. SiO2-AlO5	0.0033	1.0000	0.3560	0.0510	0.9200	31.0	0.0488
	CMC 1%+ Water	1005	0.0214	0.0660	Spheres	Porous cat. SiO2-AlO6	0.0033	1.0000	0.3560	0.0510	0.9200	30.0	0.0670
Khan et al.2000	Water	1000	0.0010	0.0720	Spheres		0.0062	1.0000	0.3900	0.0910	1.0000	31.0	0.0546
	Water	1000	0.0010	0.0720	Spheres		0.0062	1.0000	0.3900	0.0910	1.0000	29.0	0.0507
	Water	1000	0.0010	0.0720	Spheres		0.0062	1.0000	0.3900	0.0910	1.0000	31.0	0.0449
	Water	1000	0.0010	0.0720	Spheres		0.0062	1.0000	0.3900	0.0910	1.0000	30.0	0.0429
	Water	1000	0.0010	0.0720	Raschig rings			0.4030	0.4800	0.0910	1.0000		0.0480
	Water	1000	0.0010	0.0720	Raschig rings			0.4030	0.4800	0.0910	1.0000		0.0456
	Water	1000	0.0010	0.0720	Raschig rings			0.4030	0.4800	0.0910	1.0000		0.0437
	Water	1000	0.0010	0.0720	Raschig rings			0.4030	0.4800	0.0910	1.0000		0.0408
	Water	1000	0.0010	0.0720	Berl saddles			0.4264	0.6200	0.0930	1.0000		0.0267
	Water	1000	0.0010	0.0720	Berl saddles			0.4264	0.6200	0.0930	1.0000		0.0254
	Water	1000	0.0010	0.0720	Berl saddles			0.4264	0.6200	0.0930	1.0000		0.0198
	Water	1000	0.0010	0.0720	Berl saddles			0.4264	0.6200	0.0930	1.0000		0.0186
Kohler &Richarz,1985	Water	1000	0.0009	0.0720	Spheres	Glass	0.0015	1.0000	0.3800	0.0300	0.6000	29.0	0.0570
	Organic mixture	934	0.0004	0.0350	Spheres	Glass	0.0015	1.0000	0.3800	0.0300	0.6000	30.0	0.0562
	Glycerol	1250	0.4720	0.0660	Spheres	Glass	0.0026	1.0000	0.4150	0.0490	0.0620	29.0	0.0480
	Water	1000	0.0010	0.0730	Spheres	Glass	0.0004	1.0000	0.4050	0.0500	0.2960	28.0	0.0520
	Water	1000	0.0010	0.0730	Spheres	Glass	0.0004	1.0000	0.4000	0.0500	0.3450	25.0	0.1160
	Methanol	796	0.0006	0.0228	Spheres	Glass	0.0004	1.0000	0.3960	0.0500	0.3400	24.0	0.1460
	Ethanol	793	0.0012	0.0220	Spheres	Glass	0.0004	1.0000	0.4080	0.0500	0.3360	23.0	0.1270
Kücükkafa,1985	Water	1000	0.0010	0.0720	Raschig rings	Stainless steel		0.4030	0.1130	0.0750			0.0471

	Ethyleneglycol	1109	0.0200	0.0480	Raschig rings	Stainless steel		0.4030	0.1130	0.0750			0.0455
	Water	1000	0.0010	0.0720	Raschig rings	Stainless steel		0.4030	0.0940	0.0750			0.0376
	Ethyleneglycol	1109	0.0200	0.0480	Raschig rings	Stainless steel		0.4030	0.0940	0.0750			0.0369
	Water	1000	0.0010	0.0720	Raschig rings	Stainless steel		0.4030	0.0810	0.0750			0.0463
	Ethyleneglycol	1109	0.0200	0.0480	Raschig rings	Stainless steel		0.4030	0.0810	0.0750			0.0367
	Water	1000	0.0010	0.0720	Raschig rings	Ceramic		0.4030	0.3580	0.1500			0.0237
	Ethyleneglycol	1109	0.0200	0.0480	Raschig rings	Ceramic		0.4030	0.3580	0.1500			0.0217
	Water	1000	0.0010	0.0720	Raschig rings	Stainless steel		0.4030	0.0550	0.1500			0.0282
	Ethyleneglycol	1109	0.0200	0.0480	Raschig rings	Stainless steel		0.4030	0.0550	0.1500			0.0239
	Water	1000	0.0010	0.0720	Raschig rings	Aluminium		0.4030	0.6190	0.1500			0.0247
	Ethyleneglycol	1109	0.0200	0.0480	Raschig rings	Aluminium		0.4030	0.6190	0.1500			0.0244
	Water	1000	0.0010	0.0720	Raschig rings	Stainless steel		0.4030	0.0780	0.0750			0.0712
	Ethyleneglycol	1109	0.0200	0.0480	Raschig rings	Stainless steel		0.4030	0.0780	0.0750			0.0413
	Water	1000	0.0010	0.0720	Raschig rings	Stainless steel		0.4030	0.0530	0.1500			0.0345
	Ethyleneglycol	1109	0.0200	0.0480	Raschig rings	Stainless steel		0.4030	0.0530	0.1500			0.0265
	Water	1000	0.0010	0.0720	Raschig rings	Polypropylene		0.4030	0.2760	0.1500			0.0364
	Ethyleneglycol	1109	0.0200	0.0480	Raschig rings	Polypropylene		0.4030	0.2760	0.1500			0.0289
Lakota,1990	Water	1000	0.0010	0.0720	Spheres	Glass	0.0030	1.0000	0.3820	0.1720	1.2000	33.0	0.0220
	Water	1000	0.0010	0.0720	Spheres	Porous catalyst	0.0037	1.0000	0.3910	0.1720	1.2000	34.0	0.0210
	Water	1000	0.0010	0.0720	Spheres	Porous catalyst	0.0055	1.0000	0.3870	0.1720	1.2000	28.0	0.0220
	Water	1000	0.0010	0.0720	Spheres	Glass	0.0060	1.0000	0.3850	0.1720	1.2000	33.0	0.0220
	Water	1000	0.0010	0.0720	Cylinders	Naphthalene	0.0062	0.8736	0.3100	0.1720	1.2000	34.0	0.0370
	Water	1000	0.0010	0.0720	Spheres	Glass	0.0052	0.8736	0.4200	0.1720	1.2000	34.0	0.0220
Levec et al.1986	Water	1000	0.0010	0.0725	Spheres	Glass	0.0030	1.0000	0.3750	0.1720	1.3000	33.0	0.0083

	Water	1000	0.0010	0.0725	Spheres	Glass	0.0060	1.0000	0.3850	0.1720	1.3000	34.0	0.0085
Mao et al. 1993	Water	998	0.0013	0.0616	Spheres	Glass	0.0015	1.0000	0.3670	0.0750	0.7500	30.0	0.0512
	Water	998	0.0013	0.0616	Spheres	Glass	0.0027	1.0000	0.3530	0.0750	0.7500	28.5	0.0502
	Water	998	0.0013	0.0616	3-lobed	Al extrudate	0.0011	0.6096	0.7380	0.0750	0.7500	14.0	0.1150
	10% glycerol+ water	1052	0.0026	0.0616	Spheres	Glass	0.0015	1.0000	0.3670	0.0750	0.7500	33.0	0.0539
	10% glycerol+ water	1052	0.0026	0.0242	Spheres	Glass	0.0027	1.0000	0.3530	0.0750	0.7500	34.0	0.0582
	10% glycerol+ water	1052	0.0026	0.0242	3-lobed	Al extrudate	0.0011	0.6096	0.7380	0.0750	0.7500	16.0	0.1100
	50% glycerol+ water	1110	0.0039	0.0363	Spheres	Glass	0.0015	1.0000	0.3670	0.0750	0.7500	22.0	0.0519
	50% glycerol+ water	1110	0.0039	0.0363	Spheres	Glass	0.0027	1.0000	0.3530	0.0750	0.7500	24.0	0.0490
	50% glycerol+ water	1110	0.0039	0.0363	3-lobed	Al extrudate	0.0011	0.6096	0.7380	0.0750	0.7500	15.5	0.1030
	90% ethanol+ water	869	0.0020	0.0336	Spheres	Glass	0.0015	1.0000	0.3670	0.0750	0.7500	26.0	0.0508
	90% ethanol+ water	869	0.0020	0.0336	Spheres	Glass	0.0027	1.0000	0.3530	0.0750	0.7500	24.5	0.0471
	90% ethanol+ water	869	0.0020	0.0336	3-lobed	Al extrudate	0.0011	0.6096	0.7380	0.0750	0.7500	14.5	0.1120
Mekuc & Levec,1994	Water	1000	0.0010	0.0720	Spheres	Glass	0.0030	1.0000	0.3750	0.1720	0.1300	29.0	0.0220
	Water	1000	0.0010	0.0720	Spheres	Porous alumina	0.0037	1.0000	0.3910	0.1720	0.1300	33.0	0.0210
	Water	1000	0.0010	0.0720	Spheres	Porous silica	0.0055	1.0000	0.3870	0.1720	0.1300	35.0	0.0220
	Water	1000	0.0010	0.0720	Spheres	Glass	0.0060	1.0000	0.3850	0.1720	0.1300	33.0	0.0230
	water+sodium octadecil sulphate	1000	0.0010	0.0720	Spheres	Glass	0.0030	1.0000	0.3750	0.1720	0.1300	31.0	0.0160
	water+sodium octadecil sulphate	1000	0.0010	0.0720	Spheres	Porous alumina	0.0037	1.0000	0.3910	0.1720	0.1300	32.0	0.0270
	water+sodium octadecil sulphate	1000	0.0010	0.0720	Spheres	Porous silica	0.0055	1.0000	0.3870	0.1720	0.1300	33.0	0.0290
	water+sodium octadecil sulphate	1000	0.0010	0.0720	Spheres	Glass	0.0060	1.0000	0.3850	0.1720	0.1300	34.0	0.0170

	Water	1000	0.0010	0.0720	Cylinders	Porous iron molybdate	0.0036	0.8700	0.4150	0.1720	0.1300	31.0	0.0370
	Water	1000	0.0010	0.0720	Cylinders	Porous zinc-copper-alumina	0.0045	0.8690	0.4200	0.1720	0.1300	32.0	0.0220
	Water	1000	0.0010	0.0720	Cylinders	Non-porous naphthalene	0.0055	0.8690	0.3100	0.1720	0.1300	33.0	0.0370
	Water	1000	0.0010	0.0720	Extrudates	Porous zinc-aluminate	0.0018	0.7400	0.4600	0.1720	0.1300	30.0	0.0280
	Water	1000	0.0010	0.0720	Raschig rings	Ceramic	0.0041	0.4300	0.5830	0.1720	0.1300	29.0	0.0280
Morsi et al. 1978	Methanol	805	0.0006	0.0251	Spheres	Co/Mo/Al Catalyst	0.0024	1.0000	0.3850	0.0500	1.2000	32.0	0.0273
	Cyclohexane	769	0.0009	0.0256	Spheres	Co/Mo/Al Catalyst	0.0024	1.0000	0.3850	0.0500	1.2000	32.0	0.0300
	Kerosene	810	0.0013	0.0258	Spheres	Co/Mo/Al Catalyst	0.0024	1.0000	0.3850	0.0500	1.2000	30.0	0.0304
	Desulfurized gasoil	840	0.0058	0.0290	Spheres	Co/Mo/Al Catalyst	0.0024	1.0000	0.3850	0.0500	1.2000	31.0	0.0404
	Ethyleneglycol	1118	0.0172	0.0490	Spheres	Co/Mo/Al Catalyst	0.0024	1.0000	0.3850	0.0500	1.2000	27.5	0.0855
	Polyethylene glycol	1146	0.0646	0.0394	Spheres	Glass	0.0024	1.0000	0.3850	0.0500	1.2000	31.0	0.0857
	Desulfurized gasoil	860	0.0050	0.0288	Cylinders		0.0020	0.6966	0.3810	0.0500	1.2000	30.5	0.0495
	Cyclohexane	780	0.0009	0.0250	Cylinders		0.0020	0.6966	0.3810	0.0500	1.2000	31.0	0.0370
Pironti et al.1999	Water	1000	0.0010	0.0720	Cylinders	Extruded catalyst	0.0037	0.8100	0.4100	0.1016	2.0000	31.0	0.0360
	Water	1000	0.0010	0.0724	Spheres	Glass	0.0031	1.0000	0.3840	0.0500	0.5000	31.0	0.0357
	Water	1000	0.0010	0.0724	Spheres	Glass	0.0031	1.0000	0.3840	0.0500	1.0000	32.0	0.0207
	Teepol+water	998	0.0011	0.0601	Spheres	Glass	0.0031	1.0000	0.3860	0.0500	2.0000	33.0	0.0208
	Sulfite+water	1098	0.0018	0.0491	Spheres	Glass	0.0031	1.0000	0.3840	0.0500	1.0000		0.0084
	Kerosene	784	0.0011	0.0250	Cylinders	Catalyst	0.0018	0.8130	0.4850	0.0500	1.0000	35.0	0.0044
	Gasoil	838	0.0052	0.0291	Cylinders	Catalyst	0.0018	0.8130	0.4850	0.0500	1.0000	31.0	0.0209
	Polyethylene glycol	1124	0.0646	0.0398	Cylinders	Catalyst	0.0018	0.8130	0.4850	0.0500	1.0000	31.5	0.0475
	Kerosene	784	0.0011	0.0250	Spheres	Glass	0.0031	1.0000	0.3840	0.0500	1.0000	28.0	0.0184
	Gasoil	838	0.0052	0.0291	Spheres	Glass	0.0031	1.0000	0.3840	0.0500	1.0000	32.0	0.0204
	Ethyleneglycol	1109	0.0208	0.0470	Spheres	Glass	0.0031	1.0000	0.3840	0.0500	1.0000	32.0	0.0292

	Polyethylene glycol	1124	0.0646	0.0398	Spheres	Glass	0.0031	1.0000	0.3840	0.0500	1.0000	31.0	0.0084
	Cyclohexane	778	0.0009	0.0256	Spheres	Glass	0.0031	1.0000	0.3860	0.0500	2.0000	34.0	0.0347
Rao et al,1983	Water	1000	0.0010	0.0720	Spheres	Glass	0.0067	1.0000	0.3730	0.0924	1.8350	34.0	0.0184
	Water	1000	0.0010	0.0720	Cylinders	Ceramic	0.0093	0.8735	0.3730	0.0924	1.8350		0.0201
	Water	1000	0.0010	0.0720	Raschig rings	Glass		0.4030	0.2450	0.0750			0.0431
	Ethyleneglycol	1109	0.0200	0.0480	Raschig rings	Glass		0.4030	0.2450	0.0750			0.0388
	Methanol	791	0.0006	0.0230	Raschig rings	Glass		0.4030	0.2450	0.0750			0.0363
	Water	1000	0.0010	0.0720	Raschig rings	Polypropylene		0.4030	0.3100	0.0750			0.0401
	Ethyleneglycol	1109	0.0200	0.0480	Raschig rings	Polypropylene		0.4030	0.3100	0.0750			0.0373
	Methanol	791	0.0006	0.0230	Raschig rings	Polypropylene		0.4030	0.3100	0.0750			0.0314
	Water	1000	0.0010	0.0720	Raschig rings	Aluminium		0.4030	0.2350	0.0750			0.0434
	Ethyleneglycol	1109	0.0200	0.0480	Raschig rings	Aluminium		0.4030	0.2350	0.0750			0.0388
	Methanol	791	0.0006	0.0230	Raschig rings	Aluminium		0.4030	0.2350	0.0750			0.0364
Rehani,1983	Water	1000	0.0010	0.0720	Spheres	Glass	0.0100	1.0000	0.6040	0.0750		27.0	0.0431
	Ethyleneglycol	1109	0.0200	0.0480	Spheres	Glass	0.0100	1.0000	0.6040	0.0750		26.5	0.0381
	Methanol	791	0.0059	0.0230	Spheres	Glass	0.0100	1.0000	0.6040	0.0750		27.5	0.0372
Saez et al.1991	Water	1000	0.0010	0.0731	Spheres	Glass	0.0008	1.0000	0.3700	0.0750	0.5000	25.0	0.1158
	Methanol	792	0.0006	0.0227	Spheres	Glass	0.0007	1.0000	0.3700	0.0750	0.5000	26.0	0.1128
	Kerosene	808	0.0010	0.0250	Spheres	Glass	0.0009	1.0000	0.3700	0.0750	0.5000	27.0	0.1013
	Methanol	792	0.0006	0.0227	Spheres	Glass	0.0009	1.0000	0.3700	0.0750	0.5000	28.0	0.0848
	Water	1000	0.0010	0.0731	Spheres	Glass	0.0017	1.0000	0.3700	0.0750	0.5000	29.0	0.0726
	Methanol	792	0.0006	0.0227	Spheres	Glass	0.0013	1.0000	0.3700	0.0750	0.5000	28.0	0.0707
	Kerosene	808	0.0010	0.0250	Spheres	Glass	0.0017	1.0000	0.3700	0.0750	0.5000	30.0	0.0635
	Methanol	792	0.0006	0.0227	Spheres	Glass	0.0017	1.0000	0.3700	0.0750	0.5000	31.0	0.0549
	Water	1000	0.0010	0.0731	Spheres	Glass	0.0040	1.0000	0.3700	0.0750	0.5000	31.0	0.0568
	Water	1000	0.0010	0.0731	Spheres	Glass	0.0040	1.0000	0.3700	0.0750	0.5000	31.0	0.0398
	Water	1000	0.0010	0.0731	Spheres	Glass	0.0040	1.0000	0.3700	0.0750	0.5000	30.0	0.0387
	Water	1000	0.0010	0.0731	Spheres	Glass	0.0040	1.0000	0.3700	0.0750	0.5000	31.0	0.0478
	Water	1000	0.0010	0.0731	Spheres	Glass	0.0040	1.0000	0.3700	0.0750	0.5000	32.0	0.0285
	Water	1000	0.0010	0.0731	Spheres	Glass	0.0040	1.0000	0.3700	0.0750	0.5000	32.0	0.0286
	Water	1000	0.0010	0.0731	Spheres	Glass	0.0040	1.0000	0.3700	0.0750	0.5000	33.0	0.0296
	Methanol	792	0.0006	0.0227	Spheres	Glass	0.0040	1.0000	0.3700	0.0750	0.5000	33.0	0.0269

	Water	1000	0.0010	0.0731	Spheres	Glass	0.0040	1.0000	0.3700	0.0750	0.5000	34.0	0.0202
	Kerosene	808	0.0010	0.0250	Spheres	Glass	0.0040	1.0000	0.3700	0.0750	0.5000	32.0	0.0280
	Methanol	792	0.0006	0.0227	Spheres	Glass	0.0040	1.0000	0.3700	0.0750	0.5000	33.0	0.0144
Shulman et al. 1955a	Water	1000	0.0010	0.0720	Raschig rings	Ceramic	0.0125	0.4982	0.6050	0.2540	0.9144	28.0	0.0325
	Water	1000	0.0010	0.0720	Raschig rings	Ceramic	0.0221	0.3873	0.7260	0.2540	0.9144	29.0	0.0150
	Water	1000	0.0010	0.0720	Raschig rings	Ceramic	0.0330	0.3862	0.7150	0.2540	0.9144	31.0	0.0089
	Water	1000	0.0010	0.0720	Berl saddles	Ceramic	0.0351	0.4360	0.6600	0.2540	0.9144	26.0	0.0317
	Water	1000	0.0010	0.0720	Berl saddles	Ceramic	0.0209	0.4264	0.6950	0.2540	0.9144	31.0	0.0110
	Water	1000	0.0010	0.0720	Raschig rings	Carbon	0.0223	0.3926	0.7000	0.2540	0.9144	24.0	0.0358
Shulman et al. 1955b	Dupont Petrowet Sol. 4	1000	0.0010	0.0370	Raschig rings	Ceramic	0.0221	0.3873	0.7260	0.2540	0.9144	30.0	0.0080
	Dupont Petrowet Sol. 1	1000	0.0010	0.0430	Raschig rings	Ceramic	0.0221	0.3873	0.7260	0.2540	0.9144	31.0	0.0082
	Dupont Petrowet Sol. 1	1000	0.0010	0.0430	Raschig rings	Ceramic	0.0221	0.3873	0.7260	0.2540	0.9144	29.0	0.0116
	Dupont Petrowet Sol. 1	1000	0.0010	0.0430	Raschig rings	Ceramic	0.0221	0.3873	0.7260	0.2540	0.9144	29.0	0.0145
	Dupont Petrowet Sol. 2	1000	0.0010	0.0575	Berl saddles	Ceramic	0.0209	0.4264	0.6950	0.2540	0.9144	31.0	0.0094
	Dupont Petrowet Sol. 2	1000	0.0010	0.0575	Berl saddles	Ceramic	0.0209	0.4264	0.6950	0.2540	0.9144	31.0	0.0108
	Dupont Petrowet Sol. 2	1000	0.0010	0.0575	Berl saddles	Ceramic	0.0209	0.4264	0.6950	0.2540	0.9144	30.0	0.0125
	Dupont Petrowet Sol. 3	1000	0.0010	0.0380	Raschig rings	Carbon	0.0223	0.3926	0.7000	0.2540	0.9144	23.0	0.0436
	Dupont Petrowet Sol. 3	1000	0.0010	0.0380	Raschig rings	Carbon	0.0223	0.3926	0.7000	0.2540	0.9144	24.0	0.0440
	Dupont Petrowet Sol. 3	1000	0.0010	0.0380	Raschig rings	Carbon	0.0223	0.3926	0.7000	0.2540	0.9144	22.0	0.0489
	Water	1000	0.0010	0.0720	Berl saddles	Ceramic	0.0209	0.4264	0.6950	0.2540	0.9144	30.0	0.0127
	Water	1000	0.0010	0.0720	Raschig rings	Ceramic	0.0221	0.3873	0.7260	0.2540	0.9144	29.0	0.0140
	Water	1000	0.0010	0.0720	Raschig rings	Carbon	0.0223	0.3926	0.7000	0.2540	0.9144	22.0	0.0473
	Sorbitol Sol. 1	1299	0.0165	0.0730	Berl saddles	Ceramic	0.0209	0.4264	0.6950	0.2540	0.9144	30.0	0.0116
	Sorbitol Sol. 1	1299	0.0165	0.0730	Raschig rings	Ceramic	0.0221	0.3873	0.7260	0.2540	0.9144	29.5	0.0127
	Sorbitol Sol. 1	1299	0.0165	0.0730	Raschig rings	Carbon	0.0223	0.3926	0.7000	0.2540	0.9144	23.0	0.0399
	Sorbitol Sol. 2	1268	0.0530	0.0730	Raschig rings	Ceramic	0.0221	0.3873	0.7260	0.2540	0.9144	30.0	0.0113
	Sorbitol Sol. 2	1268	0.0530	0.0730	Berl saddles	Ceramic	0.0209	0.4264	0.6950	0.2540	0.9144	30.0	0.0131

	Sorbitol Sol. 2	1268	0.0530	0.0730	Raschig rings	Carbon	0.0223	0.3926	0.7000	0.2540	0.9144	22.0	0.0469
	Sorbitol Sol. 3	1215	0.1850	0.0730	Berl saddles	Ceramic	0.0209	0.4264	0.6950	0.2540	0.9144	30.0	0.0136
	Sorbitol Sol. 3	1215	0.1850	0.0730	Raschig rings	Ceramic	0.0221	0.3873	0.7260	0.2540	0.9144	28.0	0.0146
	Sorbitol Sol. 3	1215	0.1850	0.0730	Raschig rings	Carbon	0.0223	0.3926	0.7000	0.2540	0.9144	30.0	0.0492
	Water	1000	0.0010	0.0720	Berl saddles	Ceramic	0.0209	0.4264	0.6950	0.2540	0.9144	29.0	0.0124
	Water	1000	0.0010	0.0720	Raschig rings	Ceramic	0.0221	0.3873	0.7260	0.2540	0.9144	21.5	0.0143
	Water	1000	0.0010	0.0720	Raschig rings	Carbon	0.0223	0.3926	0.7000	0.2540	0.9144	30.5	0.0487
	Sol CaCl 1	1170	0.0014	0.0774	Berl saddles	Ceramic	0.0209	0.4264	0.6950	0.2540	0.9144	28.5	0.0113
	Sol CaCl 1	1170	0.0014	0.0774	Raschig rings	Ceramic	0.0221	0.3873	0.7260	0.2540	0.9144	21.5	0.0135
	Sol CaCl 1	1170	0.0014	0.0774	Raschig rings	Carbon	0.0223	0.3926	0.7000	0.2540	0.9144	23.0	0.0445
	Sol CaCl 2	1225	0.0024	0.0803	Raschig rings	Ceramic	0.0221	0.3873	0.7260	0.2540	0.9144	29.0	0.0142
	Sol CaCl 3	1321	0.0045	0.0863	Berl saddles	Ceramic	0.0209	0.4264	0.6950	0.2540	0.9144	28.5	0.0118
	Sol CaCl 3	1321	0.0045	0.0863	Raschig rings	Ceramic	0.0221	0.3873	0.7260	0.2540	0.9144	21.0	0.0141
	Sol CaCl 3	1321	0.0045	0.0863	Raschig rings	Carbon	0.0223	0.3926	0.7000	0.2540	0.9144	25.0	0.0432
Specchia & Baldi,1977	Water	1000	0.0010	0.0720	Spheres	Glass	0.0060	1.0000	0.4000	0.0800	1.0500	30.5	0.0500
	9% glycerol +water	1030	0.0013	0.0520	Cylinders	Glass	0.0062	0.8736	0.3700	0.0800	0.7500	34.0	0.0507
	29% glycerol +water	1070	0.0024	0.0440	Cylinders	Glass	0.0062	0.8736	0.3700	0.0800	0.7500	32.0	0.0507
	Water	1000	0.0010	0.0720	Cylinders	Glass	0.0062	0.8736	0.3700	0.0800	0.7500	30.0	0.0507
	Water	1000	0.0010	0.0720	Cylinders	Glass	0.0031	0.8736	0.3800	0.0800	0.3000	28.0	0.0502
Standish,1968	Cerrobend (Pb,Bi,Cd, Sn alloy)	9581	0.0039	0.2768	Raschig rings	Steel	0.0559	0.3987	0.7100	0.0444	0.3048	25.0	0.0506
	Cerrobend (Pb,Bi,Cd, Sn alloy)	9504	0.0032	0.2768	Raschig rings	Steel	0.0559	0.3987	0.7100	0.0444	0.3048	24.0	0.0348
	Cerrobend (Pb,Bi,Cd, Sn alloy)	9489	0.0027	0.2768	Raschig rings	Steel	0.0559	0.3987	0.7100	0.0444	0.3048	24.5	0.0313
	Cerrobend (Pb,Bi,Cd, Sn alloy)	9448	0.0023	0.2768	Raschig rings	Steel	0.0559	0.3987	0.7100	0.0444	0.3048	26.0	0.0268
	Cerrobend (Pb,Bi,Cd, Sn alloy)	9581	0.0039	0.2768	Saddles	Porcelain	0.0559	0.3987	0.6420	0.0444	0.3048	26.5	0.0386
	Cerrobend	9504	0.0032	0.2768	Saddles	Porcelain	0.0559	0.3987	0.6420	0.0444	0.3048	28.0	0.0258

(Pb,Bi,Cd, Sn alloy)												
Cerrobend (Pb,Bi,Cd, Sn alloy)	9489	0.0027	0.2768	Saddles	Porcelain	0.0559	0.3987	0.6420	0.0444	0.3048	27.5	0.0209
Cerrobend (Pb,Bi,Cd, Sn alloy)	9448	0.0023	0.2768	Saddles	Porcelain	0.0559	0.3987	0.6420	0.0444	0.3048	29.5	0.0168
Cerrobend (Pb,Bi,Cd, Sn alloy)	9581	0.0039	0.2768	Rings	Porcelain	0.0069	0.3987	0.5650	0.0444	0.3048	30.0	0.0290
Cerrobend (Pb,Bi,Cd, Sn alloy)	9504	0.0032	0.2768	Rings	Porcelain	0.0069	0.3987	0.5650	0.0444	0.3048	30.5	0.0190
Cerrobend (Pb,Bi,Cd, Sn alloy)	9489	0.0027	0.2768	Rings	Porcelain	0.0069	0.3987	0.5650	0.0444	0.3048	31.5	0.0146
Cerrobend (Pb,Bi,Cd, Sn alloy)	9448	0.0023	0.2768	Rings	Porcelain	0.0069	0.3987	0.5650	0.0444	0.3048	32.5	0.0134
Cerrobend (Pb,Bi,Cd, Sn alloy)	9581	0.0039	0.2768	Rings	Carbon	0.0058	0.4390	0.6050	0.0444	0.3048	31.0	0.0224
Cerrobend (Pb,Bi,Cd, Sn alloy)	9504	0.0032	0.2768	Rings	Carbon	0.0058	0.4390	0.6050	0.0444	0.3048	30.0	0.0153
Cerrobend (Pb,Bi,Cd, Sn alloy)	9489	0.0027	0.2768	Rings	Carbon	0.0058	0.4390	0.6050	0.0444	0.3048	34.0	0.0129
Cerrobend (Pb,Bi,Cd, Sn alloy)	9448	0.0023	0.2768	Rings	Carbon	0.0058	0.4390	0.6050	0.0444	0.3048	35.0	0.0113
Mercury	13546	0.0017	0.4854	Raschig rings	Steel	0.0559	0.3987	0.6420	0.0444	0.3048	21.5	0.0660
Mercury	13546	0.0017	0.4854	Saddles	Porcelain	0.0069	0.3987	0.5650	0.0444	0.3048	28.0	0.0380
Mercury	13546	0.0017	0.4854	Raschig rings	Porcelain	0.0058	0.3987	0.7100	0.0444	0.3048	9.5	0.1050
Water	1000	0.0009	0.0720	Raschig rings	Steel	0.0559	0.3987	0.7100	0.0444	0.3048	21.0	0.0403
Water	1000	0.0009	0.0720	Raschig rings	Steel	0.0559	0.3987	0.7100	0.0444	0.3048	24.0	0.0341
Water	1000	0.0009	0.0720	Rings	Porcelain	0.0559	0.3987	0.6420	0.0444	0.3048	22.0	0.0665
Water	1000	0.0009	0.0720	Rings	Porcelain	0.0559	0.3987	0.6420	0.0444	0.3048	28.0	0.0293

	Water	1000	0.0009	0.0720	Rings	Carbon	0.0058	0.4390	0.6050	0.0444	0.3048	23.0	0.0975
	Water	1000	0.0009	0.0720	Saddles	Porcelain	0.0069	0.3987	0.5650	0.0444	0.3048	27.0	0.0803
	Water	1000	0.0009	0.0720	Saddles	Porcelain	0.0069	0.3987	0.5650	0.0444	0.3048	28.0	0.0341
Tsochatzidis,1998	Glycerol 70%+sodium chloride+water	1178	0.0202	0.0746	Spheres	Glass	0.0060	1.0000	0.3600	0.1400	1.2400	33.0	0.0260
	Glycerol 58%+sodium chloride+water	1130	0.0067	0.0762	Spheres	Glass	0.0060	1.0000	0.3600	0.1400	1.2400	32.0	0.0260
	Water	1000	0.0010	0.0760	Spheres	Glass	0.0060	1.0000	0.3600	0.1400	1.2400	34.0	0.0200
Van Swaaij,1969	Water	1000	0.0010	0.0720	Raschig rings	Glass	0.0096	0.4142	0.6900	0.1000	2.0800	31.0	0.0092
	Water	1000	0.0010	0.0720	Raschig rings	Glass	0.0096	0.4142	0.6900	0.1000	2.0800	25.0	0.0345
	Water	1000	0.0010	0.0720	Raschig rings	Glass	0.0056	0.3781	0.7000	0.1000	2.1000	26.0	0.0355
	Water	1000	0.0010	0.0720	Raschig rings	Glass	0.0201	0.4367	0.7330	0.1538	2.7200	27.0	0.0161
Wammes et al. 1990b	DEA 2M+water	1022	0.0017	N/A	Spheres	Glass	0.0030	1.0000	0.3900	0.0500	0.6000		0.0254
	40%ETG+1.5M DEA+water	1060	0.0040	N/A	Cylinders	Alumina	0.0037	0.8740	0.4100	0.0500	0.6000		0.0471
	Water	1000	0.0010	0.0720	Spheres	Glass	0.0030	1.0000	0.3900	0.0500	0.6000	30.0	0.0495
	40%ETG +water	1050	0.0029	0.0600	Spheres	Glass	0.0030	1.0000	0.3900	0.0500	0.6000	31.0	0.0408
	Ethanol	790	0.0012	0.0220	Spheres	Glass	0.0030	1.0000	0.3900	0.0500	0.6000	32.0	0.0398
	Ethanol	790	0.0012	0.0220	Cylinders	Alumina	0.0037	0.8740	0.4400	0.0500	0.6000	30.0	0.0356
	Water	1000	0.0010	0.0720	Cylinders	Alumina	0.0037	0.8740	0.4400	0.0500	0.6000	29.0	0.0585
Warner,1959	Mercury	13546	0.0017	0.4854	Raschig rings		0.0069	0.4390	0.7200	0.0445	0.5334	33.0	0.1060
Yang et al.1993	Water	1000	0.0010	0.0720	Spheres	Aluminium	0.0022	1.0000	0.6600	0.0500		26.0	0.0300
Zun et al.1997	Water	1000	0.0010	0.0720	Spheres	Glass	0.0060	1.0000	0.3700	0.1720	1.2000	33.0	0.0230

Table 4.3 Partition of connectivity weights of the ANN SLH correlation showing the relative impact of the input variables on the output variable using the criterion of Garson (1991).

Bo	50.1 %
(1-ε)/ε	18.1 %
Contact angle (θ_c)	16.8 %
Shape factor (ϕ)	9.8 %
BPR	5.2 %
Total	100 %

Table 4.4 Comparison in valid range of the performances of SLH models/correlations using the compiled database.

Model/Correlation	N	AARE
Saez and Carbonell(1985)	83	72.5
Saez et al. (1991)	147	180.7
Kramer (1998)	338	106.5
Mersmann (1975)	273	443.9
Mao et al.* (1993)	130	137.0
Stein** (2000)	184	69.5
This work	239	22.3

* SLH calculated using the number of liquid rings estimated by means of German (1989) equation;

$N_p = 3.1/\varepsilon$

** Estimated using the contact angle calculated with the algorithm proposed in this work.

Table 4.5 ANN normalized input/output functions and corresponding weights (ranges of applicability in brackets) for the SLH correlation.

$S = \frac{1}{1+\exp\left(-\sum_{j=1}^{3}\omega_j H_j\right)}$	$U_1 = \frac{\log(\phi)}{0.422416}$ $\quad U_2 = \frac{\log\left(\frac{(1-\varepsilon)/\varepsilon}{0.449755}\right)}{0.797243}$
$H_j = \frac{1}{1+\exp\left(-\sum_{i=1}^{6}\omega_{ij} U_i\right)}$	$U_3 = \frac{\log\left(\frac{\mathrm{BPR}}{0.71433}\right)}{12.28217}$
$1 \le j \le 2 \qquad H_3 = 1$	$U_4 = \frac{\log\left(\frac{\theta_c}{0.977724}\right)}{1.72637}$ $\quad U_5 = \frac{\log\left(\frac{\mathrm{Bo}}{5.30103}\right)}{7.2444}$ $\quad U_6 = 1$
$S = \frac{\log\left(\frac{\mathrm{SLH}}{2.36051}\right)}{1.52484}$	$\mathrm{BPR} = \frac{3}{2}\frac{D_c^2 H_b}{d_v^3}$ $\quad \mathrm{Bo} = \frac{\rho_\ell g R^2}{\sigma_\ell}$ $\quad [0.378 \le \phi \le 1]$ $\quad [0.355 \le (1-\varepsilon)/\varepsilon \le 2.22]$
$\begin{bmatrix} \mathrm{SLH} \ge 0044 \\ \mathrm{SLH} \le 0.146 \end{bmatrix}$	$[2150 \le \mathrm{BPR} \le 9.9 \times 10^{12}]$ $\quad [7.0 \le \theta_c \le 35]$

ω_{ij}	**1**	**2**	**3**	**4**	**5**	**6**
1	-1.39192	-1.88987	3.95538	-0.195066	-15.101	9.9596
2	-1.45349	-3.75946	6.3011	10.9297	-11.4207	-2.0424

ω_j	**1**	**2**	**3**
	4.38922	-4.55253	0.184316

Correlation downloadable from the Internet: http://www.gch.ulaval.ca/~flarachi

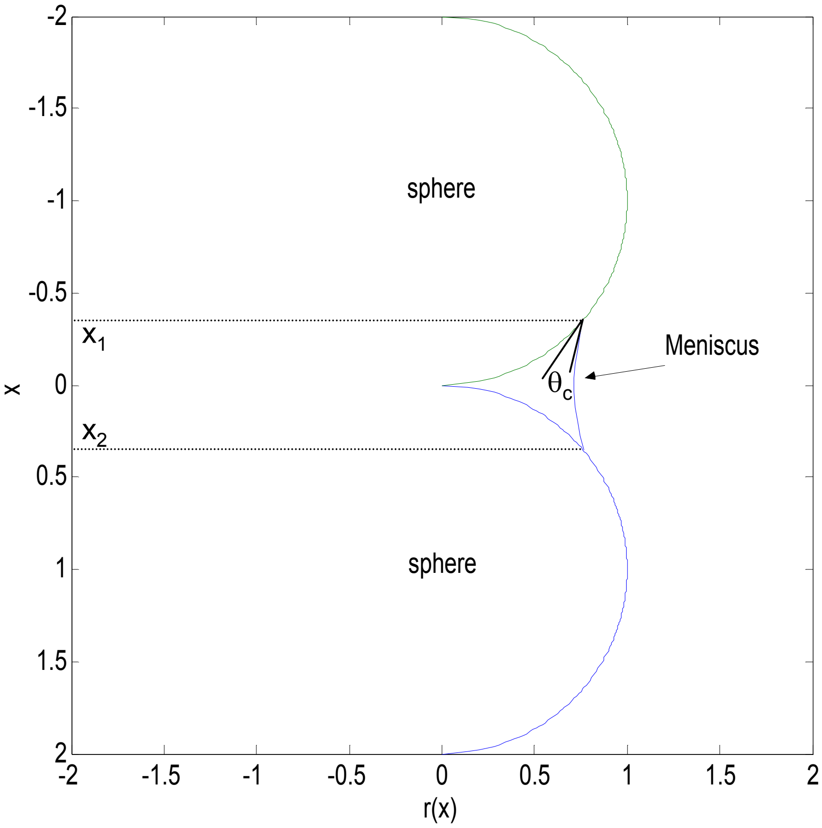

Figure 4.1 Domain and geometry definition for solving the Young-Laplace equation.

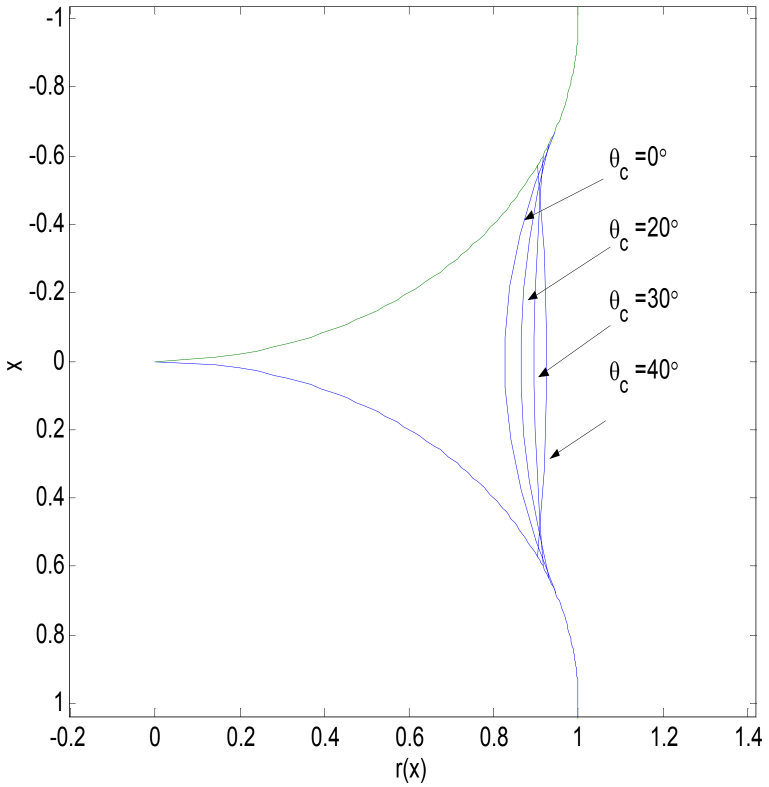

Figure 4.2 Calculated menisci for various contact angles at constant Bo and SLH values (Bo = 0.052 SLH = 0.115).

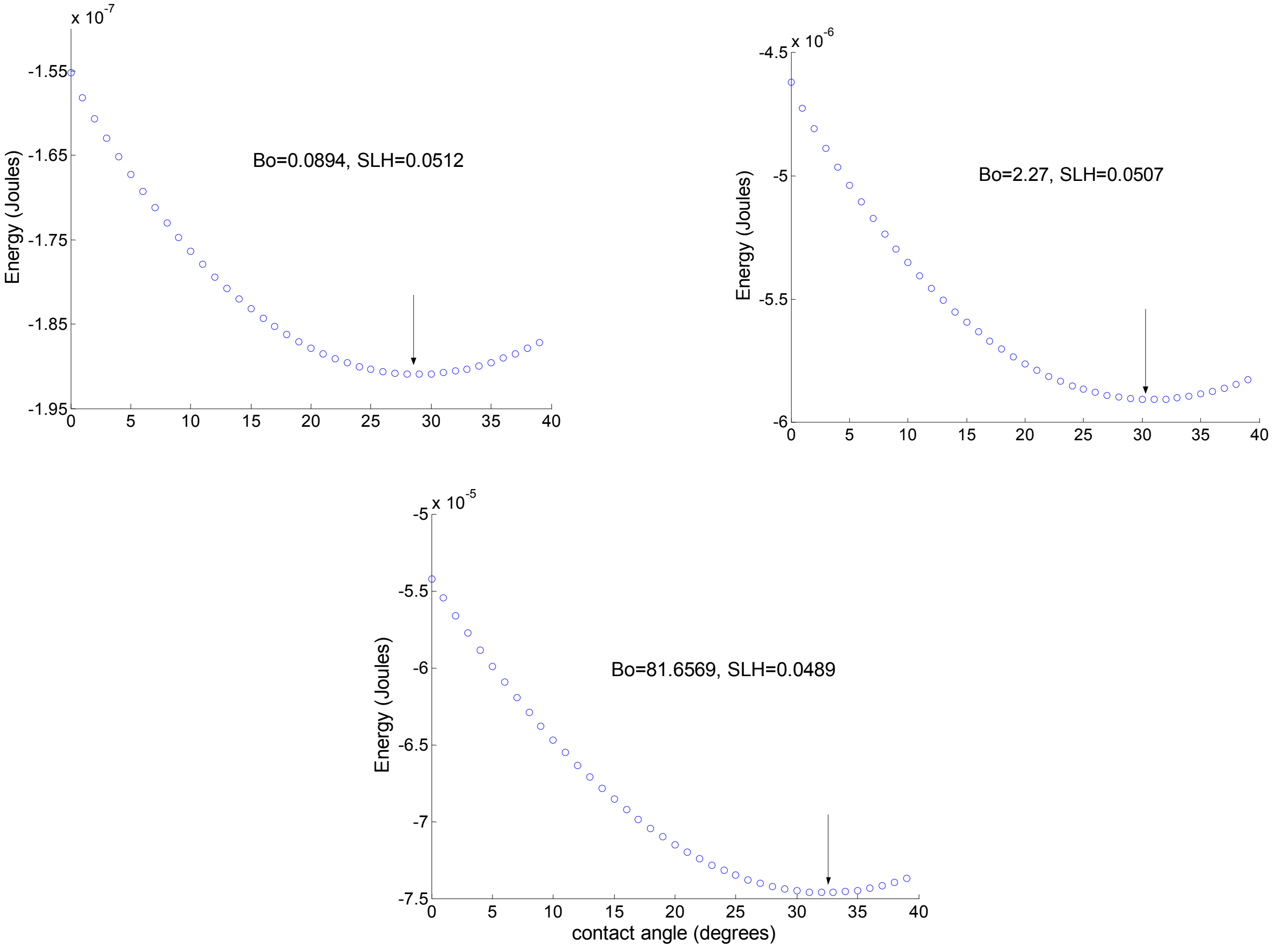

Figure 4.3 Typical simulations of interfacial energy change versus contact angle showing minimum energy corresponding to the contact angle for the stable menisci. Simulations for low, moderate and high Bond numbers and various SLH values.

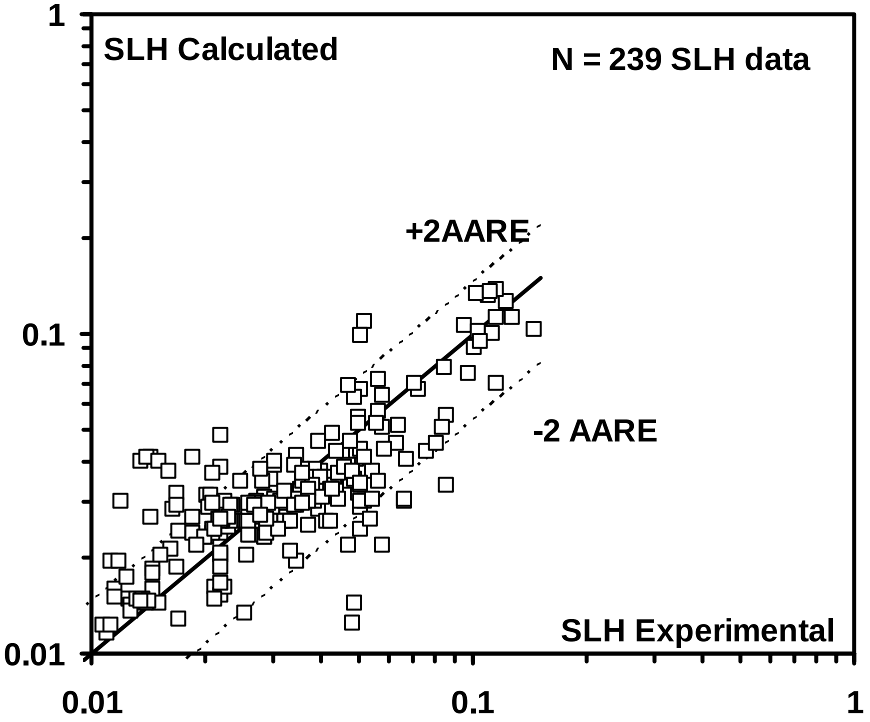

Figure 4.4 Parity plot of the measured versus predicted SLH (AARE= 22.3%, N = 239). Envelopes correspond to within ± 2 AARE predictions.

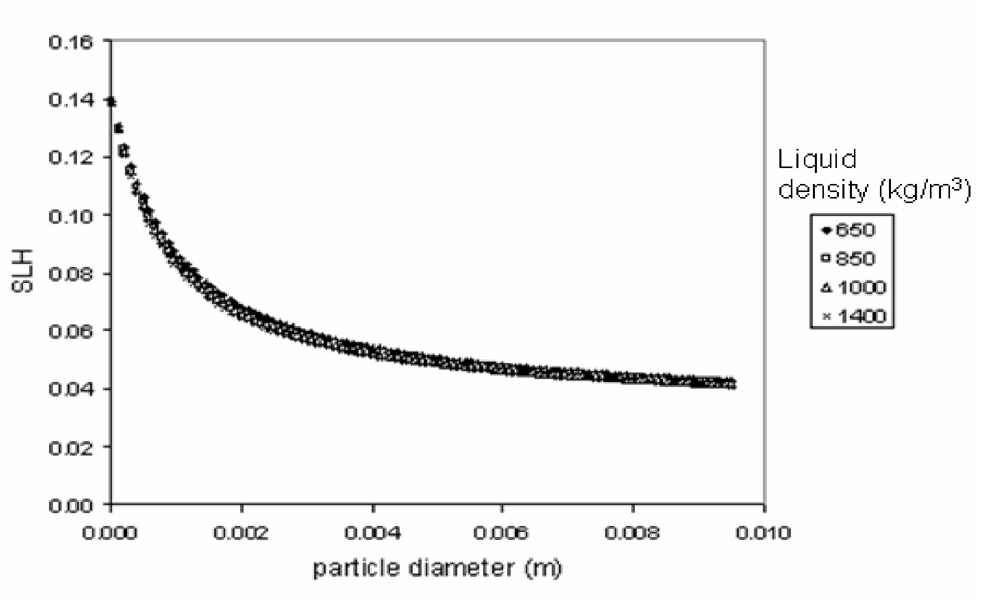
SLH
0.16
0.14
0.12
0.10
0.08
0.06
0.04
0.02
0.00
0.000
0.002
0.004
0.006
0.008
0.010
particle diameter (m)
Liquid density (kg/m³)
650
850
1000
1400

(a)

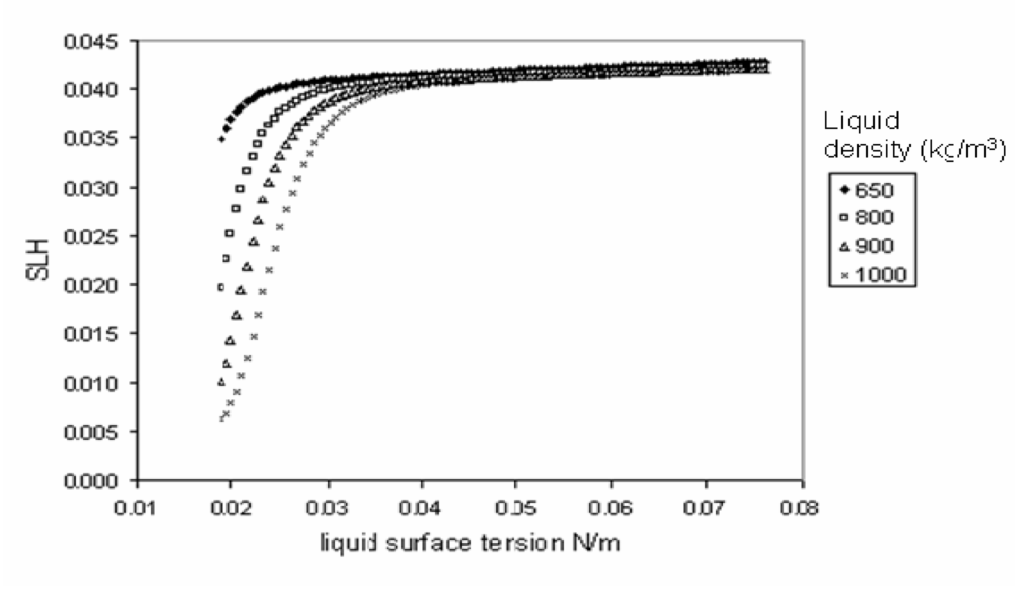
SLH
0.045
0.040
0.035
0.030
0.025
0.020
0.015
0.010
0.005
0.000
0.01
0.02
0.03
0.04
0.05
0.06
0.07
0.08
liquid surface tension N/m
Liquid density (kg/m³)
650
800
900
1000

(b)

(c)

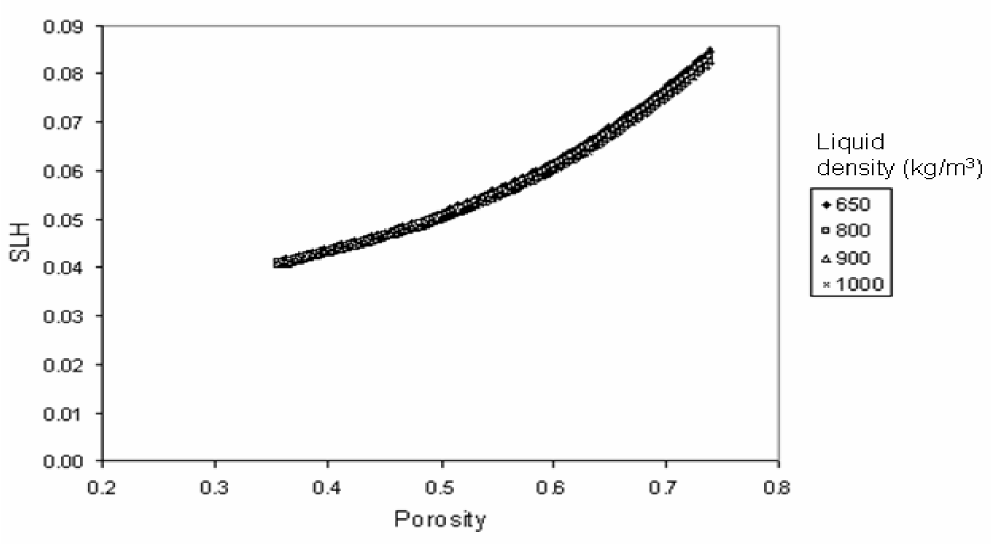

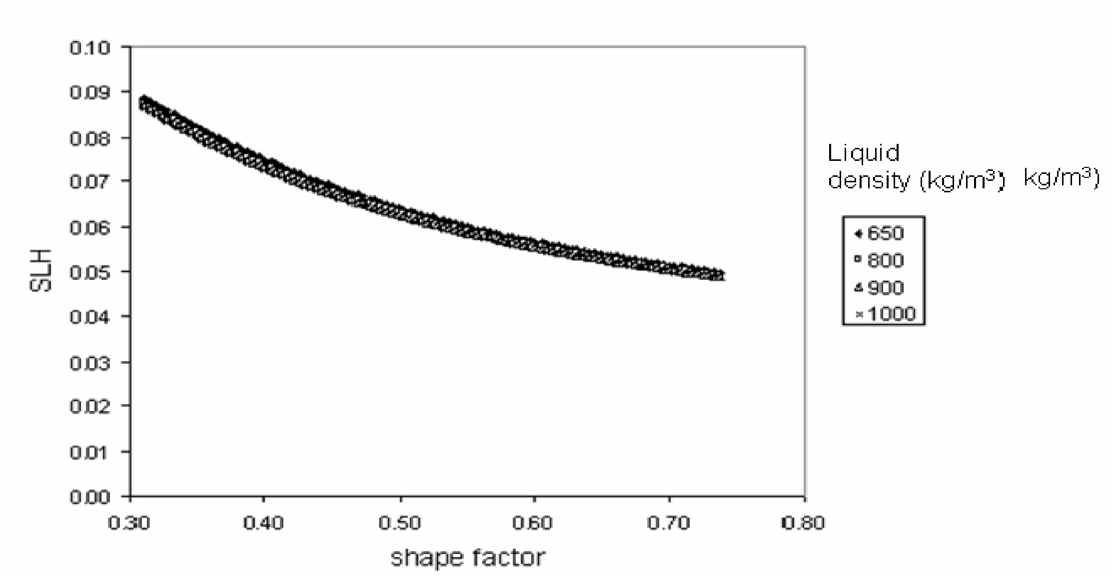

(d)

Figure 4.5 Neural network correlation simulations, SLH vs. (a) particle size, (b) surface tension and liquid density, (c) bed porosity, (d) sphericity factor at various liquid densities while keeping all other properties constant**.**

CHAPTER 5
Conclusions and recommendations

5.1 General Conclusions.

In this work, a study has been conducted to propose new theoretical tools and methodologies for the modeling of the plugging of packed beds in single phase and gas-liquid trickle flow operating under refinery and petroleum-like conditions.

Computational Fluid Dynamics (CFD) was explored as a simulation tool that proved to be a promising methodology for the transient and multidimensional modeling of the deep bed filtration phenomena in single and multiple phase conditions. The Euler-Euler CFD methodology proportionate snapshots of the transient inner porous media structure and bed properties while deposition develops. This feature cannot be reported by other methodologies. The importance of this capability of the CFD modeling will allow the models to be benchmarked when non-invasive methods will be available for the study of clogging in single and multiphase conditions.

To apply CFD accurately and effectively the closure equations added to the flow, continuity and momentum transfer equations must be physically sound and, if possible, based on first principles. In each chapter the closure equations were adapted from existing models or newly developed as it is explained in the following sections.

In chapter two, the choice for single phase deposition of fines closure equation was the renowned equation of Rajagopalan and Tien (1976). To explain the pressure drop and the loss of permeability of the bed, a combined effect of the loss of porous space and collector area increment was used. The augmentation of the collector area includes the shadow area effect as well as the multilayer collection model of Choo and Tien (1995b), while the loss of porosity was calculated by the net mass transfer coefficient accounting for the volume of the transferred fines. This approach compared favorably with the data of Narayan et al. (1997) while it was evident that not all the characteristics of the fines deposition were included. Particularly the experimenters reported specific morphologies that depended on the velocity of liquid. Flock like deposits were reported for low liquid velocities while compact deposits were found at higher liquid velocities. Another characteristic was the higher amounts of fines that were deposited in the particle-particle points of contact. None of these phenomena can be included in the closure equations model so more work on this features must be included in a more comprehensive model. Despite the simplifications shown, the model was able to predict the pressure drop, loss of porosity and permeability. Pressure drop was readily compared with the reported experimental data while loss of porosity and permeability distributions are contributed by the CFD modeling method. This information is still impossible to measure experimentally in such a detailed manner as it is shown in the results of the simulations. Actually, experimental methodologies require stopping the process and opening the packed bed to take pictures. If a snapshot is desired at several times, then the process shall be repeated at exactly the same conditions which is a difficult endeavor.

A new comprehensive modeling approach was proposed in chapter 3 for the plugging of multiphase trickle bed reactors. With the use of the slit model of Holub (1990) for the description of a packed bed in trickle flow and a modification of the Trajectory Analysis as presented by Payatakes et al. (1974), it was possible to calculate efficiencies for the capture of fines in clean and deposited collectors (monolayer and multilayer collection). Multilayer collections were calculated by solving a set of two differential equations; one for the free flowing liquid and another for the liquid present in the porous multilayer deposit. Brinkman's flow was assumed in the porous deposit that included an effective viscosity with an Einstein like form. The calculated efficiencies reflected coherently the theoretical trends shown for the collection in single phase. Such efficiencies were included in an Eulerian-Eulerian CFD code in which closure equations for the collector area increase and porosity reduction akin to the single phase case were used.

Results of the simulations were compared favorably with the experimental results of Gray et al. (2002) for the trickle flow case.

It is possible to conclude that the initial hypothesis statement that the deposition in multiphase flow is akin to the single phase case and is modified only by the presence of the gas phase flowing at a higher velocity seems to be plausible. The influence of the gas velocity on the model predicted lower deposition efficiencies at higher gas velocities being the acceleration provided by the gas over the liquid film the main reason of this effect. Another finding was the elucidation of the opposite effects given by the liquid velocity and the total liquid hold-up. Higher liquid velocities provide higher liquid hold-ups in trickle beds. Intuitively it can be conceptualized that a higher liquid hold-up should convey higher concentrations of fines and higher deposition ratios. Conversely, TA predicts lower deposition efficiencies at higher liquid velocities. TA on the slit geometry showed that the dominant mechanism was the liquid velocity giving lower deposition rates even when the total liquid hold-up increased.

Multiphase flow on packed beds is complicated by the presence of complex interactions between the present phases. An accurate description must include all the observed phenomena and models must include most of them. If a more exact formulation of the deposition of fines in trickle flow is needed, then the inclusion of the Static Liquid Hold-up (SLH) is necessary. Gray et al. (2002) and Fang et al. (1998) described the precise morphology in trickle flow, in which considerable amounts of particles were found on the points of contact of the packing material. It is in these regions in which the rate of renewal of liquid diminishes dramatically and SLH develops.

So far no model for the accurate estimation of SLH is available which includes the contact angle as an input parameter. Contact angle is difficult to measure as it depends on many physicochemical characteristics of the liquid and the solid surface; liquid properties, purity and physical and thermodynamical properties of the liquid and the solid phases. Even if these properties are controlled, the contact angle ranges between two extreme values; the advancing and receding contact angle depending on the measurement technique which makes this parameter even harder to obtain.

In chapter four, an effort was made to include this important parameter into a correlative model. Experimental SLH values were obtained from an extensive research in the open literature. With these values at hand a contact angle was obtained by a reverse method. Given a fixed volume of the meniscus dictated by experimental SLH, the equation of Young and Laplace was solved. Being the contact angle a boundary condition at the point of contact on a two sphere geometry, it was varied as well as position on the sphere. The stopping criterion was if a minimum energy of the meniscus configuration was found.

With this methodology and with the aid of neural networks, a correlative model was found for SLH. Among the findings it can be cited that the method provided an average value over the bed contact angle that seems to attain an approximate value of 30 degrees that can be used in the absence of more detailed measurements. The correlation behaves well giving an average absolute relative error (AARE) of 25% that compares very satisfactorily when comparing with the most used correlation (Saez and Carbonell, 1985) which gives 85%.

5.2 Recommendations for future work.

An important issue still to be resolved is the insertion of the static liquid hold-up in the model of plugging of packed beds in multiphase conditions. The only published study in which collection at the point of contact of the collectors is calculated by three dimensional trajectory analysis was presented by Cushing and Lawler (1998) in single phase conditions. Authors used the results of Snyder and Stewart (1966) for the flow field in a porous media modeled by an array-of-spheres which accounted for the points of contact on the bed. Trajectories were calculated using classical TA with non Brownian particles obtaining an equation in terms of the London, reduction and gravity numbers.

In the case of multiphase flow this approach is not at present possible as no trickle flow model exists than can predict the flow field including the static liquid holdup region. Then another methodology must be followed to achieve this goal.

Flow field in trickling film can be considered as formed of two regions, the first fraction proportional to (1-SLH) and a contiguous region of length proportional to SLH. It is possible to assume that fines traveling in the trickling film will first reach the static liquid hold-up region. As the region is considered stagnant, then it can be feasible to consider that the mechanism of capture will be sedimentation and as a simplification, it can be suggested that all the arriving fines will be captured. Then capture efficiency due to the SLH (η^{SLH}) can be calculated using TA in trickle film using the whole length of the slit. A problem to be resolved is that the stagnant liquid region has a finite volume given by the SLH and cannot keep on capturing fines of volume v_f beyond the volume given by the SLH; v_{SLH}. Also the concentration of the fines already captured in the SLH will diminish the driving force for the capture efficiency and the method must be modified according to the sedimentation theory.

Once filled the volume of the SLH other efficiency must be calculated for the fraction non-covered by the SLH using TA as proposed in chapter 3.

Hence, plugging of trickle beds under two-phase flow conditions must consider an additional filtering sub-stage in which the static liquid holdup is to be filled by the fines added to the initial stage normally described in DBF. This speculation must be, of course, proved experimentally and if so, the multistage model can be proposed.

References

Choo C.U. and Tien C. (1995b) Analysis of the transient behavior of deep-bed filtration. *J. Colloid Interface Sci.* **169**, 13-33.

Cushing R.S. and Lawler D.F. (1998) Depth filtration: Fundamental investigation through three dimensional trajectory analysis. *Env. Sci. Tech*. **32**, 3793.

Fang J., Chung K., Masliyah J. and Gray M.R. (1998) Characteristics of particle filtration from gas-liquid flow by packed beds. Personal Comunication.

Gray M.R., Srinivasan N. and Masliyah J.H. (2002) Pressure buildup in gas-liquid flow through packed beds due to deposition of fine particles. *Can. J. Chem. Eng.* **80**, 346-354.

Holub R. A. (1990) Hydrodynamics of trickle bed reactors. *Doctoral Thesis*, Washington University in St. Louis, MO, USA.

Narayan R., Coury J.R., Masliyah J.H. and Gray M.R.(1997) Particle capture and plugging in packed-bed reactors. *Ind. Eng. Chem. Res.* **36**, 4620-4627.

Payatakes A.C., Rajagopalan R. and Tien C. (1974) Application of porous media models to the study of deep filtration. *Can. J. Chem. Eng.* **52**, 722.

Rajagopalan R. and Tien C. (1976) Trajectory analysis of deep bed filtration with the sphere-in-cell porous media model. *AIChE J.* **3**, 523.

Saez A.E. and Carbonell R.G. (1985) Hydrodynamic parameters for gas-liquid cocurrent flow in packed beds. *AIChE J.* **31**, 52.

Snyder L. J. and Stewart W. E. (1966) Velocity and pressure profile for Newtonian creeping flow in regular packed beds of spheres. *AIChE J.* **12**, 167.